MgO based magnetic tunnel junctions

Lavrijsen, R.

Award date:
2006

Eindhoven University of Technology
Department of Applied Physics
Group Physics of Nanostructures (FNA)

MgO based Magnetic Tunnel Junctions

R. Lavrijsen

December, 2006

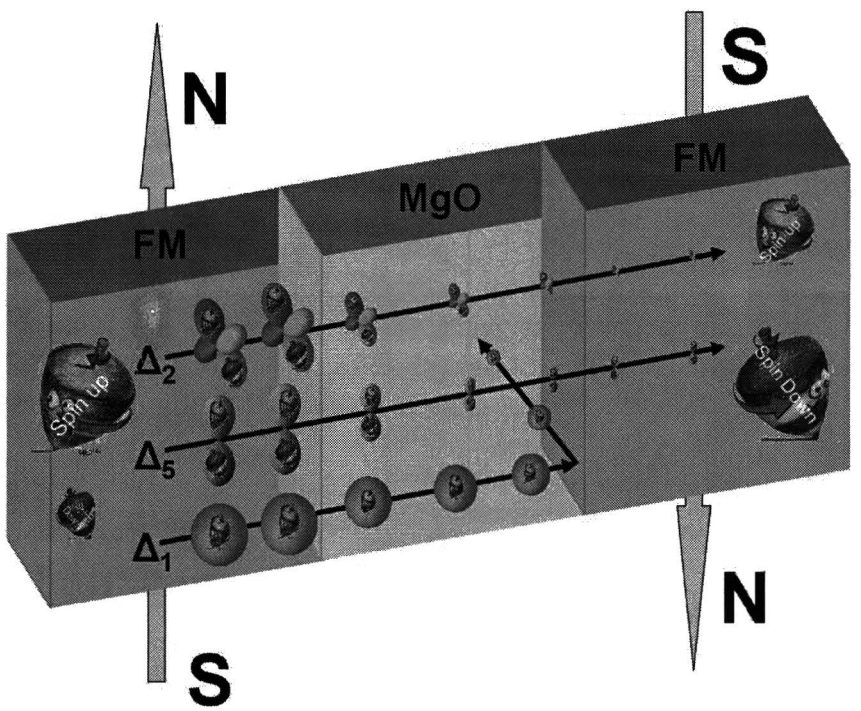

Report of a graduation project (December 2005 - December 2006) carried out at the Eindhoven University of Technology in the group Physics of Nanostructures (FNA)

Supervisors: P.V. Paluskar
prof.dr.ir. H.J.M. Swagten

Abstract

The realization of huge tunneling magnetoresistance is a hot topic of research in the area of spintronics. In this thesis, we explore the realization of this effect in magnetic tunnel junctions using poly-crystalline MgO barriers. The crystalline nature of MgO makes it an interesting barrier material as it acts as a filter allowing certain electronic states to tunnel more effectively than others. The theoretical understanding of this filtering process and its experimental realization has not only opened up new avenues for spintronics device applications but also shed light on the theory of tunneling.

We have been successful in the fabrication and magnetic engineering of CoFeB/MgO/-CoFeB junctions showing up to 90% tunneling magnetoresistance at room temperature and 150% at 4K. Our junctions and MgO barriers are analyzed with various experimental techniques such as X-ray diffraction, X-ray photoelectron spectroscopy, magneto optical Kerr effect and electrical transport measurements. We find that our MgO barriers are non-stoichiometric with an excess of oxygen. Also we find an indication for high levels of impurities in the barrier. We show that these are the reason for non-optimal performance, i.e. low TMR values and a high sample to sample variation in our magnetic tunnel junctions.

Further optimization is in progress by implementing a new sputter magnetron able to sputter at very low pressures and using a sintered high purity, high density MgO target.

Contents

1 General Introduction 4
- 1.1 Magnetoresistive devices . . . 4
- 1.2 Motivation . . . 7
- 1.3 This Thesis . . . 7

2 Theoretical background and experimental techniques 8
- 2.1 Spin Polarized Tunneling . . . 8
  - 2.1.1 Basic magneto-transport . . . 12
  - 2.1.2 Temperature and bias voltage dependence . . . 13
- 2.2 Theory of tunneling in crystalline Fe-MgO-Fe MTJ's . . . 15
  - 2.2.1 Electronic band structure . . . 16
  - 2.2.2 Fe-MgO-Fe system . . . 26
- 2.3 Experimental techniques . . . 31
  - 2.3.1 Superconducting Tunneling Spectroscopy (STS) . . . 31
  - 2.3.2 Magneto Optical Kerr Effect (MOKE) . . . 33
  - 2.3.3 X-ray Diffraction (XRD) . . . 33
  - 2.3.4 Sputter deposition . . . 35
  - 2.3.5 X-ray Photoelectron Spectroscopy (XPS) . . . 37

3 Critical points for huge TMR-effects 41
- 3.1 Research strategy . . . 44
- 3.2 Sample fabrication . . . 46

4 MgO characterization 48
- 4.1 X-ray diffraction . . . 48
  - 4.1.1 Target-Sample distance . . . 48
  - 4.1.2 Seed layer . . . 50
  - 4.1.3 Crystallization . . . 52
- 4.2 Sputter Optimization of the MgO layer in MTJ's . . . 57
- 4.3 X-ray photoelectron spectroscopy . . . 64
  - 4.3.1 Metallic Mg and Plasma Oxidized Mg . . . 64
  - 4.3.2 Single Crystal MgO and Sputter deposited MgO . . . 67
  - 4.3.3 Stoichiometry . . . 70

4.3.4 Partial H_2O and impurity pressure 72

5 TMR in MgO based MTJ's and SPT measurements 75
5.1 Magnetic characterization 75
5.1.1 Hard-Soft MTJ's 75
5.1.2 Exchange biased MTJ's 77
5.2 IV characteristics 77
5.3 TMR behavior 80
5.4 Spin Polarized Tunneling measurements 85

6 Conclusions and Outlook 88

Chapter 1

General Introduction

Our hunger for information in all facets of life has led to a booming business; look at the recent gadgets as mobile phones with built-in TV and internet access, portable playstations where one can now watch news, browse the internet, play games, all with graphical splendor wherever one wants. These technologies ask for ever-increasing data storage and memory capacity which needs to become faster, cheaper, energy efficient and easy to make. Until recently this was only done with the electric charge property of electrons, but now rapid progress is being made using the spins of the electrons as information carriers. Very soon we will evolve from the realm of electronics to spintronics [1]. In this new exciting field, we use the intrinsic magnetic moment of a free electron: namely spin-up and spin-down. Its interaction via coupling of the spins with an external magnetic field leads to a shift of the energy levels of the two states. In magnetic materials, where spin-up and spin-down electron populations are unequal, an electric current should naturally be spin polarized, i.e. the current should consist of an unequal number of spin-up and spin-down electrons. So through the interaction of the spins with an external applied magnetic field an additional degree of freedom is created for device design, namely control of the spin populations. One of the best studied effect which is a direct consequence of the aforementioned phenomenon is the magnetoresistance effect, as discussed in the next section. This effect finds applications in devices ranging from magnetic field sensors, read heads for hard disks, biosensors to non-volatile memories. The topic of this thesis is the characterization of MgO, a material used in magnetoresistive devices that enhances their performance manyfold.

This general introduction will briefly describe the magnetoresistive effects and their applications. Also some of the concepts used throughout this thesis will be explained. Finally our motivation for this thesis work will be given.

1.1 Magnetoresistive devices

A magnetoresistive device is a device that shows a change in resistance under the application of a magnetic field. There is a whole range of different magnetoresistance effects, each having a different magnitude and physical origin. In a normal metal, the application

of a field will result in a resistance change on the order of 0.1% which originates from the electrons travelling in helical orbits due to the Lorentz force. In ferromagnetic metals, however, the resistance is also dependent on the relative orientation of the current to the magnetization direction. This effect can be in the order of a few percent and is referred to as anisotropic magnetoresistance (AMR). In 1988 the giant magnetoresistance effect (GMR) was discovered [2] typically in the order of 10%, it is observed when ferromagnetic and non-magnetic layers are stacked, for instance Fe/Cr/Fe or Co/Cu/Co. The effect originates due to the fact that electrons with spin-up and and spin-down moments "see" different resistivities as they propagate across these layers depending on whether the magnetization (north-south direction) of the ferromagnetic layers is mutually parallel or anti-parallel. This discovery made a record-fast introduction of GMR based devices in the consumer market where it is used even today in read-heads for hard-disks. Such a read head can be seen in figure 1.1. The stray field emanating from the surface represents a binary "1" or "0" depending on the magnetization direction of the surface and is detected by the read head.

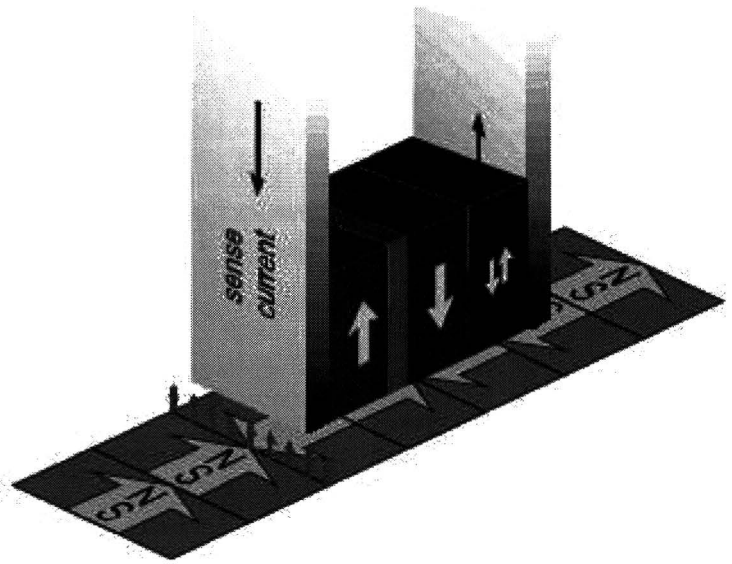

Figure 1.1: Schematic illustration of a magnetoresistive read head passing over media containing oppositely magnetized regions. The magnetization of the softer magnetic layer in the read head is influenced by the perpendicular fields emanating from the media, resulting in a change of the current passing through the sensor.

Another application uses the non-volatile property of the ferromagnetic material. This means that when the magnetization is set in a certain direction it will stay this way until it is set into another direction, also known as the hysteresis-effect. This can be used to set a binary "0" or "1". If we combine the hysteresis and the magnetoresistance effect, we can make an array of elements which are all separately addressable, each element being one bit. Such a device can be seen in figure 1.2. This is the non-volatile magnetic random access memory (MRAM), one that does not require power to maintain the information stored.

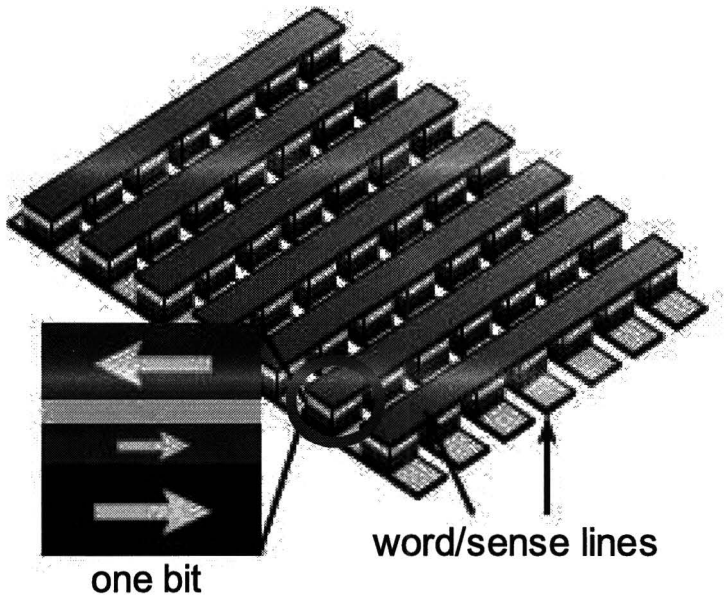

Figure 1.2: Schematic illustration of a magnetic random access memory (MRAM) based on magnetoresistance. Between every crossing of the word and sense lines is one magnetic junction. The word and sense lines permit measurement of the junction resistance and also create the magnetic fields required to switch the resistance state of the junction.

Tunneling magneto-resistance (TMR) is another effect observed in layered stacks when the normal metal of the GMR stack is replaced by an insulator, so that we have the stack FM/I/FM where FM stands for the ferromagnetic layer and the I for the insulating layer. In this case we use the quantum-mechanical phenomenon of electron tunneling through an insulator where an electron can pass through a classically forbidden region, i.e. the insulator. This is possible if the forbidden region is made sufficiently thin. Due to the wave-like nature of electrons in quantum mechanics the "probability" to find an electron on the other side of such a region (barrier) is non-zero. Typical thickness of such barriers is less then a couple of nm. This is exactly what is done in this thesis; we combine one such thin insulation barrier (MgO) with magnetic electrodes. Later we will show that the tunneling probability of the different spin-up and spin-down electrons can be controlled by varying the magnetic electrode material, and the thickness and type of barrier. Traditionally aluminum oxide (AlO_x) has been used as the barrier material of choice, due to the ease of making such a ultra thin, pinhole-free and flat barrier. However, after optimizing these barriers, a maximum TMR effect of 70% has been observed [3]. Although, this TMR effect results in a much better signal to noise ratio in comparison to the GMR effect, due to the enormous market potential, a worldwide research effort to improve TMR performance is underway. A big step forward was made with the theoretical prediction of huge TMR effects of over 1500% by using MgO as barrier material by Butler *et al.* [4] and Mathon and Umerski [5] in 2001, and the first promising results showing 180% TMR by Parkin *et al.* [6] and Yuasa *et al.* [7] in 2004. The full complex mechanism

behind the tunneling process through a crystalline barrier is still not fully understood. At the time of this writing, TMR ratios of more then 500% have been reported and there is still considerable room for improvement. This brings us to the motivation for this thesis.

1.2 Motivation

The motivation to devote a master thesis to MgO as barrier material for magnetic tunnel junctions results from the promise that MgO holds as a future barrier for applications in commercial devices. The Physics of Nanostructrues group (FNA) at the Technical University of Eindhoven has a strong history and experience in spintronics and is always looking for new exciting research opportunities. Within the group there is a treasure of knowledge on magnetic tunnel junctions using AlO_x barriers and the engineering of the magnetic properties of the ferromagnetic electrodes. So with the aforementioned theoretical prediction of huge >1500% TMR with MgO, and its first experimental realization, it was a logical step to start fabricating MgO based magnetic tunnel junctions. The aim of such a step is not only to understand the underlying physics of tunneling in crystalline barriers, but also to contribute to new ideas and device physics by cleverly engineering the stacks and address the numerous outstanding issues in the area of magnetic tunnel junctions. The PhD research of Paresh Paluskar, dedicated to investigating novel magnetic and barrier materials for applications in spintronics, made the topic of this work an ideal sub-topic of his thesis.

Concluding, considering the limited time frame for a master thesis, the objective for this thesis was created: demonstrate the fabrication and optimization of MgO barriers for magnetic tunnel junctions and realize the measurement of the tunneling spin polarization of magnetic tunnel junctions with MgO barriers.

1.3 This Thesis

This thesis is built up in the following way:

- In chapter 2 we will first explain the theory behind spin polarized tunneling and the used characterization tools and measurement techniques.
- Chapter 3 discusses the critical points needed to obtain the huge TMR values in crystalline MgO barriers. We also give an overview of the used samples.
- In chapter 4 we present the characterization of the MgO barrier material including the growth optimization and a chemical analysis.
- Then we turn to the magnetic and electrical characterization of MTJ's and discuss the results obtained with the spin polarized tunneling apparatus in chapter 5.
- Finally, in chapter 6 we will draw conclusions and give an outlook.

Chapter 2

Theoretical background and experimental techniques

In this chapter we will discuss the theory of spin polarized tunneling and some aspects of the experimental techniques used. The current theory describing the tunneling through the crystalline MgO barrier will be discussed from which we can identify the critical parameters for realizing the huge TMR effects. We will start with the simple description of the tunnelling mechanism in normal tunnel junctions (i.e. normal metals) using a quantum-mechanics textbook example. We then turn to magnetic tunnel junctions (MTJ's) and relate the tunneling to density of states factors of spin-up and spin-down electrons in ferromagnetic materials providing a simple explanation of the (TMR) effect. In section 2.1.1 we will discuss the commonly used models to characterize the barrier in terms of barrier height and thickness. This will later supply us with a model to compare our junctions with those of other groups. Subsequently we discuss a model that explains the experimental observed dependence of the TMR effect on temperature and bias voltage. In section 2.2, we will discuss the current theoretical interpretation of the huge TMR effect observed with crystalline MgO barriers. Section 2.2 discusses the theory of tunneling through crystalline MgO barriers. For the results presented in chapter 4 and 5 an in-depth understanding of this section will not be needed. We will summarize the most critical points as obtained from the theory in chapter 3. Finally, we will shortly discuss the used experimental techniques.

2.1 Spin Polarized Tunneling

In this section we will discuss the theory of spin polarized tunneling in magnetic tunnel junctions. Generally, we will follow the discussion given in the review of Swagten [8] and summarize its most important points. As discussed in section 1.1, the tunnel junction is a device where two metals are separated by a thin insulator. By making this insulating layer very thin (nanometers), the electrons responsible for the electrical conduction are allowed to tunnel from one electrode to the other. This is schematically displayed in figure 2.1.

The description of the tunneling current through these junctions is extensively treated

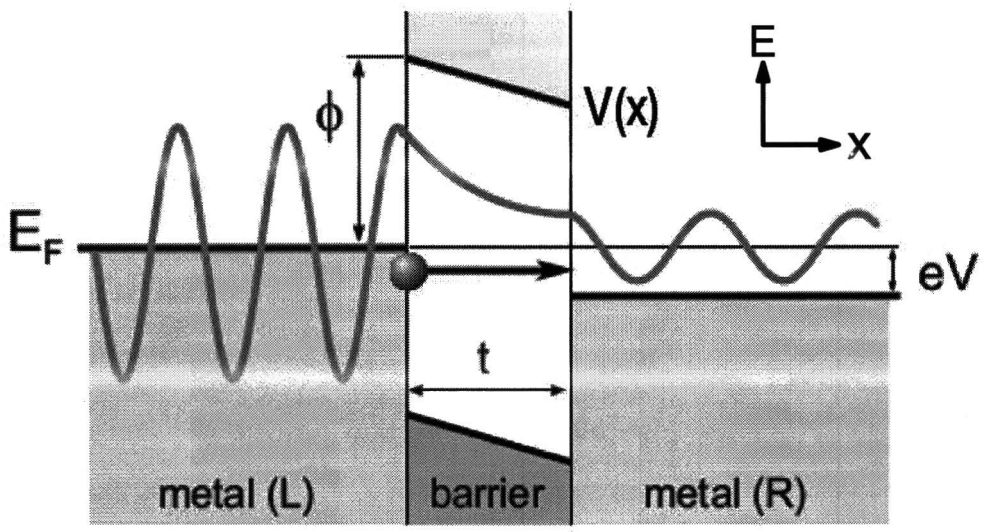

Figure 2.1: The wave function in a metal-oxide-metal tunnel structure schematically shows the concept of quantum-mechanical tunneling for electrons with an energy close to the Fermi energy E_F. The barrier height at the interface between metal and oxide is given by ϕ. A non-zero tunnelling current is flowing when a bias voltage V is applied between the metallic electrodes. The grey areas in the metal regions represent the occupied density-of-states (DOS), in the barrier the energy gap of the insulator is indicated in white, from [8].

in elementary textbooks on quantum mechanics. If we revive this and use the Wentzel-Kramers-Brillouin (WKB) approximation, which is valid for potentials V varying slowly on the scale of the electron's wavelength, the transmission probability for an electron in one dimension is given by:

$$T(E, k_{\|} = 0) \approx \exp\Big(-2 \int_0^t \sqrt{2m[V(x) - E]/\hbar^2}\, dx \Big) \tag{2.1}$$

with E the electron energy, m the electron mass, and x the direction perpendicular to the barrier plane. This equation directly shows the well-known exponential of $T(E)$ dependance on the barrier thickness t and energy barrier $V(x) - E$. The electron momentum in the plane of the layers is assumed to be absent, i.e. $k_{\|} = 0$, so all the electrons are assumed to be tunneling along the normal of the barrier. If we also include tunneling for electrons having a momentum in the plane of the barrier, the probability for tunneling rapidly decreases. In that case the term $2m[V(x) - E]/\hbar^2$ in the exponent of the transmission should be replaced by $2m[V(x) - E]/\hbar^2 + k_{\|}^2$, resulting in a lower transmission probability for $k_{\|} \neq 0$. This simple textbook example gives us the understanding of the probability of tunneling, which is dependent on the (1) barrier thickness (t) (2) barrier height (ϕ) (3) fast decrease of tunnel probability with increasing component $k_{\|}$. We will see later that for a crystalline MgO barrier this list is incomplete (see section 2.2).

In an experimental situation with no voltage applied, the Fermi level of both electrodes are equal and no tunnel current will result if we assume that $V(x)$ is constant throughout

the barrier. If we now apply a voltage across the junction, the Fermi level is lowered (by eV) at the right-hand side of the barrier as is indicated in figure 2.1, electrons are now able to elastically tunnel from filled available electron states (left) towards unoccupied states in the second (right) electrode. This is because there is a lower energy state at the right side of the barrier. As a result, the tunneling current will be proportional to the product of the available, occupied electron states on the left (DOS), and the number of empty states at the right electrode multiplied by the barrier transmission probability given by equation (2.1). Summarizing we find that the tunneling current is a function of the transmission probability and the DOS of the two electrode systems. So for small voltages $eV \ll \phi$ and low enough temperatures $k_bT \ll eV$ (electrons close to the Fermi level) we can write the tunnel conductance as:

$$G \equiv dI/dV \propto N_L(E_F)N_R(E_F)T(\phi, t) \tag{2.2}$$

where N_L and N_R are the DOS of the left, right electrode respectively, scaled by the tunneling probability. Knowing this, we can proceed to evaluate the current in the *magnetic* tunnel junction. Now the metal electrodes are replaced by ferromagnetic electrodes. This is seen in figure 2.2, where the DOS of a ferromagnetic material are represented by a simple majority and minority electron band, shifted in energy due to the exchange interaction. We consider two identical ferromagnetic electrodes with parallel magnetization orientations, separated by an insulating barrier. Assuming that the electron spin is conserved in these processes [9], tunneling may only occur between bands of the same spin orientation in either electrode, i.e., from a spin majority band to a spin majority band, and similar for the minorities. Using equation 2.2 and assuming equal transmission of both spin species, we write the conductance for parallel magnetization as:

$$G_P = G_\uparrow + G_\downarrow \propto N^2_{maj}(E_F) + N^2_{min}(E_F), \tag{2.3}$$

where $G_{\uparrow(\downarrow)}$ is the conductance in the up- (down-) spin channel and $N_{maj}(E_F)$, $(N_{min}(E_F))$ is the majority (minority) DOS at E_F. When we switch the magnetization of one electrode, we also switch the spin quantization of that electrode. Tunneling between same spin orientations now means tunneling from a majority to a minority channel and vice versa. The conductance for antiparallel aligned magnetization is then:

$$G_{AP} = G_\uparrow + G_\downarrow \propto 2N_{maj}(E_F)N_{min}(E_F). \tag{2.4}$$

By comparing these equations we see a difference in the conductance, i.e. a change in the resistance. If we put this in words, ferromagnetic tunnel junctions display a magnetoresistance when an external field is used to switch between these magnetic orientations. This tunnel magnetoresistance (TMR) is usually defined as the difference in conductance between parallel and antiparallel magnetizations, normalized by the antiparallel conductance:

$$TMR \equiv \frac{G_P - G_{AP}}{G_{AP}} = \frac{R_{AP} - R_P}{R_P} \tag{2.5}$$

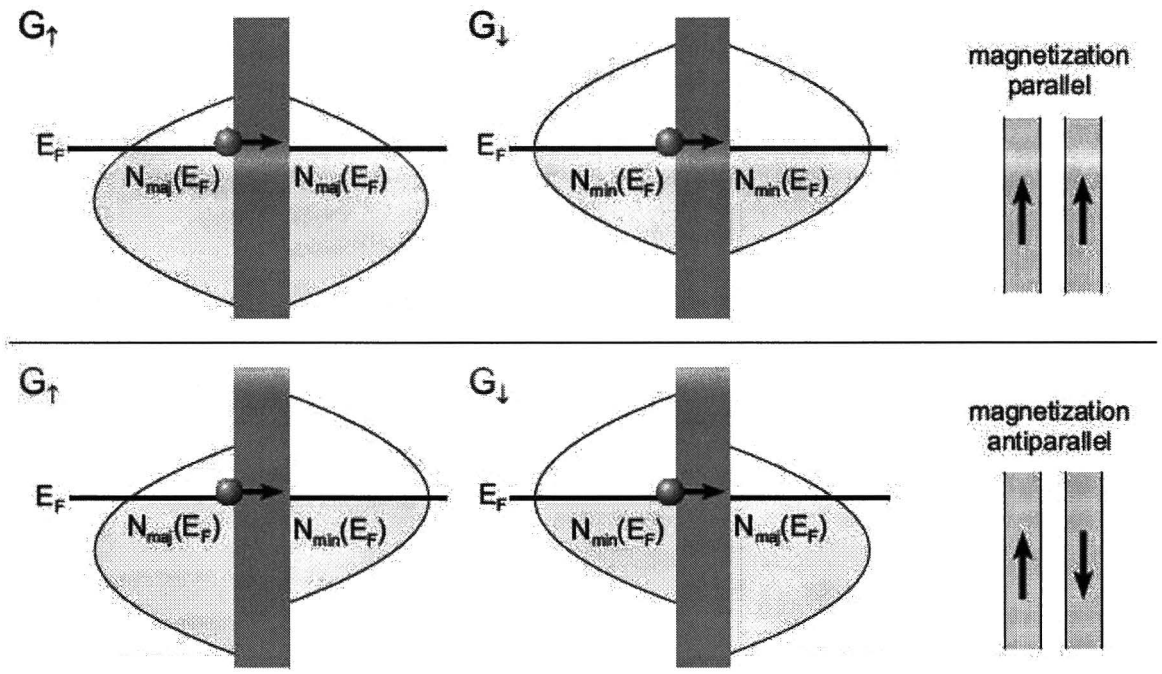

Figure 2.2: Spin-resolved tunneling conductivity G for parallel (top panel) and antiparallel magnetization (bottom), as indicated at right, is proportional to the product of the DOS factors at the Fermi level E_F. The total current in parallel orientation is governed by $N^2_{maj}(E_F) + N^2_{min}(E_F)$, in the antiparallel case by $2N_{maj}(E_F)N_{min}(E_f)$. The voltage that introduces a net tunneling current across the barrier (indicated by the grey bar) is negligible in this schematics, from [8].

Now by using equations 2.3 and 2.4 we can see that we can also write the TMR as follows:

$$TMR = \frac{[N_{maj}(E_F) - N_{min}(E_F)]^2}{[2N_{maj}(E_F)N_{min}(E_F)]} = \frac{2P_L P_R}{1 - P_L P_R} \tag{2.6}$$

Here we have introduced the $P_{L(R)}$ as the tunneling spin polarization (TSP) of the left (right) ferromagnetic electrode. The TSP is defined by Julliere [10] as:

$$P_{Julliere} = \frac{N_{maj}(E_F) - N_{min}(E_F)}{N_{maj}(E_F) + N_{min}(E_F)} \tag{2.7}$$

and is simply the normalized difference in majority and minority DOS at the Fermi level. But we should stress that the $N(E_F)$ is defined here as an effective number of *tunneling* electrons, so that the tunneling process is not only governed by the (static) DOS at E_F. That means that we are not relating the total DOS at the Fermi level to the tunneling process but only those electrons that are able to tunnel through the barrier. We will return to this thoroughly when discussing the effect of a crystalline barrier.

The TSP of individual magnetic electrodes with their barrier can be measured with the so-called superconducting tunneling spectroscopy (STS) technique that uses a superconductor to probe the spin imbalance in tunneling currents. In such an experiment a

magnetic field splits up the sharply-peaked DOS of the superconducting electrode, which leads to an asymmetry in the conductance that reflects the amount of TSP. We will come back to this technique in section 2.3.1.

It seems that we can use the Julliere model as an phenomenological equation that nicely connects the TSP to the magnitude of the magnetoresistance. However, as we will see below, the physics of spin-polarized tunneling is much more complex. In the following sections we will discuss some of these issues listed here in order of importance:

- Relevance of the electronic structure of the barrier. For crystalline MgO we will see that the symmetry contained in certain electronic (Bloch) states is the origin of the huge TMR effect, see section 2.2.
- Relevance of the electronic structure of the electrodes including surface states, see section 2.2.1.
- The electronic coupling of the Bloch states from the electrodes to the barrier.
- Strong dependence of TMR on the applied bias voltage and temperature, see section 2.1.1

To explain these experimental observations we will need a theoretical framework, which will be given in the following sections. All of these issues are naturally related, thereby creating a complex dependence between parameters. But first we give a model that is used to determine certain barrier parameters.

2.1.1 Basic magneto-transport

In this section we take a step back and discuss a model that provides a way to characterize our barriers. The model gives a physical interpretation of the following observed experimental effects:

- The tunneling current I is non-lineair in applied bias voltage V.
- The conductance dI/dV is approximately parabolic in voltage V, except for small bias.

The ohmic behavior as derived in equation 2.2 is only valid for a very small applied bias voltage. At higher voltages the IV behavior becomes non-lineair. For symmetric junctions (identical electrodes) Simmons [11] has analytically calculated the tunneling current using the WKB approximation which is valid for thick and high barriers and is given by:

$$I(V) = \frac{\alpha A}{t^2}\Big(\bar{\phi} - \frac{eV}{2}\Big) \exp\Big[-\beta t\sqrt{\bar{\phi} - \frac{eV}{2}}\Big] - \frac{\alpha A}{t^2}\Big(\bar{\phi} + \frac{eV}{2}\Big) \exp\Big[-\beta t\sqrt{\bar{\phi} + \frac{eV}{2}}\Big] \quad (2.8)$$

with $\alpha = e/(2\pi h)$, $\beta = 4\pi\sqrt{2m_e^*/h}$ (m_e^* the effective electron mass in the barrier conduction band), V the applied voltage, t the barrier thickness, A the barrier area, and $\bar{\phi}$ the average

barrier height above the Fermi level given by $\int_0^t [V(x) - E_F]dx/t$. Again the exponential dependence on the barrier thickness is shown as well as the applied bias voltage. We will use a fit to this equation when we discuss our symmetric tunnel junctions in section 5.3. The Simmons model is later adapted by Brinkman *et al.* [12] to include an asymmetry in the barrier potential ϕ in figure 2.1, with $\Delta\phi$ the potential difference between right and left electrode. The barrier height may also be varying not only due to different electrodes (different work function) but also due to inhomogeneities, for instance in stoichiometry. The tunneling current for asymmetric barriers is approximated by a Taylor expansion to the third power:

$$I(V) = R_0^{-1}\Big[V - \Big(\frac{\beta e\, t\Delta\phi}{48\,\bar{\phi}^{3/2}}\Big)V^2 + \Big(\frac{\beta^2 e^2}{96}\frac{t^2}{\bar{\phi}}\Big)V^3\Big] \tag{2.9}$$

with R_0 the ohmic low-bias resistance of the junction given by:

$$R_0 = \frac{2t\exp\left(\beta t\sqrt{\bar{\phi}}\right)}{eA\alpha\beta\sqrt{\bar{\phi}}} \tag{2.10}$$

which scales inversely with area, and rapidly grows with thickness and height of the barrier. In case of constant barrier height, the current is cubic in applied voltage V, equivalent to a parabolic conductance, one of the basic properties of transport across tunneling barriers:

$$G \equiv \frac{dI}{dV} = \frac{1}{R_0} + \Big(\frac{\beta^2 e^2}{32R_0}\frac{t^2}{\bar{\phi}}\Big)V^2. \tag{2.11}$$

These formulas have been extensively used to study barrier characteristics such as barrier height, asymmetry and the thickness. But one must keep in mind that the model is based on free-electron-like calculations using simple parabolic bands for the metallic electrodes. This means that the spin-dependence of the DOS factors of the magnetic electrodes is not explicitly incorporated in these models. The effect of a crystalline barrier further obscures the free-electron-like approach even more, as will be discussed in section 2.2. And other aspects like tunneling through so called hot spots, i.e. places where the barrier is thinner, hopping conductance though localized states in the barrier due to impurities, the existence of pinholes in the barrier where the conductance is ohmic. All these points makes the application of the discussed models questionable. But the widespread use of the models can be justified in a way that it makes barrier comparison grown in different laboratories possible.

2.1.2 Temperature and bias voltage dependence

Another observation in magnetic tunnel junctions is the dependence of the TMR on the temperature and on the applied bias voltage. From this dependence we can get information on the quality of our barriers. We discuss a commonly used model which gives us some insight in the origin of the experimental observed trends. Also, it provides us some first insight into different conduction mechanisms that are present in tunnel junctions and the behavior of the tunneling spin polarization as a function of temperature.

Temperature dependence

The temperature dependance of the TMR in MTJ's has been an extensively studied topic for AlO_x based junctions, and studies on MgO based junctions are being published as we speak. There are various temperature dependent factors involved in tunneling such as direct tunneling, phonon and magnon assisted tunneling, hopping conductance via localized states in the barrier and spin scattering at magnetic impurities. In literature the resistance or conductance is studied in the parallel and anti-parallel alignment of the magnetization direction of the electrodes. Commonly, the conductance in the parallel alignment is less dependent on temperature than in the anti-parallel alignment and also the conductance is higher at the higher temperatures due to added conduction mechanisms. This already explains the lower TMR ratio's found in the high temperature case, i.e. the extra conductance channels at high temperature are spin independent and therefore constitute a larger part of the total current leading to a lower TMR ratio.

Here, we discuss one of the models that is used to describe the temperature dependent behavior. Let's assume that there are two different contributions to the conductance, i.e. in addition to the direct tunneling channel there is a second spin-independent channel. If we follow the work of Shang et at [13], and Kou et al [14], we can write the conductance as:

$$G(\theta) = G_T(1 + P_1 P_2 cos(\theta)) + G_{SI} \tag{2.12}$$

where θ is the angle between the magnetization directions of the two electrodes. P_1 and P_2 denote the effective tunneling spin polarization (TSP) of the ferromagnetic electrodes and G_T is the prefactor for direct elastic tunneling, while G_{SI} is the spin independent part. Elastic direct tunneling (prefactor G_T) varies slightly with T due to broadening of the Fermi distributions in the electrodes, typically a few percent from $T = 0$K to 300K. Here it is assumed to be constant. The TSP might be considered to decrease with increasing temperature due to spin-wave excitations (Bloch's law):

$$P(T) = P_0(1 - \alpha T^{3/2}) \tag{2.13}$$

where α is a material dependent constant and P_0 is the full effective spin polarization at $T = 0$K. Please note that the conductance described by equation 2.12 with $G_{SI} = 0$ is decreasing with increasing temperature for parallel orientation ($\theta = 0$) and increasing in the anti-parallel orientation ($\theta = \pi$). The second conductance channel is unpolarized and is therefore independent on the magnetization of the electrodes. This spin independent part G_{SI} can be dependent on various physical contributions like non-uniformity in the barrier, misplaced ions at the interface leading to extra surface states. A mechanism that might dominate this channel is hopping through localized states in the barrier. Theoretical work shows that hopping through chains of N localized states results in a power law dependence of G_{SI} on T with an exponent $\gamma(N) = N - 2/(N + 1)$, and is given by:

$$G_{SI}(T) = \sum S_N T^{N-2/(N+1)}, \; N = 1, 2, 3, ... \tag{2.14}$$

The temperature dependence originates from phonon emission or absorption at the transition from the first to the next localized state along the chain, to overcome the energy

difference between the two levels. N=1 leads to $\gamma = 0$ (temperature independent) and for N=2 we find $\gamma = 4/3$. Shang *et al.* (AlO_x) and Kou *et al.* (MgO) both find that the dependence with N greater than 2 does not improve their fitting to the experimental data. For more hopping sites in the barrier we have to add higher terms in our power law dependence as is done for our junctions in section 5.3.

Bias-Voltage dependence

As can be seen from the models described above, the typical behavior of tunneling is contained in the non-linear IV curves. It is well known that TMR also shows a characteristic bias dependence. This dependence of the TMR on the bias voltage, however, originates from the following: On applying higher voltages across the junction we intrinsically change the amount and character of the electronic bands which participate in tunneling i.e. changing the DOS of the electrodes. A clear experimental example of the dependence of the TMR on the bias voltage which is related to the band structure of the electrodes is given by Yuasa *et al.* [15]. This is seen in figure 2.3 where the normalized TMR as function of applied bias voltage is shown for epitaxially grown (001) oriented Fe/MgO/Fe (solid line) and Co/MgO/Co (dotted line) junction. The higher bias dependence of the Co/MgO/Co junction originates from the different band structure. For the details we refer to the paper of Yuasa *et al.* [15].

Also, voltage induced hopping channels can be opened as found for AlO_x junctions by Oliver and Nowak [16] and theoretically explained by Xu *et al.* [17], all leading to the decrease of the observed TMR with increasing applied bias voltage.

The key point of this section is that the conduction in tunnel junctions especially at elevated temperature is related to the observation that TMR is reduced when the temperature or bias voltage is increased. Its origin can be found in extra conduction channels opening up at increasing temperature, and secondly, by applying a bias voltage across a junction the DOS which contribute to tunneling is modified. We will present a study on our junctions in chapter 5.

2.2 Theory of tunneling in crystalline Fe-MgO-Fe MTJ's

As discussed before, the TMR of a MTJ is determined by many physical processes. To explain the recent huge TMR effects, we need the special characteristics of crystalline MgO. The electronic structure at the barrier-electrode interface and the symmetry matching of the electron wave function between the surface and bulk of the MgO and electrode system are crucial in understanding the high TMR and TSP. Based on the first work on decaying electronic states for tunneling in insulators and semiconductors by Mavropoulos *et al.* [18], both Mathon & Umerski [5] and Butler *et al.* [4] theoretically predicted a year later a huge TMR effect in Fe-MgO-Fe magnetic tunnel junctions. This effect originates from coherent (k conserved) spin-dependent tunneling of highly spin-polarized Δ_1 Bloch states of Fe for

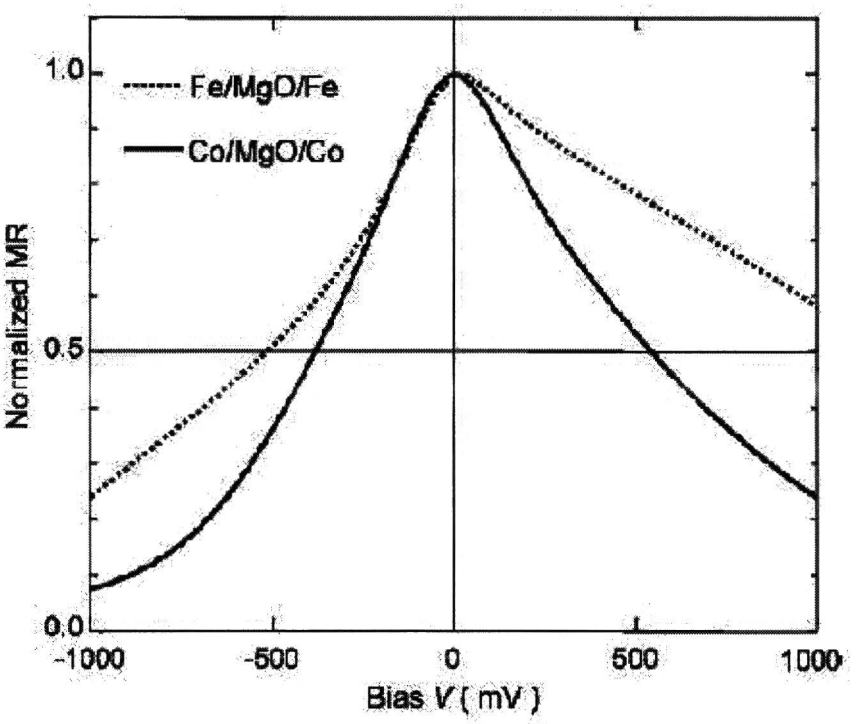

Figure 2.3: Bias voltage dependence of normalized MR ratio at room temperature for Co/MgO/Co MTJ with MgO thickness of 2.2 nm (solid line) and for Fe/MgO/Fe MTJ with MgO thickness of 2.2 nm (dotted line), from [15].

$k_{\|}$=0. In this section, we will try to explain the physics responsible for this effect. We start by giving the conclusion of this section: the huge TMR originates from two physical properties:

- *The presence of certain Bloch states in one spin channel and their absence in the other spin channel.*
- *The filtering of certain Bloch states in the crystalline MgO, i.e. different Bloch states have different decay parameters in the MgO barrier.*

With this in mind, we can start with the complex physics involved. We will explain the theory using the band structure of the materials. First we will explain the individual band structures of the bulk electrode and the MgO barrier. Then we will look at so-called metal induced gap states in the insulating MgO responsible for the tunneling in crystalline MgO. And finally we will combine these systems to form a magnetic tunnel junction with these systems.

2.2.1 Electronic band structure

Understanding the high TMR in Fe-MgO-Fe MTJ's starts with analyzing the electronic band structure of the bulk electrode (Fe) and barrier (MgO). This is directly related to the

crystal structure of the materials. The conduction through the electrodes is characterized by the available states (DOS) at the Fermi level. These states can be divided in Bloch states with specific symmetry based on crystal structure. The same is true for an insulator except that there are no states at the Fermi level. In this case the tunneling is described by decaying Bloch states in the insulator. We will discuss the key properties that are needed for the high TMR from the electronic structure point of view. But first let us look at the epitaxial system of the Fe-MgO-Fe tunnel junction.

Epitaxial Fe-MgO-Fe structure

In this section, we show the epitaxial relation between the crystal systems of Fe and MgO. The unit cell of the crystal lattice of MgO is shown in figure 2.4(a). It has a rocksalt (NaCl) structure which consists of two interpenetrating fcc sub-lattices of metal (Mg) and oxygen (O) atoms displaced relatively to one another by half a lattice spacing of the cubic cell along the [100] direction. In 2.4(b) we see the unit cell of the bcc crystal lattice of Fe. Finally, in figure 2.4(c) we see the epitaxial relation between the Fe-MgO system. It is known for both Fe deposited on MgO(100) and MgO deposited on Fe(100), that Fe[100] is parallel to MgO[110]. As can be seen from figure 2.4(a) and figure 2.4(b), the distance between the atoms in the MgO[110] direction is close to the lattice spacing of Fe[100], resulting in a lattice mismatch of only 3.5 %. In figure 2.4(c), we show the resulting interface structure where the Fe atoms are nearest neighbors of the oxygen atoms, thus the Fe unit cell is rotated 45° with respect to the MgO unit cell. For a full discussion of the epitaxial relation between the two lattices we refer to [4].

The important points to remember from this epitaxial system are:

- The unit cells of the MgO rocksalt and Fe bcc lattice are rotated with 45° along the [001]-axis with respect to each other.
- The [001]-axis is the normal to the barrier plane for both lattices. In reciprocal space this is the k_z direction. The in-plane component in reciprocal space (k_x, k_y) is referred to as k-parallel ($k_{\|}$).

Electronic structure of BCC Fe

The crystal structure for Fe is the body-centred-cubic (bcc) lattice. This was shown in figure 2.4(b); its corresponding Brillouin zone is shown in figure 2.5 showing the symmetry properties of such a bcc lattice. In the Brillouin zone of bcc Fe, we can see the high symmetry points and axes. As we have seen in the epitaxial Fe-MgO-Fe system the [001]-crystal direction is the normal to the barrier plane, so in the direction of k_z we have $k_{\|} = 0$, . In the Brillouin zone this is the direction from the Γ point towards the H point (Δ axis).

Let us for now concentrate only on this direction. The band structure of bcc Fe for this direction is shown in figure 2.6 for the majority and minority channel. Comparing the states that are present at the Fermi level, i.e. the states that contribute to the conduction, we see that in the majority channel we have a Δ_1 state crossing the Fermi level. Note that

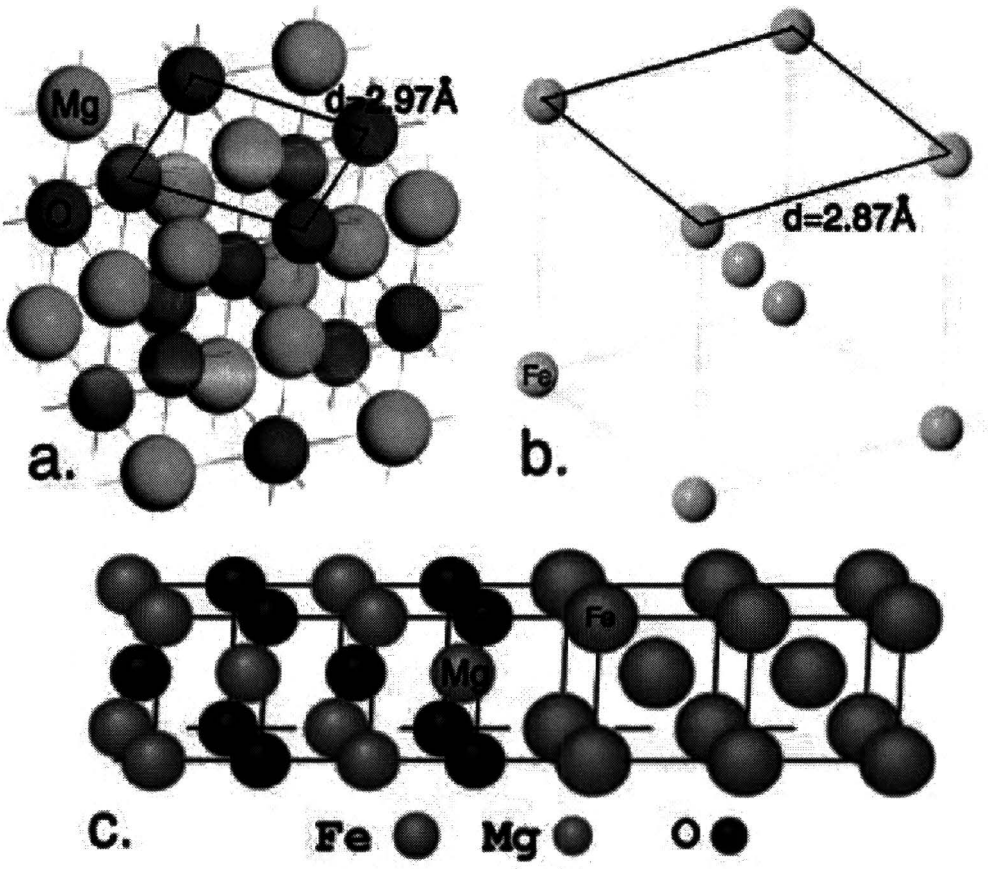

Figure 2.4: (a). Rocksalt MgO, consisting of two interpenetration FCC lattices. (b). Body centered cubic lattice of Fe (c). The epitaxial system of Fe-MgO-Fe, note that the Fe atoms are situated above the oxygen atoms.

these states are not present at the Fermi level in the minority channel. Another feature of this Δ_1 Bloch state is the parabolic shape of the band, resembling free electron like bands (s-like). Note that there are also Δ_5 and $\Delta_{2'}$ Bloch states present at the Fermi level with much flatter bands originating from the localized d and p-like orbitals.

From the band structure, integrating over all directions in the Brillouin zone, we can obtain the DOS of Fe, which is shown for the majority and minority channel in figure 2.7. We see the DOS is labelled according to the symmetry properties of s, p and d-like atomic states, where the e_g (z^2 and $x^2 - y^2$ symmetry) and t_{2g} (yz, zx, xy symmetry) are the DOS for the d-electrons in the Mullikan notation. Comparing the two spin channels, we immediately see the difference in the total DOS (top panel) for the majority and minority channel at the Fermi level (E_F) typical for ferromagnetic materials. But more importantly we also note that the DOS of the s-like states show a significant spin polarization at the Fermi level, that is there is a relatively larger s-like DOS in the majority channel as compared to the minority channel.

We will later see that these DOS features of the electrode, i.e. absence of the Δ_1 state

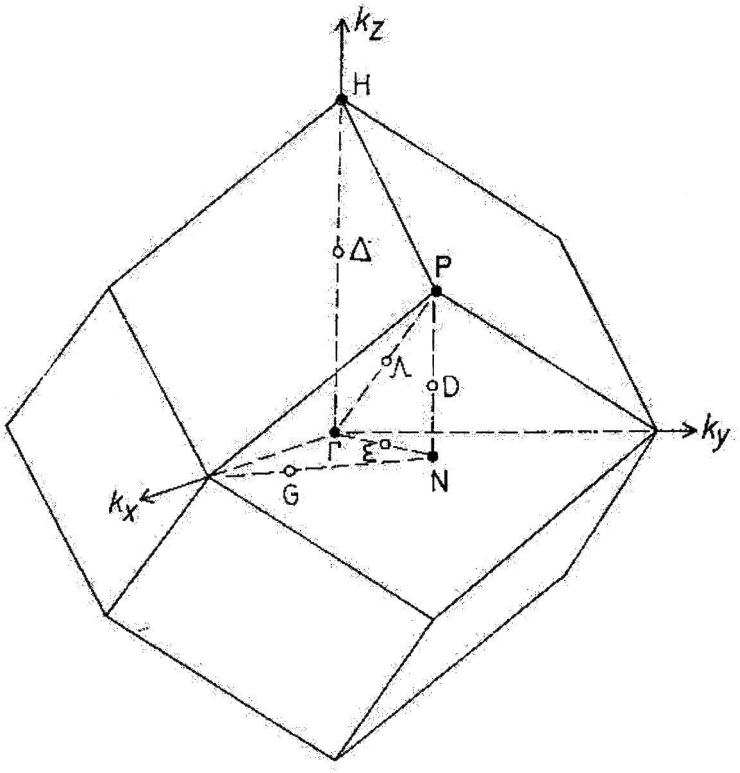

Figure 2.5: Bcc lattice Brillouin zone showing all the high symmetry directions.

in the minority channel and the high polarization in the s-like DOS is one of the reasons for the high TMR ratio obtained in combination with a MgO barrier.

Electronic structure of MgO

Now let's turn to the band structure of MgO; we have seen that its crystal structure is that of rocksalt (NaCl) as shown in figure 2.4(a); the corresponding fcc Brillouin zone is shown in figure 2.8.

MgO is an insulating material with a direct band gap (7.6 eV) which means there are no available states at the Fermi level. A first indication of this can be found by looking at the outer electronic shells of the Mg and O atoms, Mg has a $3s^2$ and O has a $2p^4$ configuration in their outer shells, so in stoichiometric MgO the 2 outer Mg electrons will be transferred to O whereby both elements obtain completely filled outer shells.

The calculated band structure of MgO is given in figure 2.9, where we can clearly see the band gap. Again, we take the Δ axis (Γ to X point) to be aligned with the normal to the barrier plane, so only the right part (Γ to X point) of the figure is important here.

The Fermi level is located halfway in the band gap. The point to remember from this figure is that in the direction of interest, we find at the conduction band (above the band gap) a Δ_1 and $\Delta_{2'}$ band at higher energy. In the valence band (below the band gap) a Δ_1 and Δ_5 band as indicated by the arrows. We will later see that such a position of

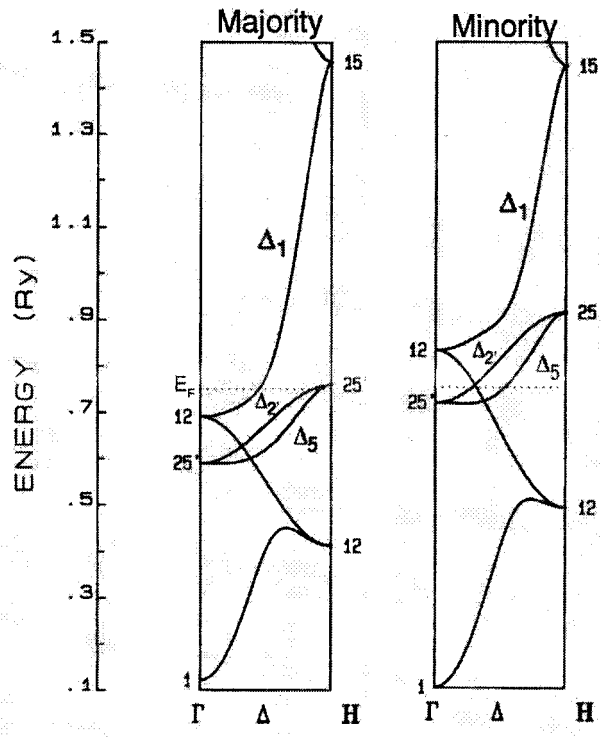

Figure 2.6: The band structure of bcc Fe in the majority (left) and minority (right) channel. The dotted line indicates the Fermi level, from [19].

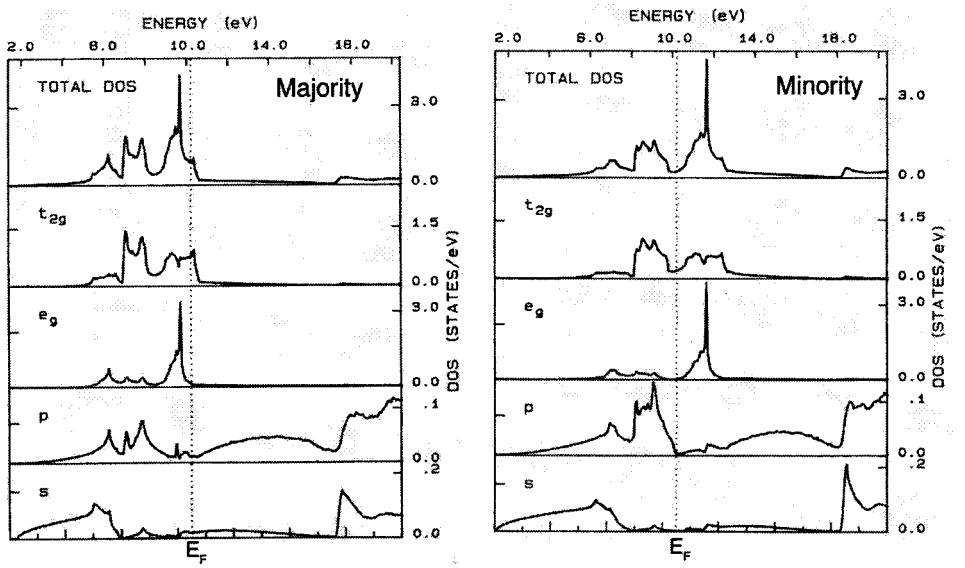

Figure 2.7: The DOS of Fe in the majority (left) and minority (right) channel. Top panel gives the total DOS, where the lower give the d (t_{2g} and e_g) the p and s-DOS, respectively, from [19].

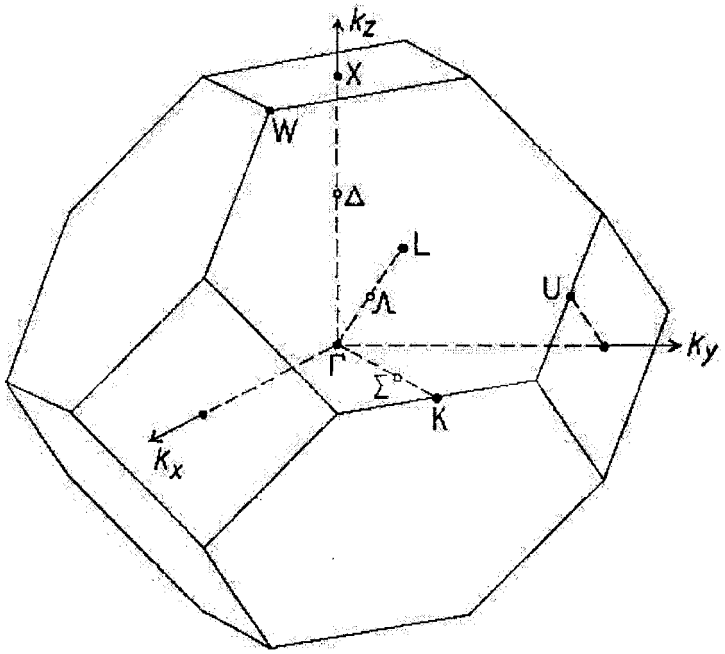

Figure 2.8: Fcc lattice Brillouin zone showing the high symmetry directions.

these conduction and valence band is primarily responsible for the TMR effect and the spin filtering in MgO.

Origin of spin filtering in MgO

We have seen in the bulk MgO band structure that the states present in the valence band and conduction band have certain symmetries. But this does not explain how these states should influence the tunneling current. More specifically, how do these states bring about the spin filter effect which is the origin of the huge TMR in MgO based MTJ's. From the simple WKB model, we have seen that the probability of an electron tunneling through the barrier is dependent on the barrier height, thickness and direction of tunneling. In that section, we noted that this model is still valid but incomplete in the case of crystalline MgO. To understand its shortcomings, we will discuss here the influence of the symmetry of the Bloch states on the tunneling electrons. We will see that the aforementioned Bloch states, in the case of Fe-MgO systems have different decay rates in the barrier leading to a selective filtering of certain Bloch states.

Because there are no allowed states at the Fermi level (in the band gap of MgO) we know that MgO is an insulator. This however, tells us nothing about the possible Bloch states that can tunnel through MgO. In the band gap of MgO, the Bloch states can be represented with imaginary k-vectors, since no real solutions to the Schrödinger equation exist in the gap. The general properties of such imaginary k-vectors can be derived from the bulk band structure of the material, if one formally allows complex k vectors to characterize the

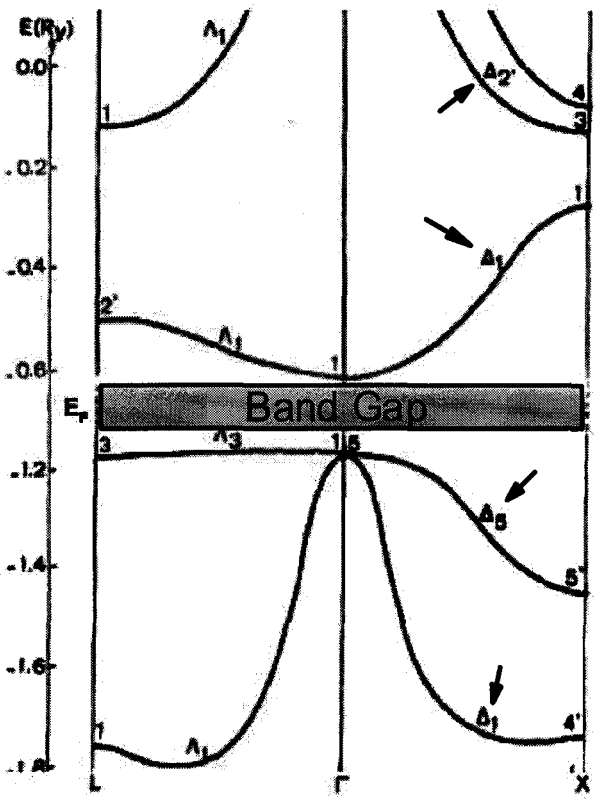

Figure 2.9: Band structure of rocksalt MgO, where we have indicated the important bands with arrows. The Fermi level is located halfway in the bandgap, from [20].

solutions of the Schrödinger equation for the bulk periodic potential. At surfaces and/or interfaces, it can be shown that these states decay evanescently. When a metallic layer is introduced at such a surface or interface, the Fermi level, E_F, lies in the insulator band gap. One can match the wave functions of complex k vectors of the metal Bloch states with those of the barrier. Thus, we describe metal induced gap states (MIGS). More specifically, one can split the wave vector into a component parallel to the barrier-electrode interface, $k_{\|}$, which is conserved during tunneling, and a component perpendicular to the interface, k_z. Then, for each real $k_{\|}$, one can find the dispersion relations $E = E(k_z)$, allowing a complex $k_z = q + i\kappa$. We denote the imaginary part κ of k_z as the *decay parameter* or *attenuation coefficient*. The corresponding wave functions will fall off as $\sim e^{-\kappa z}$ in to the barrier. The solutions of the Schrödinger equation for a certain $k_{\|}$ and arbitrary complex k_z, which are associated with a real valued energy, form the so-called real lines in the three dimensional (q, κ, E) space. For a complete discussion on MIGS we refer to Mavropoulos *et al.* [18].

The importance of κ can be understood by considering that the interface-induced changes in the charge density and atomic potentials are confined primarily to the first couple of monolayers across the interface, but the evanescent wave functions themselves, which fall off as $\sim e^{-\kappa z}$, extend over many layers into the barrier, and therefore represent

solutions of the bulk Schrödinger equation.

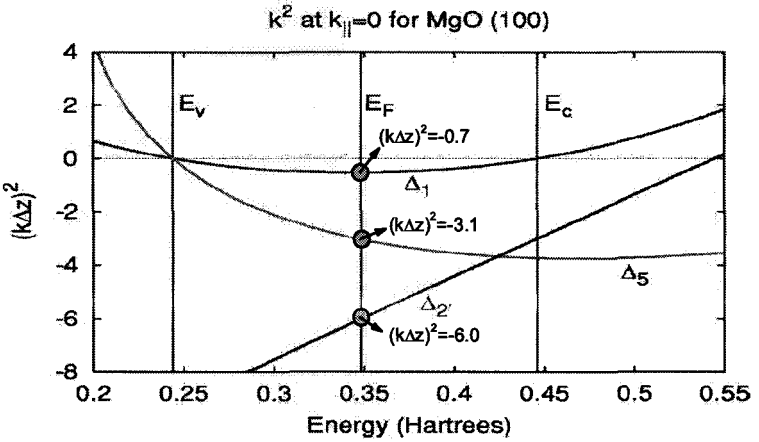

Figure 2.10: Dispersion $k^2(E)$ for MgO in the vicinity of the gap along Δ (100). Negative values of k^2 determine the exponential decay rates for various Bloch states. E_v is top of valence band. E_c is the bottom of the conduction band, from [4].

In case of MgO, after solving the complete solutions to the Schrödinger equation for the electrode-barrier-electrode interface, it turns out that the decay rates for different Bloch states emanating from the Fe(001) surface is significantly different. These decay rates for each of the Fe(001) Bloch states within the MgO can be determined by inspection of the band structure, as is illustrated in figure 2.10. In this figure, $k^2(E)$ along the Δ direction is plotted for energies in the vicinity of the gap for bulk MgO. The figure shows $(k\Delta z)^2$ where Δz is the interplanar spacing for MgO(001) (2.1Å) and k is in the (001) direction. The figure shows $(k\Delta z)^2$ calculated for three Fe Bloch state symmetries (Δ_1, Δ_5 and $\Delta_{2'}$). The energy range for which all values of k^2 are less then zero ($E_V < E < E_C$) is defined as the energy gap. It can be shown that the lowest decay rate are found for those states with the lowest value of $(k\Delta z)^2$. In case of bcc Fe, this is true for the Δ_1 Bloch states. The decay parameter for these states can be calculated from the $(k\Delta z)^2$ value at the Fermi level E_F. For the Δ_1 state this gives $\kappa\Delta z = \sqrt{-(k_{\Delta_1}\Delta z)^2} \approx 1.47$. This comes by using $\Delta z = 2.1\mathring{A}$ and κ can be read from figure 2.10 to be equal to 0.7. Reading κ for the other Bloch states, we find larger decay rates for the other Bloch states (6.5 for Δ_5 and 12.6 for $\Delta_{2'}$).

To put it simply, the impinging Bloch wave functions "see" different effective barrier heights, thus decaying differently in our simple quantum mechanical textbook example. The tunneling probability for these states is then different and is characterized by the decay parameter κ.

Labelling of the symmetry states

Now let us look at the characteristics of these Δ bands. Their nomenclature originates from group theory and was established by Bouckaert, Smoluchowski and Wigner in 1936

[21]. The Δ indicates a direction of high symmetry in the Brillouin zone and the suffix denotes certain symmetry properties. From our first inspection of the bands in the band structures of Fe (figure 2.6) and MgO (figure 2.9), we can say that the Δ_1 band has an s-like character due to the parabolic shape, where the Δ_2, $\Delta_{2'}$ and Δ_5 bands are flatter, which indicates more localized states related to a p and d-like character. These symmetries can be described within group theory as to how the wave function behaves after applying spatial transformations; a certain symmetry then occupies a certain suffix. We will look at these symmetries and explain them related to the FCC Brillouin zone of the MgO barrier as shown in figure 2.8. The character of the Bloch states under certain spatial transformation are listed in table 2.1. The spatial operation of these transformations are listed in table 2.2.

Δ	E	C_4^2	$2C_4$	$2JC_4^2$	$2JC_2$	basis function	orbital
Δ_1	1	1	1	1	1	1	s-like
Δ_2	1	1	-1	1	-1	x^2-y^2	d-like
$\Delta_{2'}$	1	1	-1	-1	1	xy	d-like
$\Delta_{1'}$	1	1	1	-1	-1	$xy(x^2-y^2)$	d-like
Δ_5	2	-2	0	0	0	$\{x,y\}$	p-like

Table 2.1: Character for the small representation of Δ. And the corresponding basis functions.

Element	Transformation
E	Identity operator (dimension/degeneracy)
C_4^2	Rotation by π about 4-fold axis Δ
C_4	Rotation by $\pm\pi/2$ about 4-fold axis Δ
J	Inversion operator
JC_4^2	Reflection in symmetry plane perpendicular to 4-fold axis Δ
JC_2	Reflection in symmetry plane perpendicular to 2-fold axis Σ

Table 2.2: The spatial symmetry operations.

Table 2.1 thus gives the character of the irreducible representations for the group shown in the upper left corner (group Δ). The corresponding representations will be the "small representations" (Δ_n) characterizing the Brillouin zone. The upper right corner contains the group elements (spatial transformations) as listed in 2.2. The symmetry types, or basis functions can now be identified and are listed in the last two columns of table 2.1.

Now let us visualize some of these symmetries, first the Δ_1 has the highest symmetry along the Δ axis. This is related to s-like character (spherically symmetric) but also the p_z and the d_{z^2} are in the Δ_1 band, i.e. they have the same character under the transformations. So let us look at two atomic d-orbitals, viz. d_{z^2} and d_{xy} how they behave under the spatial transformations as shown in figure 2.11.

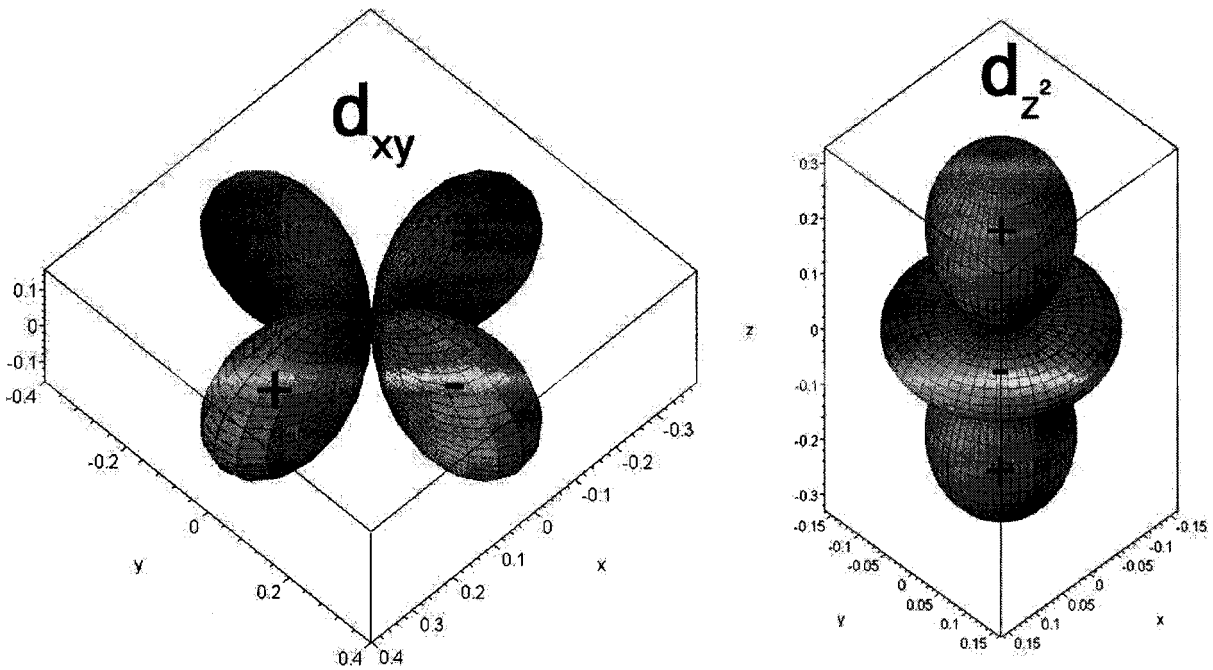

Figure 2.11: The d_{xy} and d_{z^2} orbitals. The + and - indicate the sign of the wave function.

Now let us apply the spatial transformations as described in table 2.1 on these orbitals

.

- E, the identity operator and gives the dimension, for d_{xy} and for d_{z^2} this is equal to 1, i.e. there is only one way of fitting the orbital in the Brillouin zone without overlapping.
- C_4^2, by rotating both orbitals by π about the Δ axis (=z-axis) we find the same wave functions. So the character is 1 for both orbitals.
- C_4, by rotating d_{xy} by $\pi/2$ we find the orbital with inverse sign, giving -1. For d_{z^2} there is no change so the character is 1.
- JC_4^2, for the reflection in the symmetry plane perpendicular to the delta axis we find the same sign for d_{xy} giving 1, and again the same sign for d_{z^2} so 1.
- JC_2, the reflection in the plane perpendicular to the Σ axis (y=$\pm$x axis) gives -1 for d_{xy} and 1 for d_{z^2} symmetry.

Summarizing, for the d_z^2 orbital this gives a character of 1 for all the spatial transformations and comparing with table 2.2 we allocate this function to the Δ_1 band. For the d_{xy} orbital we find 1, 1, -1, 1, -1, this compares to the characters of the Δ_2 band. Remember that in our epitaxial system the unit cell of MgO is rotated with 45° to the unit cell of Fe, this means that Δ_2 states in the Fe couple to $\Delta_{2'}$ states in MgO. In figure 2.12, we show an overview of the most important Bloch states in the Fe and MgO systems.

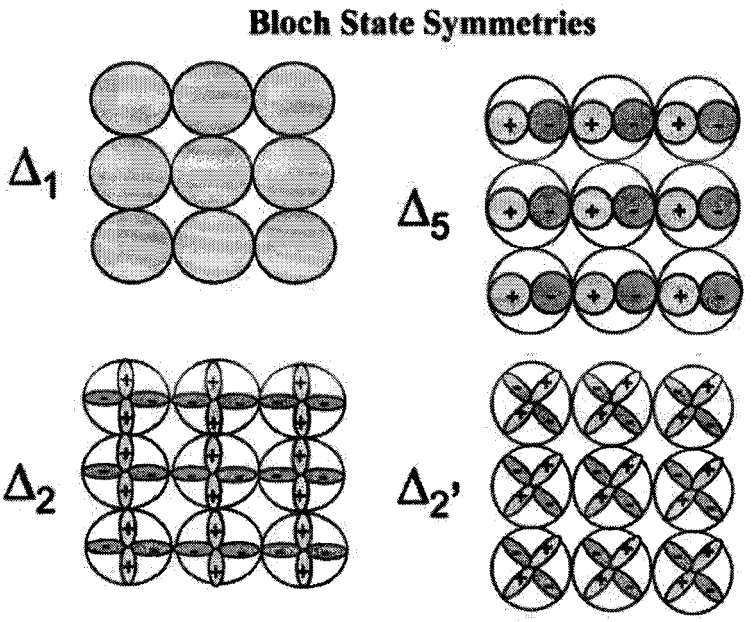

Figure 2.12: Some of the possible propagating Bloch waves in the [001] direction of MgO. The + and - indicate the sign of the wave function, from [22].

From the above discussions, we see that there are compatible Bloch states in the Fe and MgO, with different decay parameters. We can make use of this fact by combining these systems to a MTJ as is done in the next section.

2.2.2 Fe-MgO-Fe system

Here, we will discuss what happens when we combine the Fe and MgO systems to form a tunnel junction. Assuming epitaxial systems, as discussed in the last section, Butler *et al.* [4] calculated the tunneling DOS (TDOS) for the most important Bloch states as a function of the layer thickness in a tunnel junction. This can be seen in figure 2.13, where we see four panels, each describing the TDOS as function of the layers in the Fe-MgO-Fe in the parallel and anti-parallel alignment of the magnetic moments.

We first consider the upper panels which show the TDOS for parallel alignment of the magnetic moment in the electrodes. Remember that the Bloch states are labelled according to the symmetry they have in the left Fe electrode. Also, note that the decay of the TDOS is exponentially dependent on the MgO barriers thickness, as was already seen in the text book example. We will first discuss the top two panels for parallel alignment:

- In the upper left panel we see that in the majority channel for parallel alignment, we find a slowly decaying Δ_1 state. As we know from Fe band structure the Δ_1 state is completely absent in the minority channel shown in the upper right panel. The next slowest decay is that of the Δ_5 states, which is present in both channels.

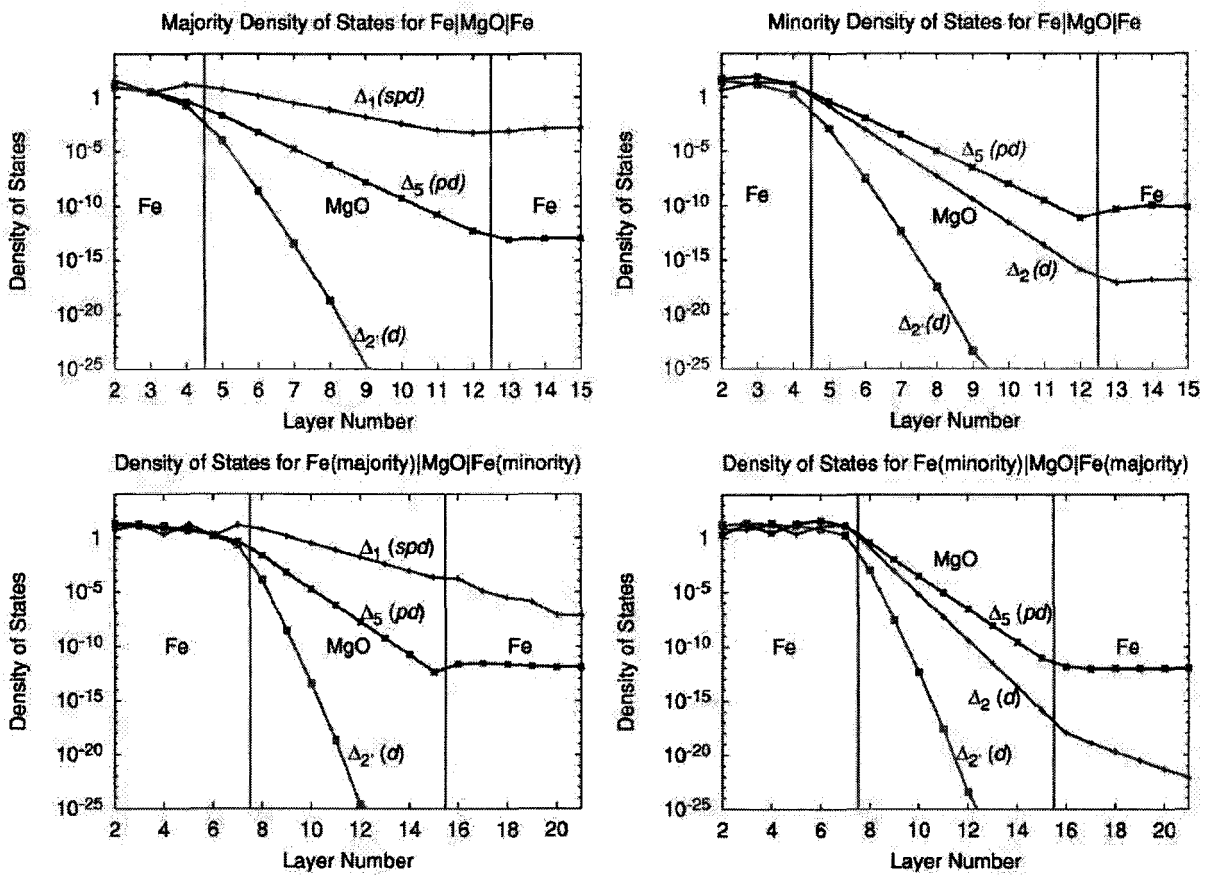

Figure 2.13: Tunneling DOS for $k_{\|} = 0$ for Fe-MgO-Fe. The four panels show the TDOS for majority (upper left) minority (upper right), and antiparallel alignment of the moments in the two electrodes (lower panels). Additional Fe layers are included in the lower panels to show the TDOS variation in the Fe. Each TDOS curve is labelled by the symmetry of the incident Bloch state in the left electrode, from [4].

- Then, we have the $\Delta_{2'}$ state that is also present in both channels and couple to the Δ_2 state in the MgO. These decay very rapidly in the MgO because there are no Δ_2 states near the Fermi energy in the MgO, i.e. in the valence or conduction band (see figure 2.10).
- Next we find in the upper right panel the minority Δ_2 state which couples to a $\Delta_{2'}$ in the MgO but decays faster than the Δ_5 state but not so fast as the Δ_2 state.

This means that the conduction in the parallel alignment is dominated by the Δ_1 state in the majority channel. Now we switch the magnetization direction of the right electrode, i.e. anti-parallel alignment. We are now tunneling from the majority (minority) channel in the left electrode to the minority (majority) channel in the right electrode. This is shown in the lower two panels of figure 2.13.

- In the lower left panel, we see the TDOS for tunneling from the left majority channel into the minority channel of the right Fe electrode. Naturally we see the same Bloch states as in the parallel case and the Δ_1 state shows the same decay in the MgO barrier. The big difference however, is that the Δ_1 state keeps decaying *in* the minority channel the right Fe electrode because there are no Δ_1 compatible states available. They are reflected at the second interface due to the absence of available Δ_1 states in the minority channel of the right Fe electrode.

- In the bottom right panel, we see the TDOS for tunneling from the minority channel in the left electrode to the majority channel in the right electrode. Again we see the same states as in the parallel case. However, the Δ_2 state now sees a reflection at the right interface due to the absence of these states in the majority channel of Fe. However, this does not change the conductance much due to the already strongly decaying nature of the Δ_2 states in the MgO.

In summary, this shows that the conductance when the electrodes are aligned parallel is high, i.e. gives a low resistance due to the high TDOS in primarily the Δ_1 channel. In the anti-parallel case, we find a higher resistance due to the significantly lower conductance in the available channels. This originates from the reflection of the Δ_1 and Δ_2 states at the interface with the right electrode due to the absence of these Bloch states in the minority channel of the Fe.

From this discussion, we have shown the effect of the MgO barrier for electrons tunneling along $k_{||} = 0$. The process is best described along this direction and shows the physical origin of the huge TMR effect. In the next section we generalize the picture by also introducing tunneling for electrons that have a component in the $k_{||}$ direction, that is $k_{||} \neq 0$.

Tunneling for $k_{||} \neq 0$

Until now we have considered tunneling along $k_{||} = 0$, from which we can understand the underlying physics. For completeness let us look at the transmission probability for $k_{||} \neq 0$. As we have seen from the quantum mechanical textbook example the probability for $k_{||} \neq 0$ decreases rapidly with increasing $k_{||}$. In the paper from Butler *et al.* [4] the transmission probability is plotted as a function of k_x and k_y for different MgO thicknesses; this can be seen in figure 2.14. Remember that we defined $k_{||} = 0$ as $k_x = k_y = 0$. In (a) and (b) we see the transmission probability for the majority channel and minority channel, respectively, for parallel aligned magnetic moments, in (c) it is plotted for the anti-parallel alignment, integrated over both conducting channels. Note the different z-axis scales between the plots for the different barrier thicknesses indicated by the transmission multiplication factor. In the following items we discuss the transmission probability for these cases.

- The transmission probability in (a) is rather similar to tunneling through a simple square barrier. For a few MgO layers it is a rather broad peak concentrated at $k_{||} = 0$,

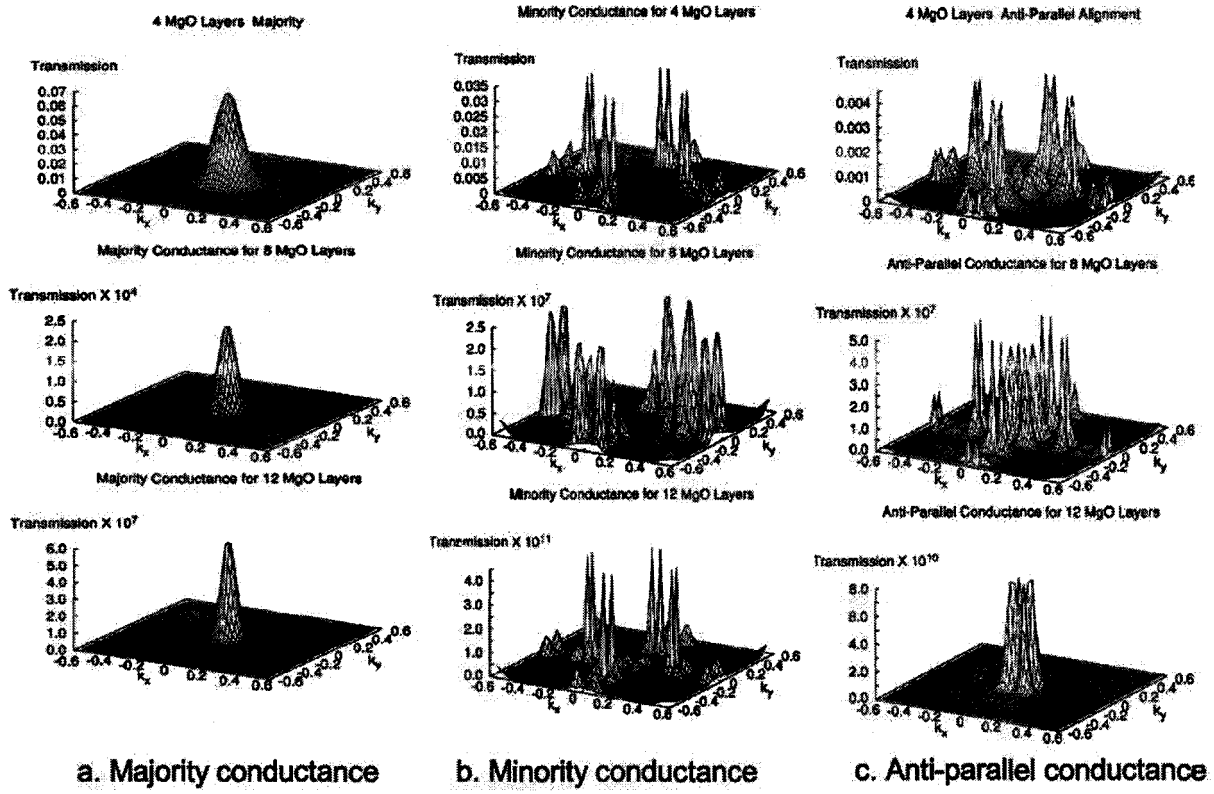

Figure 2.14: Calculated transmission probability for 4, 8 and 12 layers of MgO as a function of k_x and k_y. (a). for the majority channel (parallel alignment), (b). for the minority channel (parallel alignment), (c). for anti-parallel alignment, integrated over both conduction channels, from [4].

just like we have seen in the textbook example. The probability becomes sharper with increasing barrier thickness as we have seen.

- If we now look at the transmission probability in the minority channel in (b), it is completely different. The complicated sharply peaked structure arises from the interplay of interfacial resonance states, the $k_{\|}$ dependence of the wave function decay in the MgO, and the symmetry of the minority Fe Bloch states relative to that of the complex energy bands of MgO. The important point from this figure is the change of the scale with increasing barrier thickness. For only 4 layers of MgO we see that the peak transmission in the minority channel is half that of the majority channel. On increasing the barrier thickness we see that the ratio between these two increases to 10^3 and 10^4 for the 8 and 12 layers respectively, indicating the sensitivity to the surface states when the barrier is very thin.

- In (c) the transmission probability for the anti-parallel alignment of the magnetic moments in the electrodes is shown. Here we see a combination of the features

observed in the majority and minority channels. For a thinner barrier the highest transmission is near the line $k_y = 0$ and $k_x = 0$. As the barrier becomes thicker the highest transmission occurs closer to the origin due to the slow decay in the MgO of states derived from the Fe majority Δ_1 band. Even for the thickest MgO barrier however, the maximum conductance for antiparallel alignment does not occur exactly at $k_{||} = 0$. The reason for this can be understood from the bottom two panels of figure 2.13 which show the TDOS for antiparallel alignment and $k_{||} = 0$. The total band-to-band transmission probability is the same whether calculated for electrons going left to right or right to left. This implies of course, that one must have bands of the same symmetry on both sides in order for electrons to be transmitted. The Δ_1 electrons readily enter the MgO where they decay slowly with distance as discussed before. On the right-hand side of the barrier however these states cannot propagate because there are no minority Δ_1 propagating states at the Fermi energy. Therefore they continue to decay within the minority Fe leading to total reflection of the Δ_1 Bloch state.

From these figures, it is clear that the theoretical predicted magnetoresistance is very high. The phenomenological picture can be understood from the tunneling at $k_{||} = 0$ but for the complete calculation we must include tunneling for $k_{||} \neq 0$.

Concluding, the TMR is a direct consequence of the two aforementioned properties:

- *The presence of certain Bloch states in one spin channel and their absence in the other spin channel.*
- *The filtering of certain Bloch states in the crystalline MgO, i.e. different Bloch states have different decay parameters in the MgO barrier.*

Experimental realization

In the original papers from Umerski and Mathon [5] and Butler *et al.* [4] a large discussion was devoted to the concept of coherent tunneling. They theoretically show that relative amount of electrons tunneling along $k_{||} = 0$ is dependent on MgO thickness (as we have seen), and that the TMR should keep increasing with MgO thickness. They also predict an oscillation in the TMR with increasing MgO thickness. Both these theoretical predictions were experimentally shown by Yuasa *et al.* [7]. They fabricated single-crystalline Fe-MgO-Fe tunnel junctions by using molecular beam epitaxy with a MgO thickness in the range of 1.2 to 3.2 nm. They show that the TMR increases as a function of MgO thickness as expected. However, it saturates to a value of 180% above 2.5 nm at room temperature.

The increase in the TMR can be understood as follows; when the tunnel barrier is thick, the tunneling current is dominated by electrons with their momentum vector normal to the barrier, $k_{||} = 0$. When the barrier is made thinner, the probability for tunneling along $k_{||}$ increases which leads to an increased tunneling in the other Bloch states. Now the ratio between the tunneling through the Δ_1 and the other Bloch states (filtering effect) is lower

and therefore the TMR will be lower. They also show the predicted oscillation in the TMR as a function of thickness, which can be pointed out as evidence for the concept of the conservation of the electron momentum throughout the whole tunneling process leading to interference effects between the tunneling Bloch states. This is however beyond the scope of this master thesis. For further reading we refer to the mentioned papers.

Very recently Mathon and Umerski [23] give a theoretical interpretation of the saturation in the TMR at 180% by Yuasa *et al.* [7] which is much lower as the theoretically predicted magnitude larger than 1500%. They calculate the TMR of a junction where there is a significant amount of intermixing between the Fe and Mg atoms at the interface. It is shown that 16% intermixing shows good agreement between the experimental data of Yuasa and their calculations.

2.3 Experimental techniques

In this section we discuss the experimental techniques used and, where necessary, explain the physics behind the technique.

2.3.1 Superconducting Tunneling Spectroscopy (STS)

Here we discuss a method to directly measure the tunneling spin polarization (TSP). Such a measurement is done by using superconducting tunneling spectroscopy (STS), a technique explored by Maservey and Tedrow [24] and now used as a standard technique to measure the TSP of a electrode-barrier system. For a thorough review we refer to the PhD thesis work of Kant [25] and Kaiser [26] and the aforementioned review paper of Maservey and Tedrow [24] and Swagten [27]. In this technique one of the magnetic electrodes in a tunnel junction is replaced by a superconductor which is used as a detector for the spin polarization of the electrode-barrier system. As derived in equation 2.6 the TSP is a function of the tunneling probability and the density-of-state factors. If we now introduce the superconductor as a detector we can write the tunneling conductance as:

$$G \propto N(E_F)T(\phi, t)\rho(eV) \tag{2.15}$$

where $N(E_F)$ is the DOS at the Fermi level of the magnetic metal electrode, $\rho(eV)$ the superconduction DOS at an energy eV, with V the bias voltage between superconductor and magnetic metal. It is crucial to note that the magnitude of Δ (here the energy gap of the superconductor) is typically around 1 meV, whereas the DOS of a metal shows variations on an energy scale of eV's. A measurement of the conductance is therefore a direct reflection of the DOS of the superconductor, having sharp peaks at an energy $\pm\Delta$, the energy difference between the energy level of the Cooper pairs and the single-electron states (see figure 2.15a). Only at voltages exceeding $\pm\Delta/e$ the electrons can tunnel into the empty single-electron states of the superconductor or vice versa from the superconductor towards the metal. As a result the conductance in equation 2.15 exclusively reflects the

peak shaped DOS of the superconductor. At finite temperatures thermal broadening of the Fermi level reduces the sharpness of the peaks as can be seen in figure 2.15a.

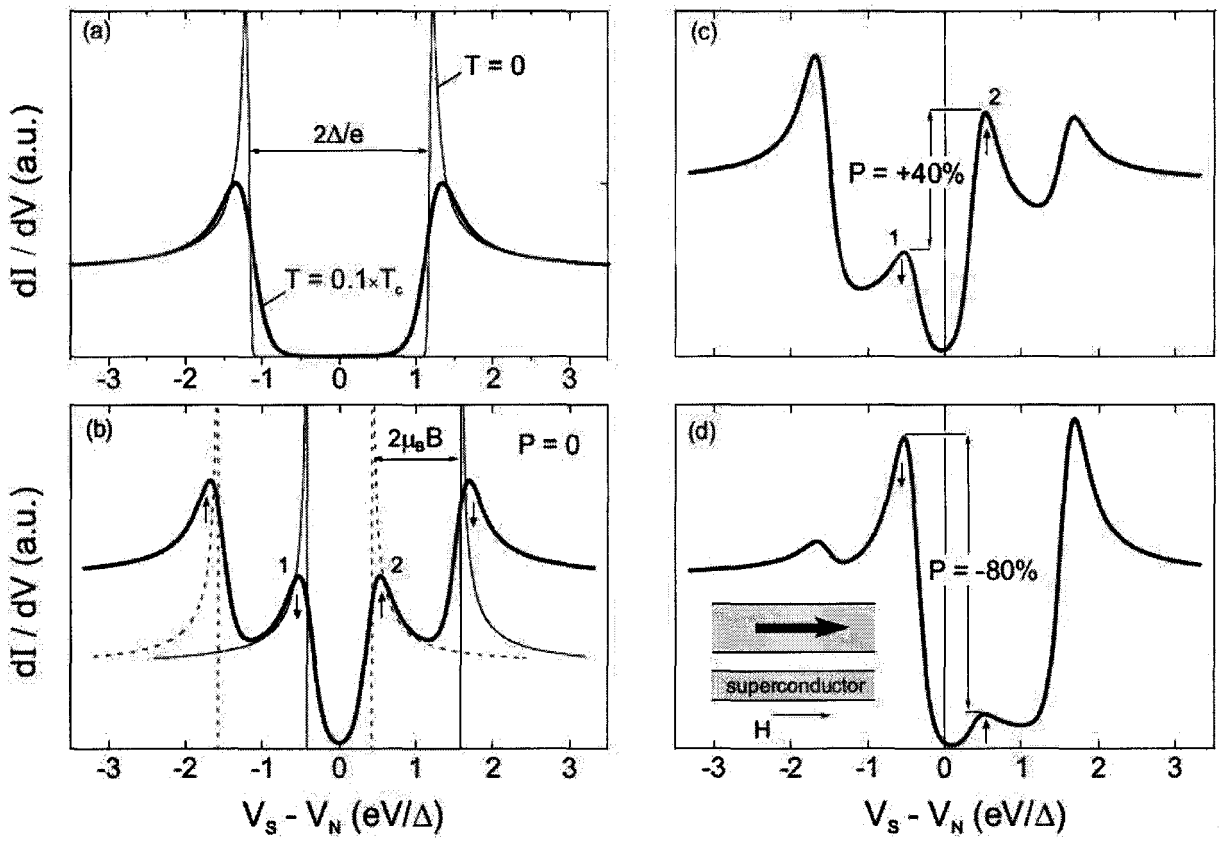

Figure 2.15: Simulated conductance of a superconductor-metal tunnel junction as sketched in the bottom right panel. In part (a) the zero-field conductance is shown both at 0 K (thin line) and at $T = 0.1T_c$ (rounded curve). In panel (b)-(d) the spin-up and spin-down DOS in the superconductor are Zeeman split by a magnetic field B ($\mu_B = 0.6\Delta$) at $T = 0.1T_c$. The polarization of the tunneling electrons is zero in (b), +40% in (c), and -80% in (d). The thin dashed and solid line in graph (b) represent the conductance due to individual spin-up and spin-down DOS, respectively, both at 0K.

The DOS of any metal $N(E)$ as observed in the conductance measurement is the sum of the spin-up and spin-down states. If we now apply a field in the plane of the superconductor, the spin-up and spin-down states will be split up in energy ($= 2\mu_B B$) through the zeeman-splitting as shown in figure 2.15b where μ_B is the electron magnetic moment. For a normal metal (equal spin-up, spin-down conductance). Here we see that the position of the maximum at position 1 reflects the conductance in the spin-down channel, and the maximum at position 2 the conductance in the spin-up channel. If we use a ferromagnetic electrode we find the figures 2.15c and d, here the conductance for the spin-up and spin-down channel are assumed unequal. The ratio between these peaks is a

measure of the TSP, in (c) we see a polarization of +40% and in (d) we see a negative polarization of -80%, in the latter case the conductance is thus dominated by minority electrons.

A more accurate measure of the polarization can be obtained by fitting to a model based on the Maki theory (see [28] and [29]) which also incorporates parameters like spin-orbit scattering and orbital depairing in the superconductor. Spin-orbit scattering scales with the atomic number of the superconductor and the orbital depairing originates from the applied field, which induces an orbital motion of the electrons through the Lorentz force, breaking up (depair) the Cooper pairs [30]. In section 5.4 we will discuss the results of the STS measurements on MgO based junctions.

2.3.2 Magneto Optical Kerr Effect (MOKE)

The magneto-optical Kerr effect (MOKE) is used for measuring the behavior of the magnetization of the magnetic electrodes. The MOKE technique exploits the change in optical polarization of light reflected from a magnetic surface and the change of the polarization after reflection relative to the polarization of the incident beam is analyzed. The change in polarization can either be a rotation about the polarization axis (Kerr-rotation) or a change from linear to elliptical polarization (Kerr elipticity). MOKE gives an indirect measure of the absolute magnetic moment because it is only proportional to the layer magnetization. It is, however, a fast analysis technique. The fact that the measurement is confined to a small laser spot ($\sim 100\ \mu$m) makes it a local technique, only the magnetization at the point is measured. This makes the measurement of layer wedges (varying thickness) and local points on a sample possible. For a thorough description of the MOKE technique please refer to [31].

In figure 2.16, we see a typical magnetization loop. The coercivity (H_c) is the opening of the curve and is a measure of the magnetic "strength" needed to switch the magnetization direction. In section 5.1 we discuss the results obtained for our engineered magnetic layers.

2.3.3 X-ray Diffraction (XRD)

The X-ray diffraction (XRD) technique is used for two purposes in this thesis. First it is used to determine the layer thickness of sputter deposited layers, thereby obtaining the growth rate. Secondly, it also provides information on the crystalline properties of the material. The principle of XRD is based on the interference of X-rays that are reflected from a crystal-lattice or a layer interface.

When we use XRD in a grazing angle incidence configuration, which means that the source and the detector are almost in the same plane as the sample (glancing incidence), we are able to probe the layer thickness. This is possible due to interference of the reflected X-rays on the interfaces of the different layers. This can be described by Bragg's law which relates the angle of constructive and destructive interferance to the layer thickness. The experimental results are compared with simulated data using GIXA (glancing incidence X-ray analysis) software which is used to estimate the layer thickness and gives an indication

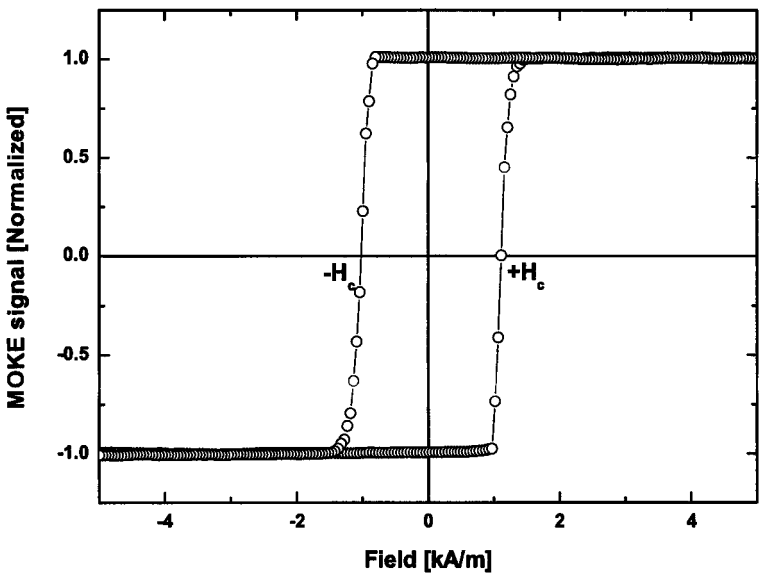

Figure 2.16: Experimental MOKE-loop of a 150Å thick CoFeB film in a magnetic tunnel junction. The hysteresis-loop is characterized by the coercivity H_c.

for the roughness of the samples. The application of XRD is typically limited to films of 100-1000 Å, for thinner films the oscillation period in the reflected intensity (constructive interference) is too long to obtain a good measure, and for very thick films the resolution is insufficient to discriminate the oscillations. Obviously, this typical thickness regime depends on the roughness of the films. In the next section the calibration of thickness of a Ta film with an glancing incidence X-ray measurement is described.

In the second case we use XRD in the high angle configuration, here the detector and source make a high angle with the sample surface. In this case we can probe the crystal structure of our films. This is possible due to the diffraction on the crystal planes. Also poly-crystalline films can be measured; in these films the crystallization is divided into regions where the crystal has different orientations. A measure of the size of these grains is obtained with the so-called Scherrer formula [32]. Also, the position and the shape of the reflected X-ray peak gives information on the crystalline nature of the films. For an in-depth treatment on XRD techniques please refer to Cullity [32]; see section 4.1.3 for the discussion on our films.

Growth rate calibration

To determine the thickness of the thin films we use low angle XRD; in figure 2.17 we see a measurement on a Ta thin film. The oscillations in intensity can be described by Bragg's law, this is done by simulating the oscillation period with GIXA. From this we can determine the thickness of the layer; the angle where the oscillations die out gives a measure of the roughness. The simulation with GIXA gives a thickness of 600Å. This technique is primarily used to calibrate the growth rate. As indicated in the figure we have

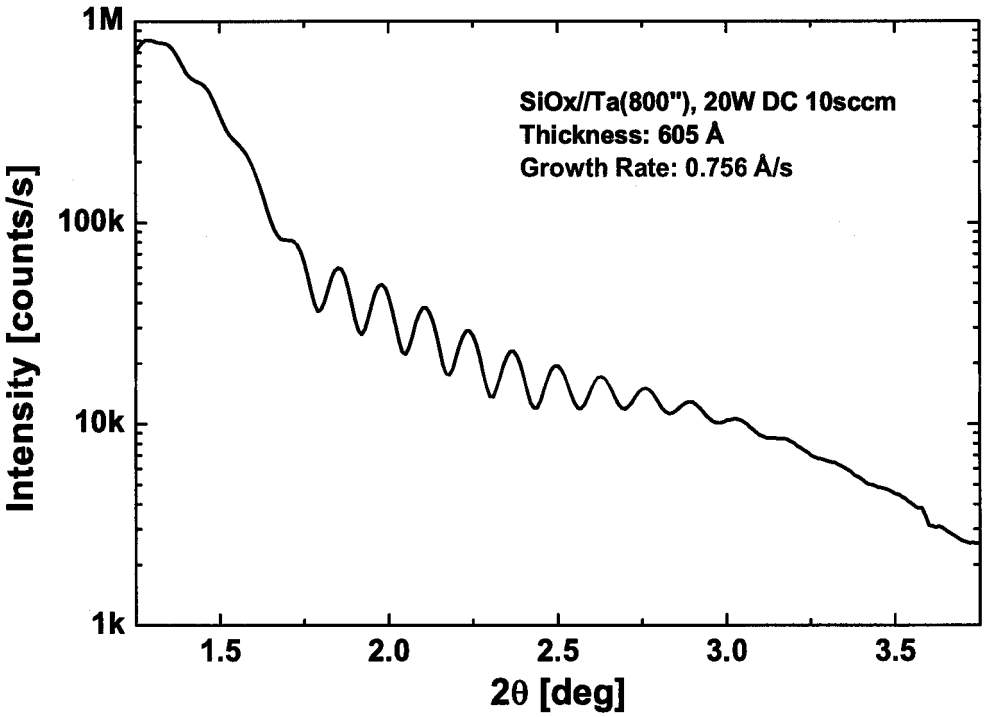

Figure 2.17: Intensity as function of 2θ for a Ta layer deposited for 800 seconds at 20W DC plasma parameters and 10 sccm Ar gas flow on a SiO_x substrate.

deposited for 800 seconds at a DC plasma power of 20W and an argon flow rate of 10 sccm which results in a growth rate of 0.76Å/s for Ta. We use this technique to calibrate the growth rate of all our sputter deposited materials.

2.3.4 Sputter deposition

Sputtering deposition is one of the most commonly used methods for the deposition of thin films. The simplest sputtering technique is by using a simple DC glow discharge (plasma). A plasma is created near a sputter material (target) surface. The high energetic plasma ions (usually from the noble gas argon (Ar)), hit the surface and thereby eject a target atom and electrons called secondary electrons. This ejected atom can be incorporated on a substrate if it is placed in the line of sight of the ejected atoms. This means that the pressure of the inert sputter gas should be low enough so that the mean free path of the atoms is long enough to reach the substrate, but high enough to maintain a steady discharge of the plasma. Typical pressures are in the range of $10^{-3} - 10^{-2}$ mbar. To concentrate the plasma to the target surface a so called magnetron is used, this means that magnets are placed behind the target; they produce a magnetic field which concentrates the ion bombardment to the target surface.

Let us now describe a typical DC sputtering process; we first pump down the chamber to eliminate any contaminating or reactive gases. Then we introduce ultra pure argon

gas and apply a DC power to the target and initially a very small current flows through the system due to the limited amount of charge carriers in the system. As the voltage increases, more and more charge carriers are created due to the secondary electrons that are emitted from the target and partly from impact ionization. As a result the current rises and a discharge is created, leading to a steady state situation where normal sputtering takes place. The sputter rate can now be controlled by the power put into the plasma or the pressure of the sputter gas. Increasing the pressure means more ionization so more target materials is being ejected. Also the mean free path of the ejected atoms is decreased due to collisions with the gas particles, which means that there is a trade off where the yield is the highest.

With such a DC plasma usually only conducting targets can be sputtered because a current should be able to flow from cathode to anode. To sputter insulating materials like MgO, a radio frequency (RF, 13.56 MHz) sputtering technique is used, at this high frequency the ions are relatively immobile due to their high mass than the electrons. In such an oscillating potential not only can electrons cause enough ionization of the gas to create and sustain a discharge, RF voltage can also be coupled through any kind of impedance, removing the restriction that the target should be a conductor. A RF plasma can be sustained at lower pressures due to two effects. First, the oscillating electrons at high frequencies cause increased collision with the sputtering gas resulting in enhanced ionization. Second, the secondary electrons are not lost due to the RF plasma and the insulating anode. In a DC discharge, many secondary electrons are lost at the anode, before they can contribute their energy to the ionization process.

If we look at the kinetics of our ejected target atoms we can use a simple molecular dynamics model. If we use a Maxwell-Boltzmann distribution the mean free path of an target atom travelling through the plasma can be described with the following expression:

$$\lambda = \frac{RT}{\sqrt{2}PN\sigma} \tag{2.16}$$

where R is the universal gas constant and N is Avogadro's number. T and P are the temperature and pressure of the background gas, respectively. σ represents the cross section for scattering of the target atom off the background gas atoms, and can be considered constant over the range of typical sputtering pressures used. From this equation we can see that on increasing the pressure the mean free path decreases but simultaneously the amount of target atoms that are ejected is lower. So there is again a trade off between the mean free path and pressure. Another point that can be understood is that, at low pressures, the kinetic energy of the target atoms is higher, due to less collisions and scattering with background gas atoms. This will influence the growth of the film; high energy atoms might have enough energy or add energy to the film by which the roughness generally becomes smaller.

2.3.5 X-ray Photoelectron Spectroscopy (XPS)

X-ray photo-electron spectroscopy or XPS is a measurement technique for quantitative and qualitative chemical analysis of the atoms present in the topmost 10 to 20 Å below the surface of a sample. The principle of XPS is illustrated in figure 2.18. The sample

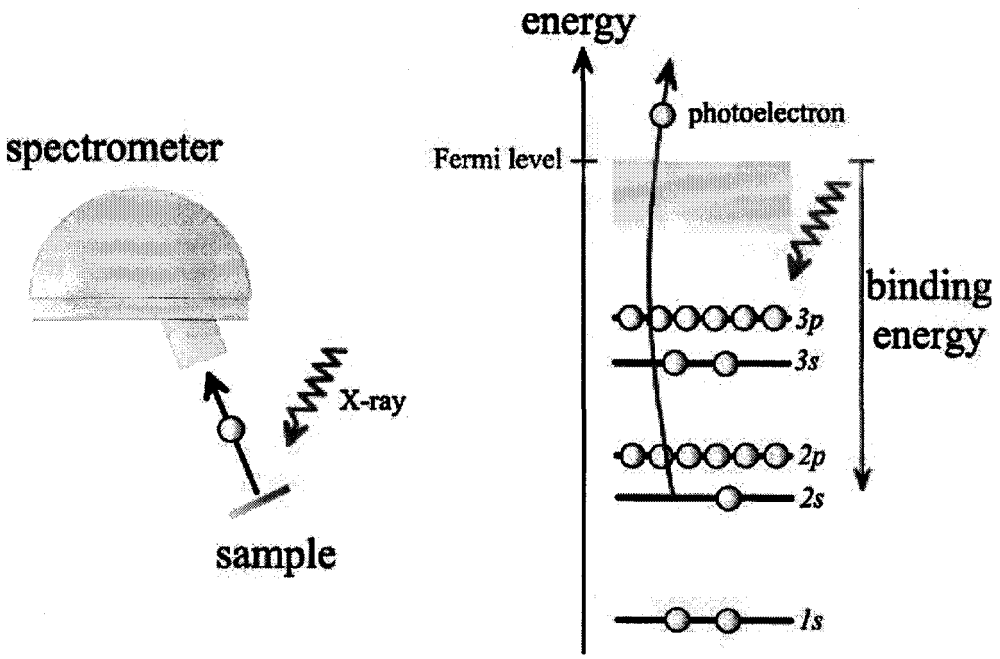

Figure 2.18: X-ray photoelectron spectroscopy, from [25].

under investigation is exposed to monochromatic X-ray radiation of a known, fixed energy. The energy of the X-ray photons is high enough to excite electrons from the atomic energy levels to an energy above the Fermi level. In figure 2.18, this process is shown for an electron from a 2s level. Part of the excited electrons, referred to as photoelectrons, escape from the sample in the direction of a spectrometer which measures the number of photoelectrons as a function of their kinetic energy. As energy is conserved, the kinetic energy of the photoelectrons is equal to the difference between the photon energy and the binding energy of the atomic level. Consequently, the kinetic energy spectrum measured by the spectrometer essentially resembles the spectrum of the atomic levels.

The X-rays penetrate a substantial distance of several μm into the sample. The surface sensitivity of XPS originates from the fact that only the photoelectrons generated in the topmost 10 to 20 Å below the surface are able to escape from the sample. Photoelectrons generated deeper in the sample lose all their kinetic energy before they arrive at the surface through inelastic scattering. Also the photoelectrons that arrive at the spectrometer but are generated several angstroms below the surface, have a probability to scatter and lose a part of their kinetic energy before they escape. These electrons have an arbitrary kinetic energy and therefore give rise to a background intensity in the kinetic energy spectrum.

To introduce more aspects of XPS we consider, as an example, the series of spectra

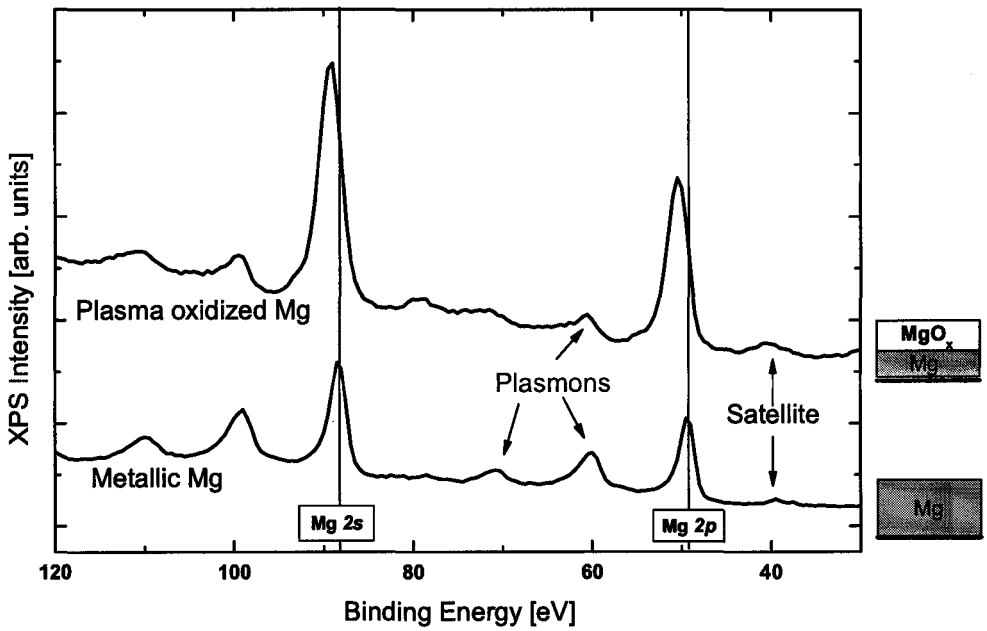

Figure 2.19: Examples of XPS spectra as discussed in the text.

shown in figure 2.19. The spectra are taken from a single sample at different stages. As is common for XPS, the kinetic energy spectrum is shifted in energy by a subtraction of the X-ray photon energy. In this way the spectrum is more conveniently plotted as a function of the binding energy. The spectrum taken first (bottom) is that of a clean 100 Å magnesium film deposited on a silicon substrate. The electronic configuration of magnesium is 1s2 2s2 2p6 3s2. The part of the spectrum shown includes the 2p level at 49 eV and the 2s level at 89 eV. The background intensity is caused by inelastic scattering of the photoelectrons ejected from the valence band.

In addition to the 2p and 2s levels, some secondary structure on the right and the left of the main levels is visible. The X-ray radiation is not completely monochromatic but contains a second small intensity of photons with 10 eV higher energy. These photons are responsible for the small peak on the right of the main levels. Such a peak is referred to as a satellite. The peaks on the left of the main levels are due to photoelectrons who have lost part of their kinetic energy to excite a collective oscillation of the sea of conduction electrons. The energy quantum of such an oscillation is referred to as a plasmon.

When chemical bonds between atoms are formed, the atomic levels are shifted in energy. Although these chemical shifts are relatively small, they can be resolved and therefore provide the extremely useful possibility to study the chemical environment of atoms. An example of a chemical shift is shown in the second spectrum of figure 2.19 (top). This spectrum is taken after the topmost 15 to 20 Å of the magnesium film is oxidized by an exposure to an oxygen plasma. For clarity the spectrum is artificially lifted in intensity so that it does not overlap with the first spectrum. The bonds with the oxygen atoms have increased the binding energy of the magnesium levels with about 2 eV. Also note that,

since there are no conduction electrons in MgO_x, the plasmon peaks are lower in intensity.

Auger Process

Another process that takes place when a solid material is irradiated by X-rays is the Auger process. This is illustrated in figure 2.20. When the electrons from the core levels are exited

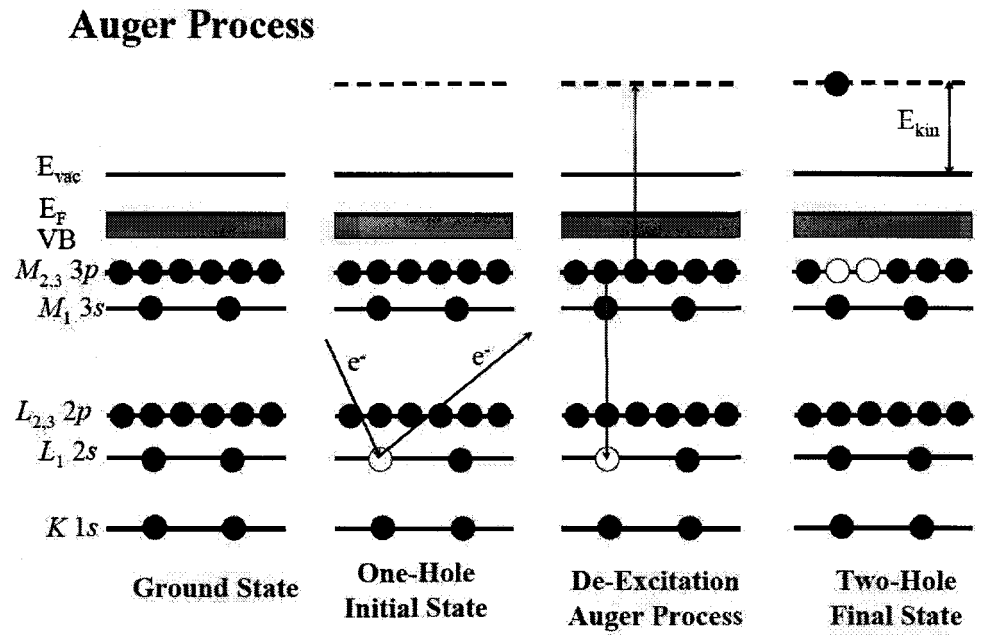

Figure 2.20: The Auger photoelectron process, from [33].

by X-rays in the XPS experiment they leave an empty state behind. This empty state is filled by the relaxation of another electron from a higher core level energy. The excess of energy between the initial and final energy state of this electron excites a second electron. This excited electron is called the Auger electron and its kinetic energy is measured in the same experiment as the aforementioned XPS. The process is described by the initial level the core photoelectron is excited from (in this case L_1 level) and the two levels from which the electron relaxes (M_{23}) and the second excited electron (M_{23}). The Auger electron that is generated in figure 2.20 is thus labelled by $L_1M_{23}M_{23}$. The Auger spectrum is described by the kinetic energy of the measured electrons.

The Auger electrons are more sensitive to the chemical environment of the atoms. The change in kinetic energy between the magnesium and MgO $KL_{23}L_{23}$ Auger electrons is 5 eV. The Mg-$KL_{23}L_{23}$ spectrum is shown in figure 2.21 of a in-situ prepared metallic Mg layer and from a MgO single crystalline (001) oriented MgO substrate. We can clearly see the shift to lower kinetic energy of the MgO substrate. The low intensity seen at the MgO position in the metallic Mg spectrum shows the sensitivity of the Auger lines to the chemical environment of the atoms at the interface. This gives us a very sensitive way to investigate the chemical environment of the interfacial Mg atoms.

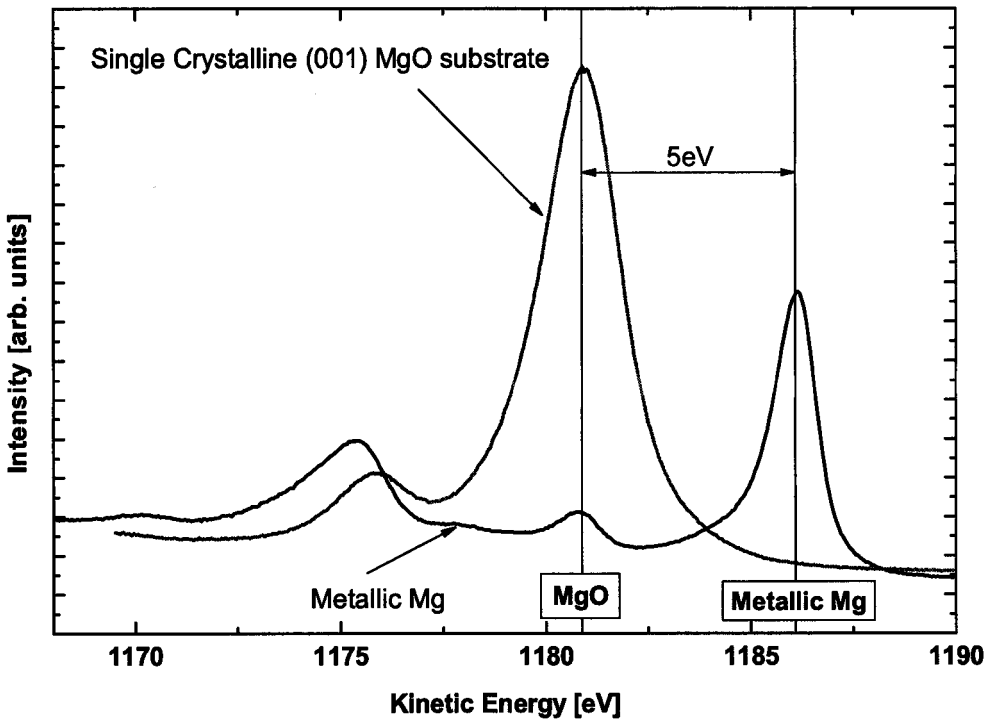

Figure 2.21: The Mg-$KL_{23}L_{23}$ Auger spectrum of a slightly oxidized metallic Mg layer and the Auger spectrum of a MgO (001) single crystalline substrate.

We will discuss the XPS measurements on our MgO layers in section 4.3. An extensive treatment of the XPS technique is given by Briggs [34].

Chapter 3

Critical points for huge TMR-effects

Before we turn to the results obtained during this thesis work, we will summarize the critical points for producing a huge TMR in MgO based MTJ's as found from the theory in section 2.2. From these points we will discuss the research strategy that is followed. Let us start with summarizing the conditions that have to be met for the huge TMR effect with MgO based MTJ's:

- The ferromagnetic electrodes should be in the bcc crystalline structure with (001) orientation; this is required to obtain the correct electronic band structure.
- The barrier-electrode interface should be as smooth as possible to obtain optimal coupling of the discussed Bloch states.
- The MgO barrier should be crystalline in the (001) orientation to obtain the filtering characteristics of the Bloch states.
- The barrier-interface and the barrier itself should be of high purity to eliminate spin scattering or extra hopping conductance by these impurities.

These points should be kept in mind when we fabricate the MgO based MTJ's. But first we give a motivation for the fabrication technique we have used for the MgO barrier.

MgO barrier fabrication techniques

There are different ways of producing an insulating (oxide) barrier with sputter deposition techniques. Sputtering is used because it is a relative easy and cheap (interesting for industry) production method. The most commonly used techniques for fabricating an oxide barrier are:

- Sputtering from a metal target in an oxygen environment, i.e. reactive sputtering.
- Plasma oxidation of a thin metallic layer.
- Directly RF sputtering from an oxide target.

Now let us discuss these techniques with respect to the fabrication of high quality MgO barriers in our sputter maching.

The first technique, i.e. reactively sputtering is one that needs optimization with respect to the oxygen dosis during the sputtering, i.e. getting the right stoichiometry. Also there should be a way of preventing the oxidation of the electrodes. In our sputter machine we have all the sputter targets in one chamber including the electrode metal targets. So after introducing oxygen in the chamber we will have to pre-sputter all targets for a rather long time (typically 15 min). This makes it a very cumbersome method.

Plasma oxidation of a thin metallic layer is commonly used to produce AlO_x barriers. However, this technique is only used in one publication up to date where they show a disappointing TMR of 60% [35]. Also in the past Kant *et al.* [25] measured the TSP of a Fe-MgO junction fabricated with this technique to be no more than 30% [25]. The disappointing results might be originating from the perfect interface that is needed with the crystalline barriers. Very accurately controlling the oxidation of the Mg is necessary in this case.

Direct sputtering from a MgO target however has none of the above mentioned drawbacks, the difficulty in this technique is however the sputtering from an insulating target as was explained in section 2.3.4.

We have chosen for the last technique for our MgO barriers. The most important reason is the amount of papers published by *different* research groups around the world using this technique on high TMR MgO based MTJ's, showing that the process should in principle be easily reproduced. Also, the ease of installing an MgO target in our existing sputter machine made us decide for this fabrication technique.

Ferromagnetic electrodes (CoFeB) and crystallization

In our MTJ's we use ferromagnetic CoFeB electrodes, with a atomic boron content of 20%. This has two reasons; CoFeB grows *amorphous* and the sputter deposited layers are *very smooth*, all due to the addition of the metalloid boron. This solves the problem of getting very smooth electrode interfaces. But now we have to crystallize the CoFeB in the required orientation. This is solved by the MgO at the electrode interfaces in the MTJ's, which is explained below.

The MTJ's are grown with the stack CoFeB/MgO/CoFeB; in the as-deposited case the CoFeB electrodes are amorphous. The MgO in the as-deposited case is partial crystalline. By adding energy to the system, i.e. by heating the stack (annealing), the MgO further crystallizes in the rocksalt (001) oriented crystal structure. This crystalline MgO induces a crystallization in the CoFeB with the correct orientation and bcc crystal structure at the interface. The electronic band structure of CoFeB shows comparable characteristics as the band structure of bcc Fe, Co and CoFe and such calculations are in progress in collaboration with Radboud University. More specifically, we mean that the Δ_1 Bloch states that are present at the Fermi energy in the majority channel but absent in the minority channel (see section 2.2).

Also, in literature MTJ's made by sputter deposition with CoFeB electrodes show the

highest TMR ratios. The crystallization process as discussed above is shown in figure 3.1 taken from Hayakawa *et al.* [36]. In this figure we see high resolution transmission-electron-microscope (HR-TEM) images of three identical sputter-deposited MTJ's in the as-deposited state, and annealed at 270°C and 375°C. On the left in the figure the layer stack is shown. Surprisingly, we already see a well-defined crystalline texture in the MgO in the as-deposited case even when grown on amorphous CoFeB.

This figure proves that with annealing the poly-crystalline structure of the barrier is improved. But more importantly, the electrodes at the interface with MgO crystallize in the bcc structure. It is known that for AlO_x junctions, the CoFeB crystallizes in the fcc structure, which means that in the case of MgO it induces the correct bcc crystal structure. Underneath the HR-TEM images we show the obtained TMR value with these junctions, showing <20% for the as-deposited junctions to 260% TMR after an anneal treatment of 375°C. This proves that the theory as stated in section 2.2, i.e. the required band structure in the minority/majority band of the electrodes and the filtering characteristics of the MgO, should also be valid in the case with these sputter deposited junctions.

The crystallization of the electrodes is also dependent on the seed-layer and the capping layer, i.e. the layer the CoFeB is deposited on (in this case Ru), and the layer on top of the second CoFeB layer (Ta), respectively. These layers also help to induce the correct crystal structure in the electrodes. This means that the very smooth layers these materials form and their crystal structure help the CoFeB crystallize in the required bcc (001) texture.

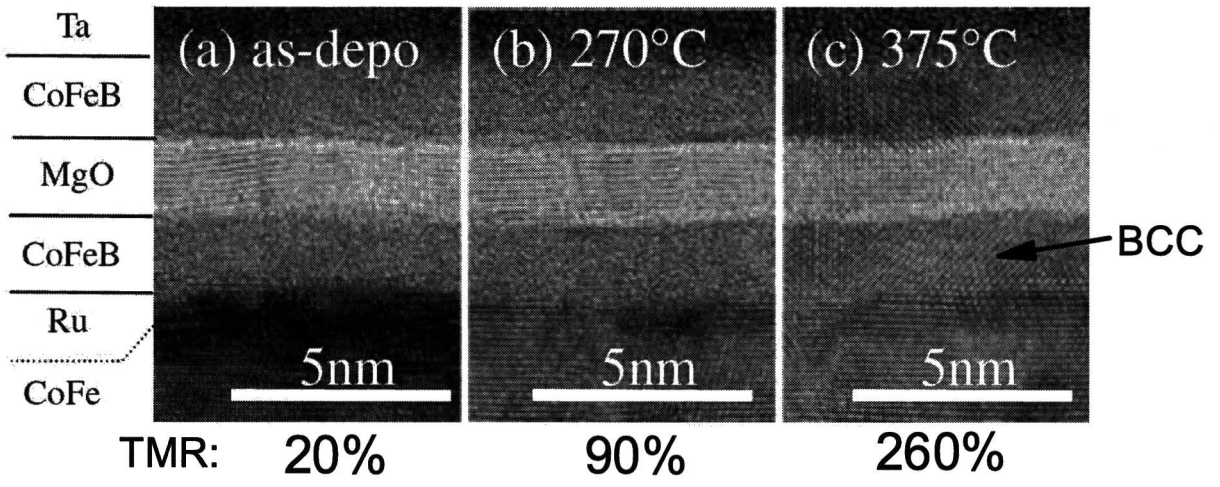

Figure 3.1: Cross-sectional TEM images of CoFeB(30Å)/MgO(20Å)/CoFeB(30Å) interfaces for samples (a) as-deposited, (b) after annealing at 270°C, and (c) after annealing at 375°C. MgO barrier deposited on amorphous CoFeB bottom ferromagnetic layer has rock-salt structure that is highly (001) oriented. Amorphous CoFeB ferromagnetic electrodes are crystallized by post annealing at 375°C. Underneath each figure the obtained TMR value is listed, from [36].

3.1 Research strategy

From the previous sections we have learned that there are many processes that we need to optimize. Here we will discuss 4 research themes that lead to huge TMR effect in our MTJ's:

1. Sputter deposition and crystallization of MgO (section 4.1)
2. Sputter optimization of MgO in MTJ's (section 4.2)
3. Chemical analysis of MgO (section 4.3)
4. (a) Magnetic, (b) electrical characterization and (c) SPT measurement of the MgO based MTJ's (chapter 5)

1 Sputter deposition and crystallization of MgO

Here we focus on the MgO layer itself. This gives us information on the growth and crystallization of only MgO that we can subsequently use to optimize the MTJ's. The addressed issues are:

- Growth of MgO as a function of sputter target-sample distance; this includes the effect on growth rate and roughness using glancing incidence XRD and will be discussed in section 4.1.1.
- MgO deposited on a CoFeB layer using glancing incidence XRD. This simulates the growth of MgO on the actual bottom electrode, in section 4.1.2.
- The crystallization of the MgO layer as a function of the anneal temperature, using high angle XRD in section 4.1.3.

These issues are all related to the structure of the MgO layer. The sample stacks used in this study are typically: substrate//seed/MgO/capping, where in the XRD studies we use thick (>150 Å) MgO layers to obtain a high enough signal to be detected.

2 Sputter Optimization of MgO in MTJ's

This study has been the largest part of this thesis work and shows the optimization of the sputter process of MgO in MTJ's. In this study over 300 batches of MTJ's have been produced leading to 1500 junctions that are individually measured and analyzed. The parameters that are addressed are:

- Power of the RF sputter plasma
- The sputtering pressure
- Biasing the substrate holder

The effect of these parameters on the characteristics of the MgO based MTJ's are analyzed. The large number of samples is due to the difficult growth of MgO in a sputter process. This brings us to the biggest problem encountered during this thesis work. The results obtained in MgO based MTJ's are very hard to reproduce, from the 1500 junctions that have been produced only 4 show a TMR effect larger than 50%, another ~200 show a TMR between 20-50%. The sample to sample variation is also large; this forces us to a statistical analysis of the obtained results.

3 Chemical analysis of the MgO layer

In this study we investigate the chemical composition of our MgO layers with XPS. We compare our sputter deposited MgO with metallic magnesium and two different MgO layers. This gives us the first hints at the reason for the non-optimal results with MgO based magnetic tunnel junctions, as mentioned previously in topic 2.

4(a) Magnetic characterization of the electrodes

Here we discuss the magnetic behavior of our ferromagnetic CoFeB electrodes. In this study we show the results of engineering the magnetic characteristics of the electrodes. The study is done with MOKE, which gives us the ability to locally probe the magnetization on a MTJ.

4(b) Investigating TMR effects

Then we turn to the physics behind the electrical transport measurements in MgO based MTJ's showing high TMR, focussing on:

- Current-Voltage (IV's) characteristics from which we can deduce the barrier height and barrier thickness, see section 5.2.
- Resistance vs applied magnetic field, showing the high TMR obtainable with MgO barriers, see section 5.3.
- Resistance vs temperature from which we can deduce the effect of hopping conductance originating from impurities in our junction, see section 5.3.

From these studies we can pinpoint some of the possible causes of the non-reproducible results. We will also compare our results with those of other studies on MTJ's with AlO_x and MgO barriers. In this study we show the record within our group for a huge 90% TMR effect at room temperature.

4(c) Spin polarized tunneling

To measure the SPT of a MgO based tunnel junction we have performed SPT measurements as explained in section 2.3.1, where we will show one successful measurement of the TSP of a MgO based junction in section 5.4. With this experimental technique we want to investigate the effect of the MgO barrier on the TSP with CoFeB electrodes.

3.2 Sample fabrication

All our samples are made using the sputter deposition tool EUFORAC (Eindhoven University nano-Film depOsition Research and Analysis Center). The technique of sputtering is explained in section 2.3.4. The UHV sputter chamber has the possibility to sputter deposit 6 different materials without breaking vacuum (in-situ); in this way we can produce layered stacks of up to 6 different materials.

To make a tunnel junction with a defined size, we pattern the MTJ using the technique of shadow masking. The used mask can be seen in figure 3.2. We first deposit our bottom layers (below the insulating MgO barrier) through the shadow mask, then remove the shadow mask and deposit on the whole substrate the insulating MgO layer. This ensures a homogeneous insulating layer on the sample thereby creating a homogeneous tunneling current. Next we rotate the shadow mask 90° and deposit the top layers. The important dimension of the mask are the strip widths of 300μm; thus making a junction area of 300*300μm^2. The strips are extended with large end-pads to make electrical connections possible.

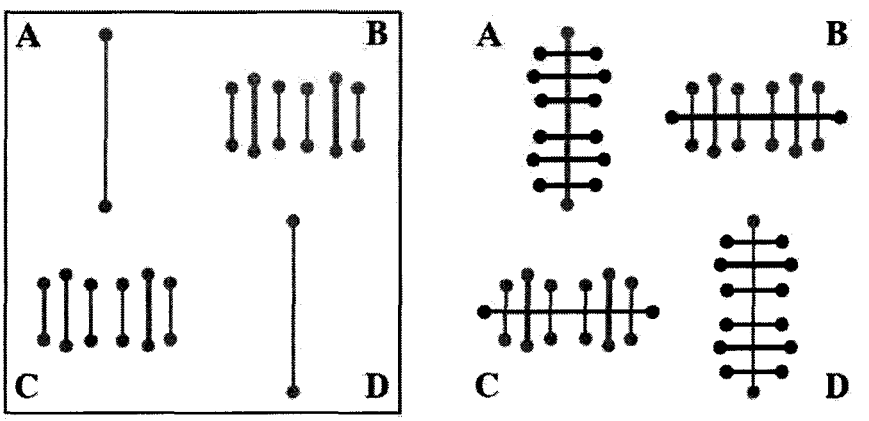

Figure 3.2: The shadow mask used to deposit our tunnel junctions is shown in the left panel in the square. By first depositing the bottom layers and then turning the mask 90 degrees and then deposit the top layers, we get four samples with 6 junctions each. This is shown in the right part of the figure. In A and D we have the long strip as the bottom electrode and in B and C we have the short strips as the bottom electrode; the top or bottom electrode are indicated by the light and dark gray, respectively.

3.2 Sample fabrication

For a overview of the used samples we have tabulated them in table 3.1 where we list the samples by reference to the research theme, corresponding section, the techniques will be discussed in the relevant sections. Due to a known sensitivity of MgO to H_2O we have capped all samples with Al that are analyzed ex-situ, i.e. the samples that are not analyzed in vacuum. The samples used for XPS are not capped, these samples are analyzed in-situ because XPS is a very surface sensitive technique. During the study of the growth of MgO in MTJ's we have kept the stack constant. This was to compare the samples using different sputter parameters.

Study	Technique	Stack	Section
Growth of MgO	Glancing incidence XRD	Al/MgO/Al	4.1.1
Seed layer	Glancing incidence XRD	Ta/CoFeB/MgO/Al	4.1.2
Crystallization	High Angle XRD	Al/MgO/Al	4.1.3
Sputter opt.	Electrical transport	Ta/CoFeB/MgO/CoFeB/Ta	4.2, 5.1 - 5.3
Chemical analysis	XPS	Ta/CoFeB/MgO	4.3
SPT	STS	Mg/Al/MgO/CoFeB/Al	5.4

Table 3.1: Overview of the used samples.

Chapter 4

MgO characterization

In this chapter we present the results obtained by only focusing on the physical properties of a MgO layer. The first two section will focus on the structur of the MgO layer. Then we discuss the sputter optimization of the MgO layer in MTJ's; in this case we will only show the results that are a direct consequence of changes made during the MgO deposition. Finally, we discuss the chemical properties of the MgO layer obtained with XPS and UPS.

4.1 X-ray diffraction

XRD (see section 2.3.3) is used to determine various parameters of the MgO thin films such as layer thickness, crystallographic nature, and it also gives an indication of the roughness. To obtain crystallographic information XRD can only be used on relative thick layers (>100 Å) as compared to the layers used in our MTJ's (~35 Å) due to the intensity of the signal needed. Therefore the studies presented here are only used as an indication for the actual properties of the thin layers used in the MTJ's.

With low angle XRD we can investigate the film thickness and get a measure of the roughness of the MgO. This is done in the first two sections. First we investigate the effect of the target-sample distance during the growth of a MgO film. Next we investigate the effect of the CoFeB seed layer (after an anneal) on the roughness of the film.

Then we turn to the high-angle XRD measurements; this is used to investigate the crystalline structure of our MgO films, and particularly the dependence of the crystalline structure on the anneal temperature.

4.1.1 Target-Sample distance

A parameter directly related to the growth rate and roughness of the films is the distance between the sputter target and the substrate. The distance is related to the physical size of the sputter plasma. When we are close to the plasma we might be sputtering the film, raising its temperature by adding energy to the film or even induce chemical reactions. The gain is an increased growth rate of the film, which may be important when we consider the

amount of impurities introduced in the growing film by the sputter gas. A higher growth rate means a shorter deposition time, so that the film is exposed for a shorter time to the high pressure sputter gas. This is discussed in detail in section 4.3.4. Another gain might be a smoother growth related to the higher kinetic energy of the incoming target atoms and sputter gas ions.

The actual target-sample distance we can set in our system is 65mm to 95mm. In figure 4.1(a) -(d) we see low angle XRD measurements on a stack consisting of CoFeB(50Å)/-MgO/Al(35Å) for three different sputter heights (a) 75mm, (b) 85mm, (c & d) 95mm and different deposition times in (c) and (d). A similar measurement on a Ta film was discussed in section 2.3.3. For a sputter height of 65mm, we weren't able to calibrate the growth rate due to very rough films (no oscillations in XRD measurement). The amount of oscillations per angle 2θ gives a measure of the film thickness and the angle 2θ to where the oscillations are visible is a measure of the roughness.

If we compare 4.1(a) and 4.1(b) both with a deposition time of 4500s, we see that on increasing the target-sample distance the growth rate decreases from ~0.07Å/s to ~0.04Å/s. But the angle where oscillations are still visible increases, which indicates that the roughness increases with decreasing target-sample distance and/or layer thickness. If we then compare 4.1(c) and 4.1(d), which have the same sputter height but different deposition time, we see that the growth rate does not change as expected. However, the oscillations can be seen to a higher angle 2θ for the 3000s case as compared to the 6000s case. This might indicate that the layer gets rougher with increasing layer thickness. If we compare all figures, we see that for the 95mm separation and 3000s deposition case the oscillations exist up the the highest 2θ which indicates lowest roughness for these parameters. This however does not conclude if the layer roughness is related to changes in the layer thickness or sputter height.

To verify this we have grown MTJ's at different target-sample distances, thereby directly investigating the effect of the target-sample distance with the thinner MgO layer in the MTJ's. Remember here that for the XRD measurements we are using thick MgO layers as compared to the MgO layer in MTJ's. The MgO layer thickness in the MTJ's was kept constant, by scaling the deposition time from the growth rate as found from the measurements shown in figure 4.1. We found the optimal sputter height to be between 85-95mm, confirming the suspicion that the roughness increases when we decrease the target-sample distance.

Finally in figure 4.1(e) we show the growth rate as a function of sputter height. We see that for the region of 85-95mm separation the growth rate is nearly constant explaining the similar results found for MTJ's grown in this region.

To conclude this section let us summarize:

- The roughness of the layer increases with both target-sample distance and layer thickness.
- The best results for MTJ's are found in the 85-95mm region of the target-sample distance.

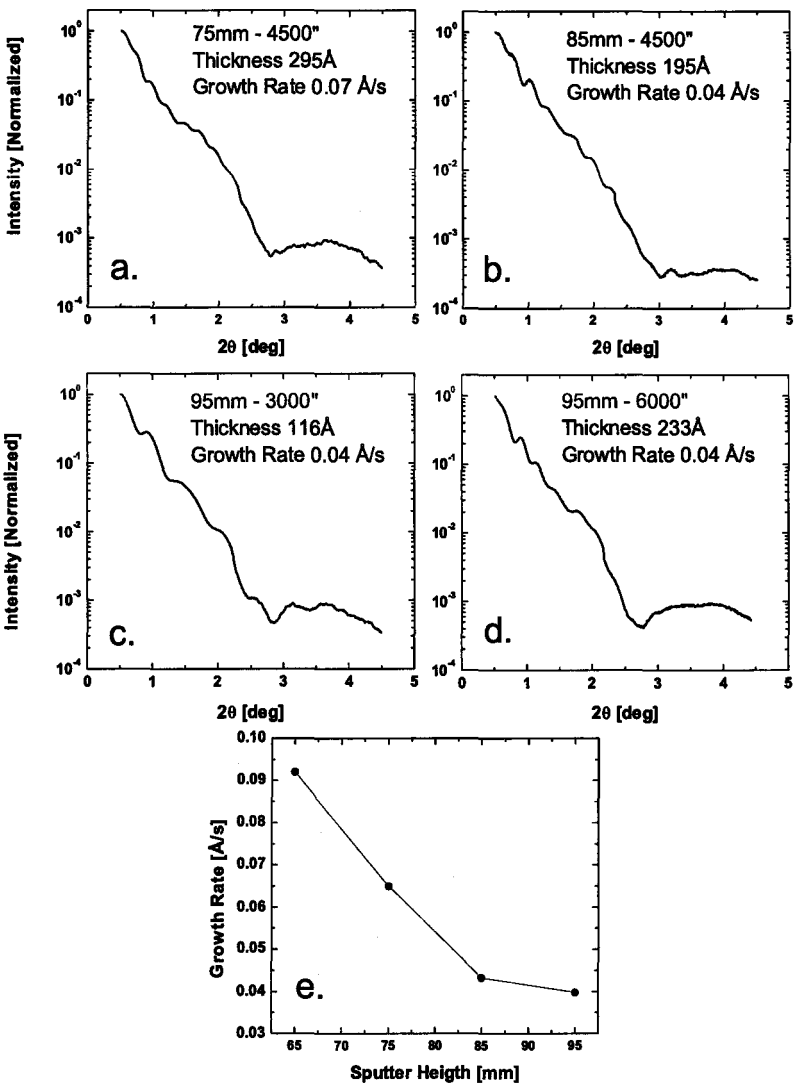

Figure 4.1: (a)-(d). Glancing incidence XRD measurements on stack: Substrate//CoFeB(50Å)/MgO/Al(35Å), for different sputter heights and deposition times. In the top right corner are the MgO layer thickness and growth rate as found from simulations with GIXA. (e). Growth rate as function of sputter height. All samples grown with sputter parameters: 40W RF, $4.5 \cdot 10^{-3}$mbar.

4.1.2 Seed layer

Here, we study the growth of MgO on CoFeB to facilitate fabrication of MTJ's and SPT junctions. The stack used is: Ta(50Å)/CoFeB(50Å)/MgO(240Å)/Al(20Å). In figure 4.2 we see a low angle XRD measurement of a as-deposited MgO film and after an anneal at 375°C. Let us first concentrate on the as-deposited measurement.

We clearly see two oscillations. The long oscillation period originates from the thin Ta and CoFeB layers and the short oscillation period is from thicker MgO, as is indicated in

the figure. Fitting the oscillations with GIXA gives a MgO layer thickness of 240Å. The high angle at which the oscillations die out indicates a smooth growth.

If we compare the as-deposited MgO curve in this figure with the measurements shown in figure 4.1 of the previous section we see that the oscillations are higher in intensity. This is a direct consequence of the MgO layer grown on the smooth CoFeB layer as was discussed in chapter 3.

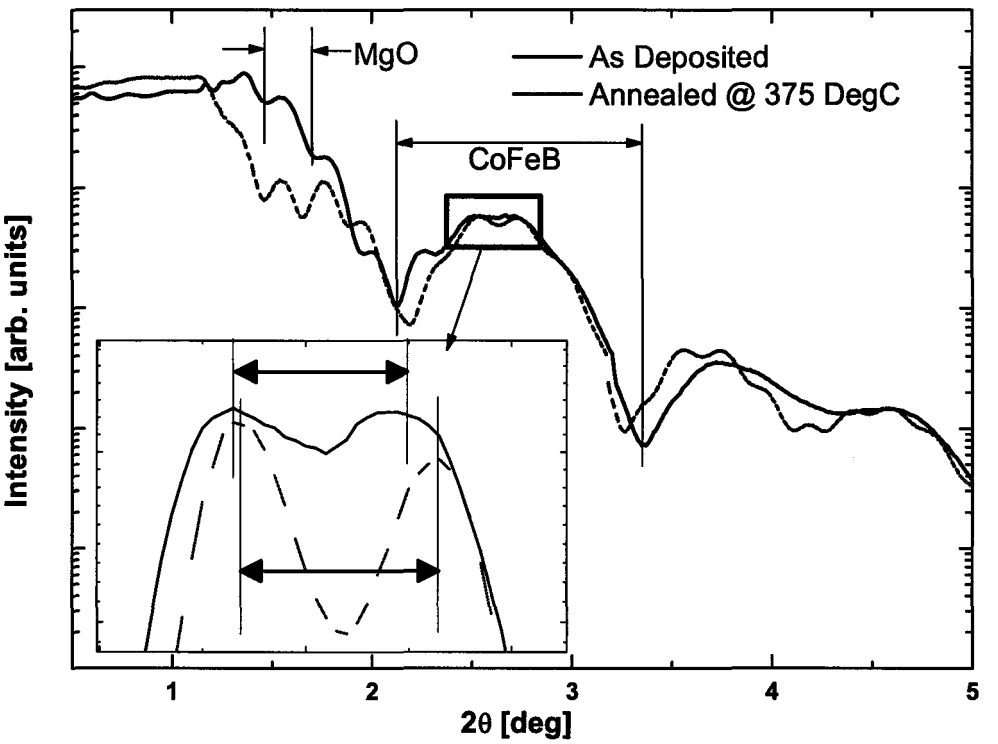

Figure 4.2: Intensity as function of 2θ for an MgO layer deposited on CoFeB in the the as-deposited case and after a 375°C argon anneal. MgO sputter parameters: 40W RF, $4.5 \cdot 10^{-3}$mbar.

After the anneal, the short oscillation period of the MgO is higher in intensity and is visible up to higher angle 2θ which indicates a smoother CoFeB/MgO interface. Also, the oscillation period has decreased slightly, as can be seen in the inset, which indicates a thinner film. The change of the thickness is, however, within the error bar of the simulation with the GIXA software. Nevertheless, we might speculate that this is an indication that the film further crystallizes during the anneal and thereby relaxes the strains in the film as will be seen in the next section. Another cause might be the change of optical contrast between the as-deposited MgO and improved crystalline MgO after the anneal. These are all speculations and further investigation is needed.

4.1.3 Crystallization

With high angle XRD we probe the crystal structure of our layers. We do this to get an indication of the optimal anneal temperature where the MgO crystallizes in the required (002) poly-crystalline orientation. The (002) orientation originates from the used lattice spacing of MgO which is defined as the distance between two Mg or O atoms in the lattice. The diffraction of the X-rays occurs at half this lattice spacing (rocksalt consists of two interpenetrating fcc lattices), i.e. on the lattice planes, leading to the (002) diffraction peak. Again, the measurements are only an indication of the crystallization in our MTJ's because we are looking at relative thick MgO films (460Å). We have done this by growing 6 identical samples in one batch.

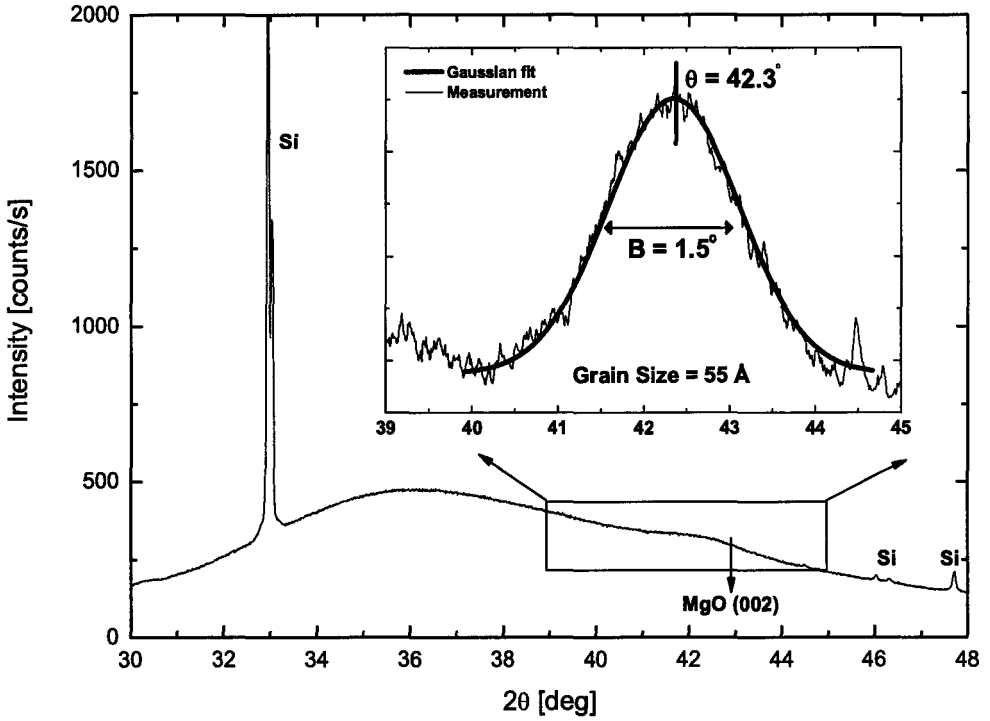

Figure 4.3: High angle XRD measurement as function of 2θ for a MgO layer as-deposited on Al. The inset shows the zoomed in, background subtracted peak for the (002) oriented poly-crystalline MgO, fitted with a gaussian. The stack is: Al(50Å)/MgO(460Å)/Al(35Å), MgO sputter parameters: 40W RF, $4.5 \cdot 10^{-3}$mbar.

In figure 4.3, a scan of a sample consisting of Al(50Å)/MgO(460Å)/Al(35Å) is shown for the as-deposited case. We see a very sharp peak of the silicon substrate at $2\theta = 32.9°$ which consist of two peaks from the Cu X-ray source for the Cu K-α (32.90°) and the K-β (33.02°) lines. Also, the sharp peaks at 46.0° and 47.8° are from the silicon substrate. The very broad peak that extends through the whole figure is due to the amorphous SiO_x layer on top of the crystalline silicon. For a well textured MgO film in the (002) orientation, we

expect a narrow peak at $2\theta = 42.9°$. Instead, we find a broad peak around the angle for the (002) orientation. If we subtract the background by scaling a measurement of a SiO_x substrate, we can isolate this MgO peak, as shown in the inset.

In the inset, the peak is fitted with a gaussian and from this we can deduce two important parameters; the peak position and the full width at half maximum (B). We find the peak located at 42.3° which indicates that the MgO is under strain because we expect the peak at 42.9° for the (002) oriented film. The B is a measure of the grain size, by using the Scherrer formula [32]:

$$t = \frac{K\lambda}{Bcos(\theta)} \tag{4.1}$$

which gives a measure of the crystal grain sizes in the film K(=0.9) is the Scherrer constant, λ is the used wavelength of the X-rays, B is the full width at half maximum and θ the location of the peak [32]. This results in a grain size of 55Å for the as-deposited film.

The effect of annealing on crystal structure for these films at different temperatures can be seen in figure 4.4(a). All the anneals are done in an argon environment, with 30 minutes at high temperature and a rise and fall time of 15°C/min. Two features can be seen in this figure, the shift of the peak position towards $2\theta = 42.9°$, and the narrowing of the peak. This indicates that the strain in the film is relaxing and that the grains of the poly-crystalline film are growing, respectively.

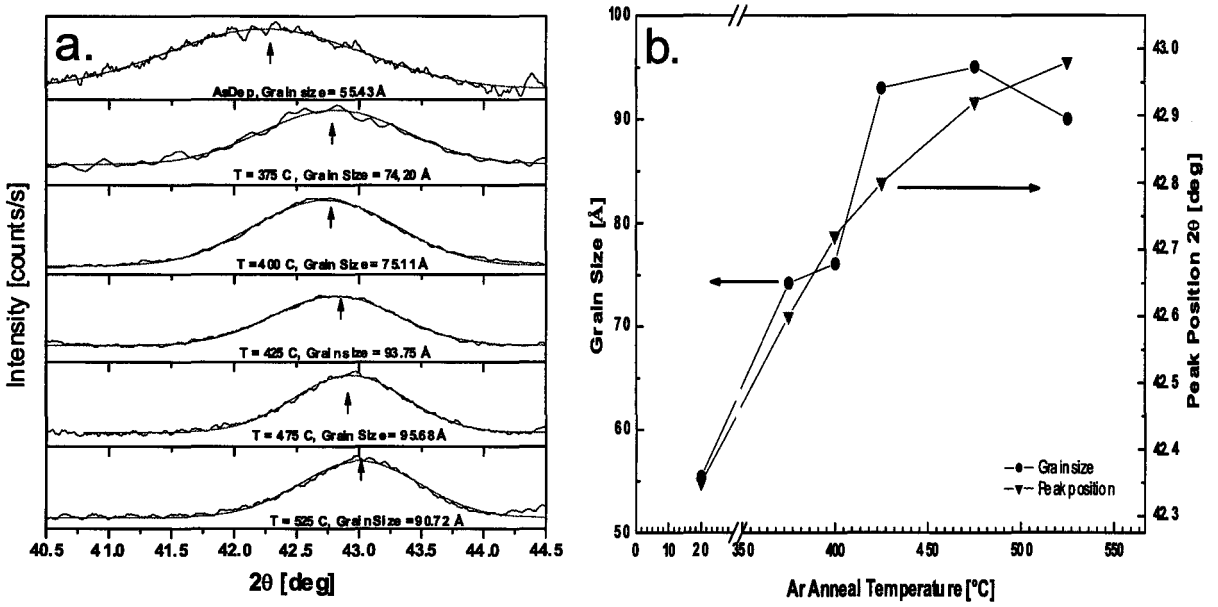

Figure 4.4: (a). High angle XRD measurement as function of 2θ for different anneal temperatures, poly-crystalline (002) oriented MgO film afer background substraction. (b). Grain size and peak position as a function of argon anneal temperature for a 460Å MgO film.

In figure 4.4(b) the two parameters are plotted as a function of anneal temperature. The change of the grain size from 375°C to 400°C is relatively small, but the peak position is shifting to higher 2θ. This indicates that at these temperatures the film is using the thermal energy to relax the strain, or the thermal energy is not enough to overcome the energy needed to merge individual crystal grains. At an anneal temperature of 525°C we see the grain size is decreasing which can have various reasons. One of the most probable cause is the diffusion of Al into the MgO film during the anneal. For this temperature we can also see that the peak position is shifting beyond 42.9° as expected for the (002) orientation. The cause for this is not clear at present.

From figure 4.4(b), we see that the optimal anneal temperature would be 425-475°C. However, from electrical characterization of our thin MgO layer in MTJ's, we find an optimal anneal temperature of 325-375°C from electrical transport measurements (see chapter 5). In the case of MTJ's annealed at higher temperatures there might be diffusion of species and/or oxidation at the barrier-electrode interface. Also, the thick MgO layer might have a different optimal anneal temperature than the thin MgO layer in MTJ's. Another cause of the lower optimal anneal temperature in MTJ's is the growth of the MgO layer on CoFeB electrodes which results in a smoother interface between MgO and the electrodes as was discussed in the previous section 4.1.2.

Now let us compare these results with literature. During this thesis work a lot of publications came out on the crystallization of MgO. The understanding now is that the crystallization of the whole system is determined by the MgO, CoFeB and the seed and capping layers used. At the time of the above study this was not clear.

In figure 4.5 taken from Lee *et al.* [37], the TMR as function of anneal temperature is shown for two different types of MTJ's; a single MTJ (S-MTJ) and a synthetic ferromagnetic MTJ (SF-MTJ). The addition of "single" and "synthetic ferromagnet" originates from the magnetic engineering of the electrodes; this will be discussed in section 5.1. For our current discussion on the crystallization the important difference between the two is the seed layer on top of which the CoFeB is deposited. In the single-MTJ (indicated by the open squares) the CoFeB layer is deposited directly on a CoFe layer. In the SF-MTJ the CoFeB is deposited on a Ru spacer layer (indicated by the closed points). We see that the TMR of the S-MTJ increases with anneal temperature until 325°C and then decreases. For the SF-MTJ's, however, the increase with increasing anneal temperature reaches an optimum TMR at 400-425°C.

The reason for this is seen in cross-sectional HRTEM images shown in figure 4.6. The top two images show the S-MTJ and the bottom two show the SF-MTJ, both after an anneal at 270 °C (left) and 375 °C (right). Lee *et al.* found that in the 270°C anneal case there is no notable difference in the crystalline structure between the two MTJ's. This can also be seen in figure 4.5 where the TMR for both MTJ's is the same. After the anneal at 375 °C, however, Lee *et al.* observe a different crystalline structure between the two MTJ's. In the S-MTJ the top CoFeB has a poly-crystalline structure with uncertain texture, and the bottom CoFeB layer has a poly-crystalline (110) texture (seen in the insert, electron diffraction analysis). In contrast the bottom and top CoFeB layer in the SF-MTJ shows a

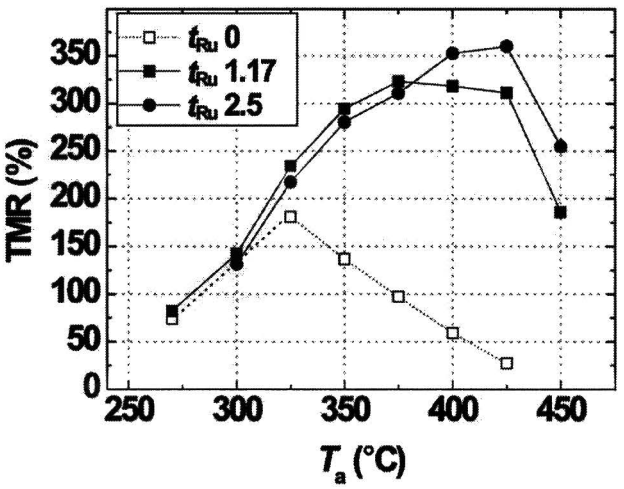

Figure 4.5: TMR ratios as a function of anneal temperature for a S-MTJ and SF-MTJ with 1.17 nm and 2.5 nm Ru thicknesses. For the SF-MTJ spin valve with 2.5 nm Ru, TMR ratio increased up to the very high anneal temperature of 425 °C, while that of the S-MTJ decreased after 325 °C, from [37].

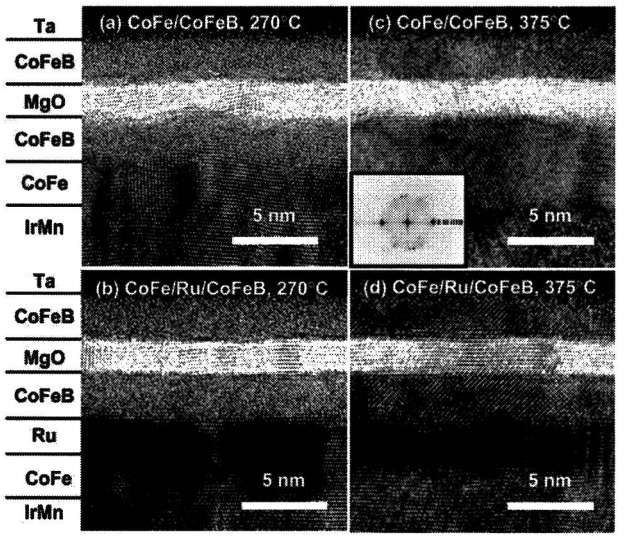

Figure 4.6: Cross sectional TEM images of the S-MTJ and SF-MTJ. S-MTJ after annealing at 270 °C (a) and 375 °C (c). SF-MTJ after annealing at 270 °C (b) and 375 °C (d). All CoFeB layers are amorphous at 270 °C and crystallize differently at 375 °C. The MgO barriers have highly oriented NaCl (001) structures. Inset in (c) is the diffraction pattern of the CoFeB pinned layer for S-MTJ after annealing at 375 °C, from [37].

clear (001) oriented bcc structure.

These results show that the MgO barrier acted as a template for crystallization of both CoFeB top and bottom layers in the SF-MTJ, whereas crystallization of the CoFeB bottom

layer in the S-MTJ was dominated by the seeding of the CoFe layer underneath that was in direct contact with the CoFeB layer. Inserting a Ru spacer between the CoFe and the CoFeB layers prevents seeding from the bottom CoFe layer, causing the amorphous CoFeB top layer to crystallize from the MgO side. It is also important to note that the Ru spacer decreased the surface roughness induced by the underlayers, leading to a formation of a MgO barrier with a clear NaCl (001) texture.

Coming back to figure 4.5 for the SF-MTJ's, the decrease of the TMR for higher anneal temperature (425°C) is due to the enhanced diffusion of the species at these temperatures. These cause degrading of the magnetic switching of the electrodes or even influence the tunnel current. Also, Ru is known to act as a barrier for diffusion showing the higher TMR value for the thicker 2.5 nm Ru layer.

This result shows that the induced crystallization from the MgO layer in to the CoFeB layer can be influenced by the inserted Ru layer. We are currently looking into the effect of the Ru layer on our MTJ's.

If we conclude this section we find:

- From the thick MgO films needed for XRD measurements, we find that we have strained poly-crystalline films in the as-deposited case.
- By annealing at higher temperatures, we find an increased grain size and a shift of the peak towards the expected position of the lattice spacing of (002) crystalline MgO.
- The optimal anneal temperature for the thick films (425-475°C) is higher as found from the electrical characterization of our MTJ's (350-375°C); this is due to the different seed (Al) and thickness of the layer that is used in this study.
- From the discussed result from literature we see that the optimal anneal temperature found from our study on MTJ's (350-375°C) is in close agreement with the results from Lee *et al.* for S-MTJ's (annealed at 325°C). The slight difference can be explained by the Ta seed layer we are using. The decrease in the TMR for the temperature higher than 425°C is probably related to the increased diffusion of species.
- Seed and capping layers are crucial for good texture of CoFeB electrodes to crystallize in the bcc (001) texture.

High Resolution Transmission Electron Microscopy

Before we turn to the optimization process of the MgO layer in MTJ's, we first discuss a HR-TEM measurement that helped us understand the growth problems we have for our junctions.

At the start of the optimization process, we had the opportunity to measure one of our first junctions with a high resolution transmission electron microscope at FEI in Eindhoven. We only had the possibility to measure one junction, for which we have chosen to use an as-deposited exchange biased junction (see section 5.1) from a batch that showed perfect magnetic switching and non-linear IV's after annealing, although TMR was absent.

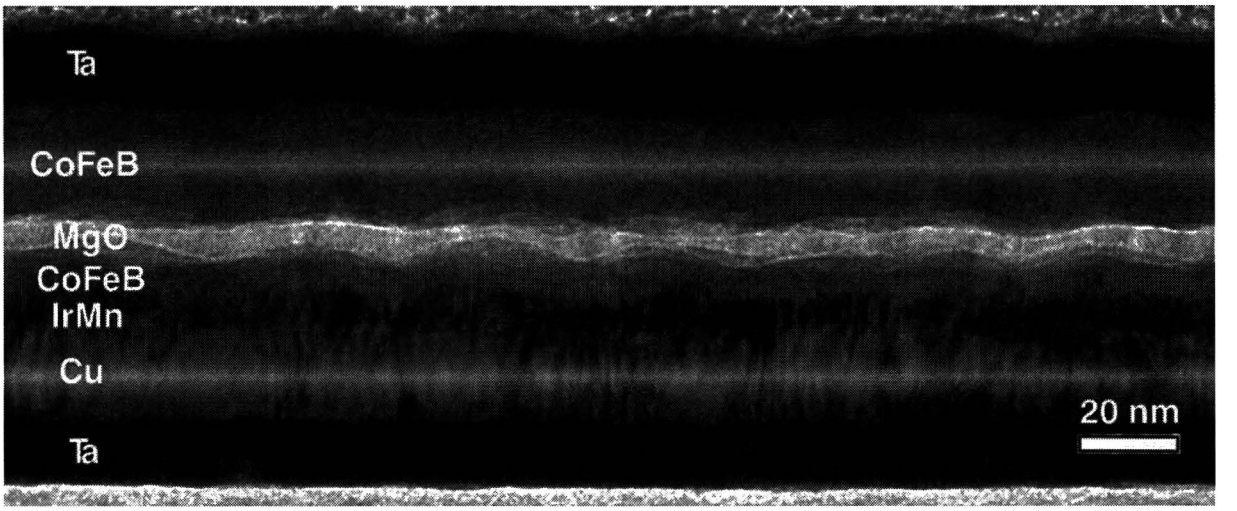

Figure 4.7: HRTEM image of a MTJ stack, from bottom to top we find the stack Ta/Cu/-IrMn/CoFeB/MgO/CoFeB/Ta.

In figure 4.7 we see the HR-TEM image of the stack: Ta/Cu/IrMn/CoFeB/MgO/-CoFeB/Ta. We can see that the roughnesses induced by the substrate propagates and gets worse in the thick Cu layer, which shows small grains indicating poly-crystalline growth. The effect is clearest in the white band that indicates the MgO layer. We do not see any crystalline texture and the layer is very rough, especially when we compare this with the HRTEM found in figure 4.6. This might explain why we find non-linear IV's, i.e. there is tunneling through the barrier but the electrode-barrier interface is so rough that coherent and/or spin-conserved tunneling is not possible in such junctions. Even after annealing we do not expect high TMR values for such junctions due to the rough interfaces. From this figure, we can conclude that the MgO layer was growing amorphous before the optimization process (see section 4.1.2) and that the choice of the seed layers are important to obtain smooth interfaces.

4.2 Sputter Optimization of the MgO layer in MTJ's

The sputter deposition of MgO is not as straightforward due to its insulating properties as compared to the deposition of conducting metals, as was discussed in section 2.3.4. In this section we discuss the optimization of the MgO growth in MTJ's. The electrical transport measurements are very sensitive to the barrier-electrode interface and the crystalline quality of the MgO films. Therefore, most fine tuning of the growth parameters has been done with trail and error on so-called hard/soft MTJ's consisting of the stack CoFeB/MgO/-CoFeB (see section 5.1). A typical measurement result of such a batch, containing a set of 6 junctions, can be seen in figure 4.8. In part (a) we see six resistance (left axis) versus applied magnetic field measurements, one for each junction; on the right axis we plot the corresponding TMR. Part (b) shows the hysteresis loops as measured with MOKE

(see chapter 5) on the electrode strips of this junction, where the different coercive field of the electrodes can be seen. This results in an anti-parallel alignment of the electrode magnetization for 1-4 mT for positive and negative applied fields. We will discuss the details and the further interpretation of these measurements in chapter 5, here we focus on optimization of the sputter growth parameters.

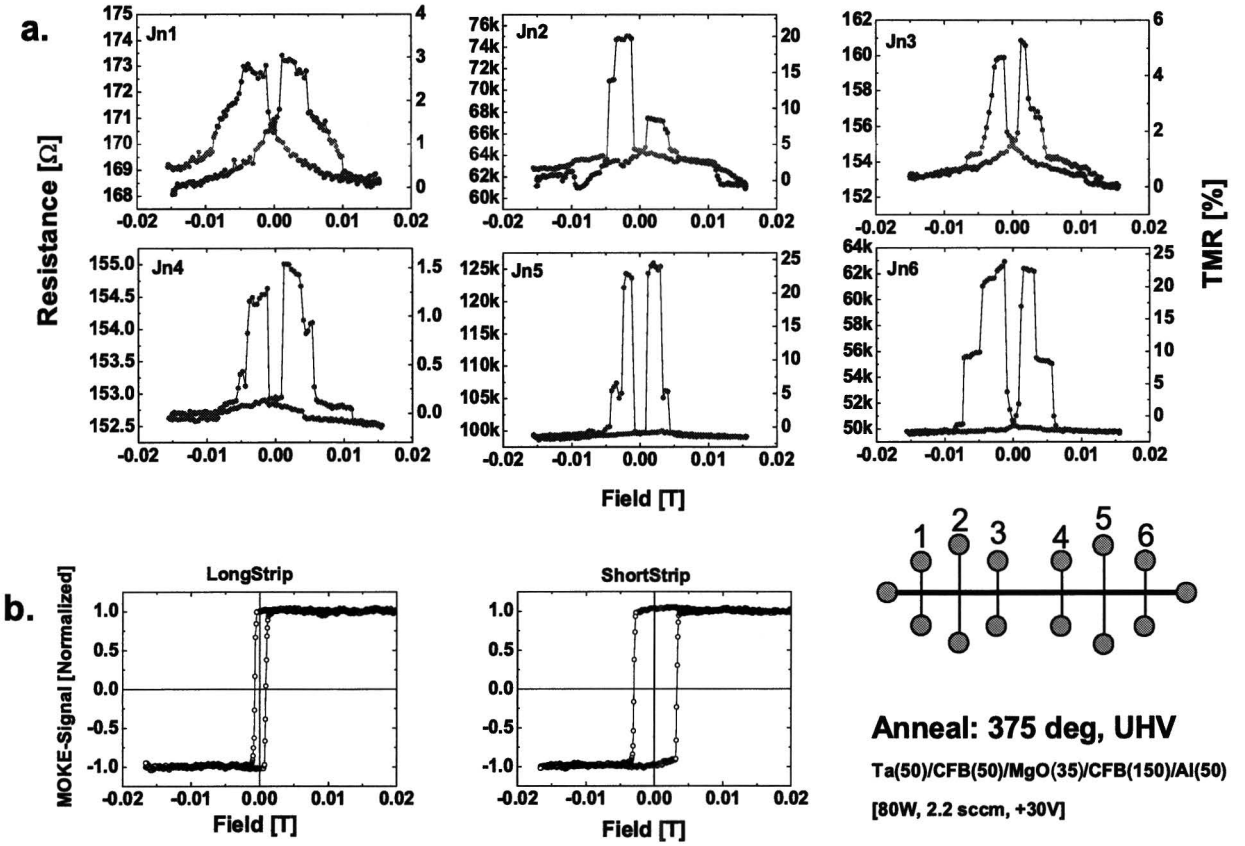

Figure 4.8: A typical example of a measurements on a batch of junctions, part (a) shows the resistance versus field measurements for the 6 junctions as indicated in the lower right corner. Part (b) shows the hysteresis loops as measured with MOKE of the long and short strip. In the lower right corner we show the stack (thicknesses in Å) and growth parameters.

From these measurements we define criteria from which we can compare junctions grown with different MgO deposition parameters. These criteria were yield, i.e. amount of MTJ's showing more then 1% TMR per batch, and the average TMR for the MTJ's showing TMR. In this particular measurement (figure 4.8) we find 100% yield and an average TMR of 10%. As can be seen from the figure, there is a large variation in TMR, resistance and switching behavior even within one batch. In the following, we will discuss general trends as a function of the mentioned criteria between batches grown with different sputter parameters.

MgO RF Plasma power

An important parameter in sputter deposition is the used power. The power was varied between 20 and 120W. At low power (< 20W) the gas pressure needed to keep the deposition plasma stable starts rising significantly. At higher power (> 120W) the power source is not able to couple the power into the plasma.

The result of the measurements done at different power with all other parameters kept constant is seen in figure 4.9. At every measured power (20, 40, 80, 120W) we see the yield and the average of the TMR of 3 identical batches of MTJ's based on 12 measured junctions per batch. We started out with 20W RF sputtering; this resulted in very low TMR (~3%)

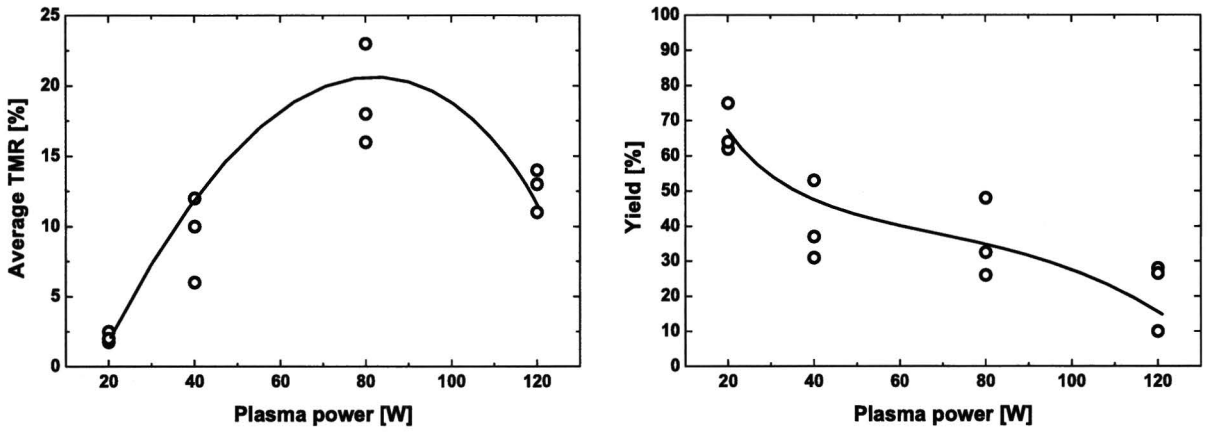

(a) TMR vs Power

(b) Yield vs Power

Figure 4.9: The TMR and yield vs plasma power of identical MTJ's with stack: Ta(50Å)/CoFeB(150Å)/MgO(~35Å)/CoFeB(50Å)/Al(30Å) grown at constant pressure (4.5 mbar), the line is a guide to the eye.

junctions but a high yield (~70%). On increasing the power the TMR increased but the yield decreased. An optimum between TMR and yield was found at 80W, the power used by other research groups (private communication) for sputter depositing MgO is in the range of 70-120W depending on their sputter equipment.

Sputtering pressure

Following the discussion in section 2.3.4, using a low argon sputter gas pressure during the deposition of MgO might result in a smooth MgO layer. This is related to the kinetic energy of the ejected particles and the argon sputter gas ions in the plasma, and it is thought that high energetic atoms carry their energy to the film and thereby a smoother film is obtained [38]. This is also shown by Shen *et al.* [39] in figure 4.10; in this figure they show the obtained TMR (left axis) and the RMS roughness (right axis) as function of

the sputter pressure. The stack used is: Ta(300Å)/CoFe(20Å)/IrMn(150Å)/CoFe(20Å)/-Ru(8Å)/CoFeB(30Å)/MgO(16Å)/CoFeB(30Å)/Ta(100Å)/Ru(50Å). At low pressures the TMR is clearly higher as at the high sputter gas pressure, and is closely related to the roughness, which is lowest at the highest TMR. Also, using a lower sputter gas pressure will lower the partial impurity pressure which will result in less impurities in the barrier, this will be discussed in section 4.3.4.

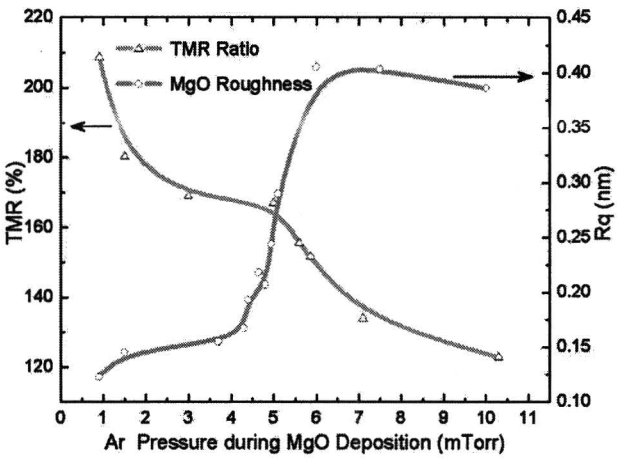

Figure 4.10: TMR ratio (triangles) and as-deposited MgO film roughness (circles) as a function of MgO sputtering pressure. Rq is the RMS roughness of the top surface of the MTJ structure: Ta(300Å)/CoFeB(30Å)/MgO(200Å). TMR ratios are taken from MTJs with 1.8-nm-thick MgO barriers, from [39].

Now let us return to our study. The pressure in the sputter chamber is a function of the sputtering gas flow rate and the pump capacity during sputtering. Because these are constant during sputtering of MgO, we will use the flow rate as the optimization parameter. Unfortunately we are restricted by our sputtering magnetrons to operate above a certain pressure to maintain a constant plasma during sputtering. Our magnetrons are rated to operate at pressures from 5 to 200 mtorr ($6.7 \cdot 10^{-3}$ – $2.8 \cdot 10^{-1}$ mbar). We have varied the pressure from the lowest value where we had a stable sputter plasma; $2.3 \cdot 10^{-3}$ to a pressure of $3 \cdot 10^{-2}$ mbar. In this range the stability of the plasma is largely independent on the applied power.

In figure 4.11, we show the average TMR and yield as a function of the gas flow rate. Again every point consists of an average over 12 measured junctions. We see a large spread but a trend is visible, the lower the sputtering pressure the higher the TMR and yield.

A proof that we are operating at the lowest possible pressures can be found by monitoring the DC bias voltage applied during the sputtering process. We do this by relating the DC bias voltage with a closed shutter to the DC bias voltage with open shutter. The shutter is used to time the exposure of the substrate to the sputter plasma. So with closed shutter the sputter plasma is confined to a smaller volume and with open shutter the plasma is exposed to the larger volume of the sputter chamber. The relation between

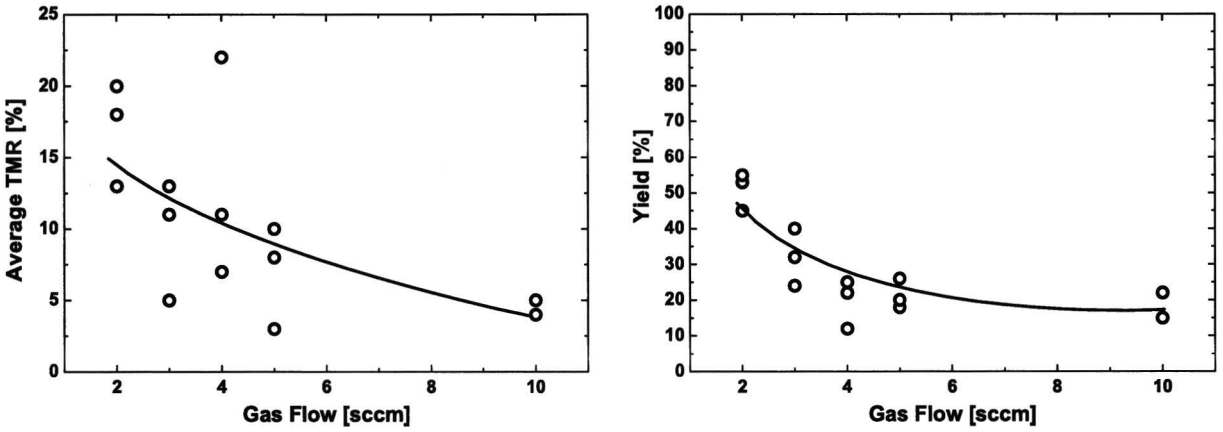

(a) TMR vs Gas flow

(b) Yield vs Gas flow

Figure 4.11: The TMR and yield vs gas flow rate of identical MTJ's with stack: Ta(50Å)-/CoFeB(150Å)/MgO(~35Å)/CoFeB(50Å)/Al(30Å) grown at constant power (80W), the lines are a guide to the eye.

these parameters at the optimal plasma power found (80W) can be seen in figure 4.12. In this figure we plot the applied plasma DC voltage with an open shutter and closed shutter during sputtering as function of the sputtering gas flow rate.

The vertical line in the figure indicates a transition where the DC voltage with open shutter is higher then with shutter closed. In this low pressure region (lower than 2.5 sccm, $3 \cdot 10^{-3}$mbar) we find the optimal results as seen from figure 4.11. This indicates a smoother growth of the MgO. To be able to sputter at lower pressures we have ordered a new magnetron rated to work at pressures as low as 0.5 mtorr ($6 \cdot 10^{-4}$ mbar), an order of magnitude than our current capabilities.

The open shutter DC voltage curve is also dependent on the substrate holder plate. When it is coated with a thick insulating MgO layer from former depositions, the open shutter DC bias voltage curve in figure 4.12 shifts to the left and so a higher gas flow rate is needed to keep the plasma stable. A very thick MgO layer on a substrate holder can be seen in figure 4.13. Therefore, we sand and clean the substrate holder plates thoroughly after each deposition.

To conclude this discussion, we have learned that by varying the sputter pressure the growth of the MgO is influenced as follows:

- Lower sputter pressure shows best results in TMR and yield related to a smoother growth of MgO and less impurities in the barrier MgO.
- Our sputter magnetrons are not rated to work at the low pressures required; therefore a new magnetron rated to work at lower pressures will be used in future work.

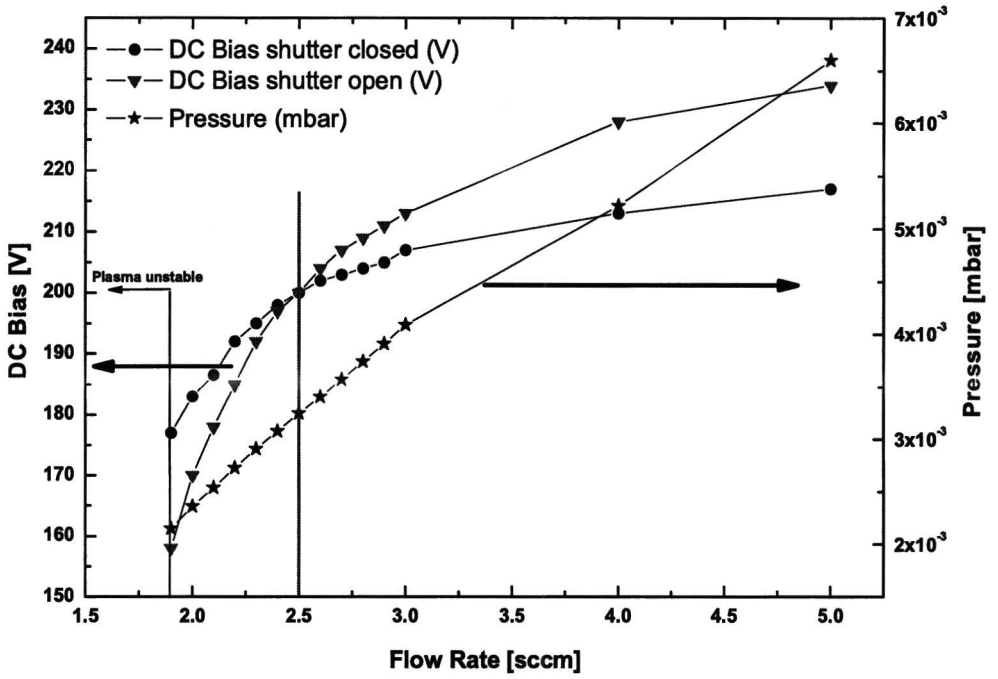

Figure 4.12: The dependence of the DC bias voltage on the sputter pressure for open and closed shutter (left y-axis) during MgO sputtering. The stars show the dependence of the pressure on the flow rate (right y-axis).

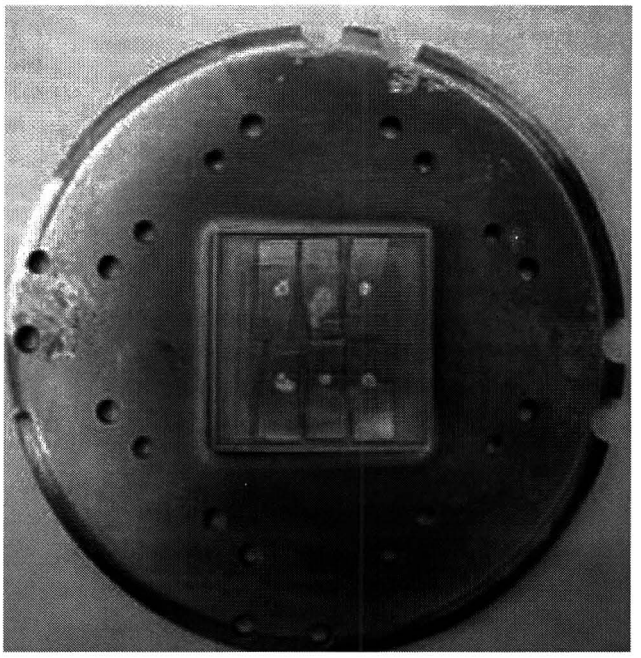

Figure 4.13: The substrate holder plate with a thick layer of MgO.

- An insulation substrate holder plate influences the growth/plasma parameters of the MgO film.

Biasing the substrate holder

Another way of influencing the growth of thin films during sputtering, is by putting a potential on the substrate holder. This will influence the rate and energy at which ions and electrons are incident on the substrate. If we apply a positive bias we will repel the positively charged ions and attract electrons; by applying a negative bias we attract ions and repel electrons from the substrate. In this way, we have a way of influencing the kinetic energy and flux of the incoming ions and electrons on our substrate. The effect of the bias can be seen by eye by observing the plasma.

In our experiment, the bias voltage applied to the substrate holder is varied between -100V and +40V relative to the sputter chamber. At high positive voltage (>40V) the plasma becomes unstable, because at positive bias we are attracting electrons that are responsible for a stable RF plasma. At high negative bias (<-100V) we attract the ions towards the substrate and repel the electrons. This explains that the plasma is stable at higher negative bias compared to the positive bias.

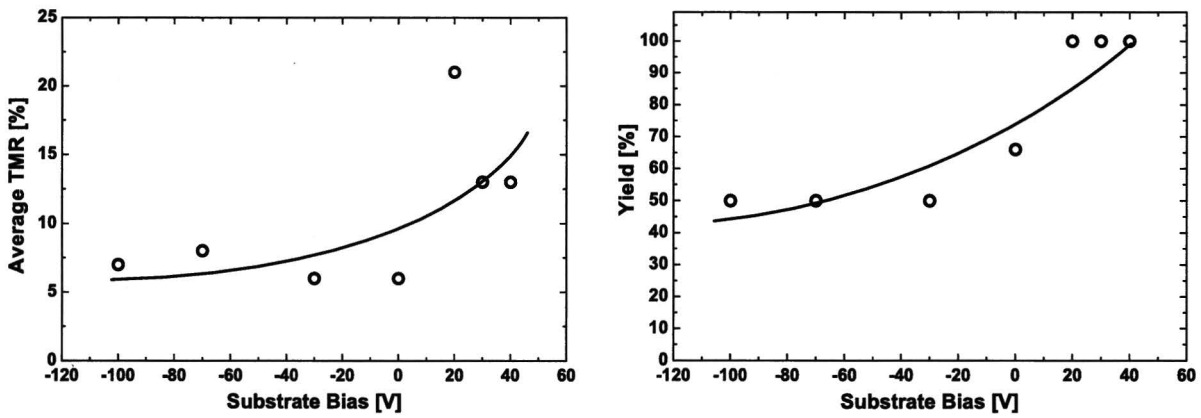

(a) TMR vs applied substrate bias

(b) Yield vs applied substrate bias

Figure 4.14: The TMR and yield vs applied bias on substrate holder of identical MTJ's with stack: Ta(50Å)/CoFeB(150Å)/MgO(~35Å)/CoFeB(50Å)/Al(30Å) grown at constant power (80W) and gas flow rate (2 sccm), the lines are a guide to the eye.

In figure 4.14, we show the TMR and yield as function the applied substrate holder bias. In this case we have measured one batch per applied bias and every point consist of the average of 6 junctions. We clearly see the effect of the optimization process of the sputter power and gas flow rate resulting in higher yield. At positive bias we find for these batches 100% yield and slightly increasing average TMR.

We speculate that this higher yield is caused by the lowering of the kinetic energy of the impinging ions. In literature, it is reported that the ions of the sputter gas (Ar^+) are used to add energy to the deposited film thereby creating a smoother film [38]. Similarly, the same process influence the crystal structure of the film. Note that with this technique we can only influence charged particles; most of the ejected target particles are neutral [38].

Summarizing the above points, we have found the following:

- Attraction or repelling of ions towards the substrate is shown to have influence on our MgO layers.
- A positive bias voltage on the substrate holder leads to a higher yield; the reason might be better crystalline growth and/or smoother layers. The physical process is the lowering of the kinetic energy of the impinging ions.

Concluding this study we see that we have been successful in increasing both the TMR and yield. However, the data shows a rather large scatter, even in samples grown within the same batch. On further investigating the chemical properties of the MgO in the next section, we are able to find some clues on this non-reproducibility.

4.3 X-ray photoelectron spectroscopy

XPS (see section 2.3.5) was used to analyse our sputter deposited MgO layers . We can obtain information on the stoichiometry, chemical environment, and possibly on impurities present in our deposited layers. To analyse our sputtered MgO layers we have also analyzed and compared sputtered metallic Mg, a MgO (001) single crystal substrate and a plasma oxidized Mg layer. By comparing these results, we will be able to show that our sputter deposited MgO films are non-stoichiometric and rich in oxygen.

4.3.1 Metallic Mg and Plasma Oxidized Mg

In figure 4.15, the XPS overview spectrum is shown for a sputter deposited metallic Mg film and the spectrum measured after plasma oxidation step (5 min, $1 \cdot 10^{-2}$ mbar O_2, 7.5W) treatment of this layer. The spectrum is obtained with Al-kα (1486.6 eV) X-rays, as the high energy Mg 1s line at 1305 eV cannot be obtained with Mg-kα (1253.6 eV). We can see the peaks from the core levels of Mg and O which are the 1s for Mg and O, the 2s, 2p lines and Auger lines for Mg. The metallic Mg has been measured to determine the exact position of the individual peaks with our XPS apparatus. On oxidizing the Mg the position of the lines change due to the changed chemical environment as was described in chapter 2.3.5.

For Mg the Auger lines are very sensitive to the chemical environment resulting in a shift of 5eV to lower kinetic energy on oxidizing the Mg. If we zoom in on the Mg $KL_{23}L_{23}$ Auger line in the spectrum, we observe the spectrum shown in figure 4.16. We identify three peaks in this spectrum, the one at highest kinetic energy (1185.7 eV) is due to metallic Mg, the other two at lower kinetic energy (1180.8 and 1175.4 eV) can be ascribed to

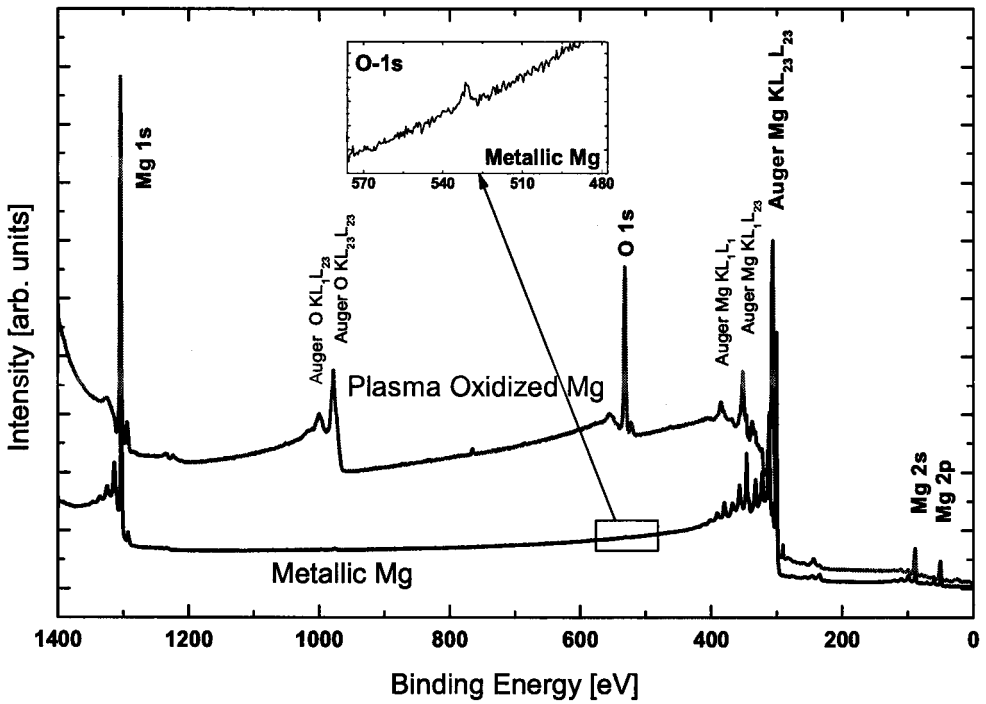

Figure 4.15: XPS overview spectrum of metallic Mg and the plasma oxidized MgO. The inset shows the zoomed in O 1s peak of the metallic Mg.

MgO. The fact that we also see MgO peaks in the metallic Mg shows the surface sensitivity of the Auger lines. Note that we see a very small O 1s feature from the core O 1s line in the metallic Mg spectrum in the inset of figure 4.15. Although we have measured the layer in-situ there is still some slight oxidation of the fresh metallic Mg layer. After plasma oxidizing the Mg we see a shift of intensity towards the MgO peaks. We still see a peak at the metallic Mg position for plasma oxidized Mg. This means that in the first few monolayers that we are analysing with the Auger electrons there is still some metallic Mg left.

We compare our spectrum with a similar study found in literature of a 7 monolayer MgO film epitaxially grown on Ag by Wollschläger *et al.* [40]. This is shown in figure 4.17; we see three spectra in (a) a metallic Mg layer is oxidized at T=200K (thermal oxidation, exposed to 18L of O_2). In (b) we see the same film, but now annealed in UHV to 700K. In (c) we see a MgO spectra of a MgO film grown by evaporating Mg and simultaneously introducing O_2. The spectrum obtained in (a) is similar to our plasma oxidized Mg, showing metallic Mg at 1185 eV and the clear MgO peak at 1180 eV. After the anneal in spectrum (b) the metallic Mg peak has disappeared, indicating that excess oxygen in the surface layers has oxidized Mg in the deeper levels of the film. The spectrum in (c) shows the reactively grown MgO film, this spectrum only shows the MgO peaks with no intensity left at the metallic Mg energy.

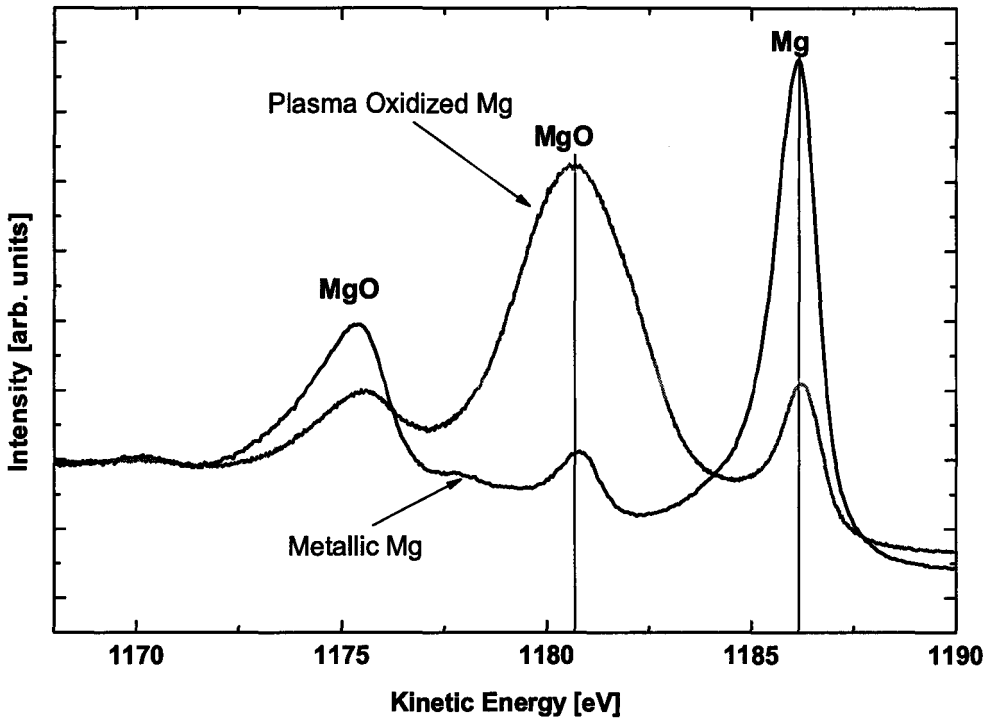

Figure 4.16: XPS Mg-$KL_{23}L_{23}$ Auger line of metallic Mg and plasma oxidized MgO.

The similar spectrum of our plasma oxidized Mg and the thermally oxidized spectrum shown by Wollschläger *et al.* shows that the plasma oxidation is not a optimal way of producing stoichiometric MgO layers. The post-oxidation anneal step would not only oxidize the metallic Mg but might also oxidize the electrodes at the interfaces. The reactively grown MgO, however, shows only MgO. This makes it a good way of producing a stoichiometric MgO layer. But as discussed in chapter 3 introducing oxygen in our sputter chamber and preventing the oxidation of the electrodes makes it a very cumbersome technique.

The 5 eV shift of the $KL_{23}L_{23}$ Auger line from metallic Mg to MgO is commonly expressed in terms of the modified Auger parameter α':

$$\alpha' = E_k(Auger) + E_b(photo - electron) \tag{4.2}$$

where E_k(Auger) and E_b(photo-electron) is the kinetic energy of the Auger line ($h\nu - E_b$) and the binding energy of the photo electron line respectively; for Mg the difference in energy of the $KL_{23}L_{23}$ and the 2p line is used. This parameter is tabulated for different chemical environments [34] of Mg. The advantage of this method is that it is independent of charging effects (relative in one measurement). The tabulated modified Auger parameter for MgO is 1230.8 eV. In our experiment we find 1230.7 eV which indicates MgO. The tabulated modified Auger parameter for metallic Mg is 1235.4 eV, we find 1235.4 eV, so

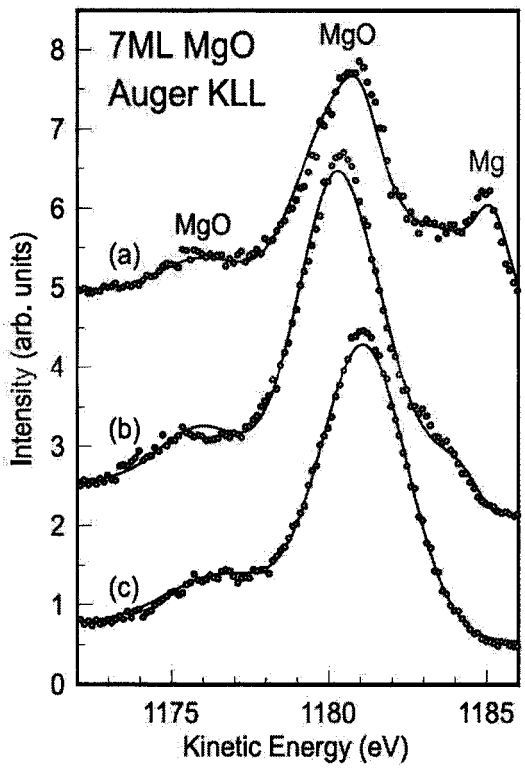

Figure 4.17: XPS Mg-$KL_{23}L_{23}$ Auger spectra for differently prepared 7 ML MgO films. (a). After post-oxidation at T=200 K. (b). After annealing to 700 K. (c). After simultaneous oxidation at T=200 K. The circles show the experimental data. The solid line is obtained from a least-square fit of the Auger peaks with Gaussians. The peak due to metallic Mg at 1185 eV observed for the film post-oxidized film at 200 K vanishes either after annealing to 700 K or oxidizing during growth, from [40].

both are in good agreement with literature.

So we can conclude with the following:

- The effect of the chemical environment of a metallic Mg films can be seen best in the Auger lines and is expressed in the modified Auger parameter.
- Upon plasma oxidation of a metallic Mg layer, we have not completely oxidized the first few monolayers due to the metallic Mg peak we find in the Auger lines.

4.3.2 Single Crystal MgO and Sputter deposited MgO

To determine the stoichiometry and chemical quality of our sputter deposited MgO layer, we have measured the XPS spectrum of a nominally stoichiometric MgO (001) single crystal substrate. It was first thoroughly chemically cleaned and consequently heated under UHV conditions to 700 °C for 30 minutes to get rid of any surface impurities. However, is is generally speculated that the high anneal temperature might induce oxygen

depleted MgO. In figure 4.18, we show the spectrum obtained from the MgO (001) single crystal substrate, plasma oxidized Mg and the spectrum of our as-deposited MgO layer (CoFeB(50Å)/MgO(100Å)). In the figure we included an offset in intensity for a easy comparison.

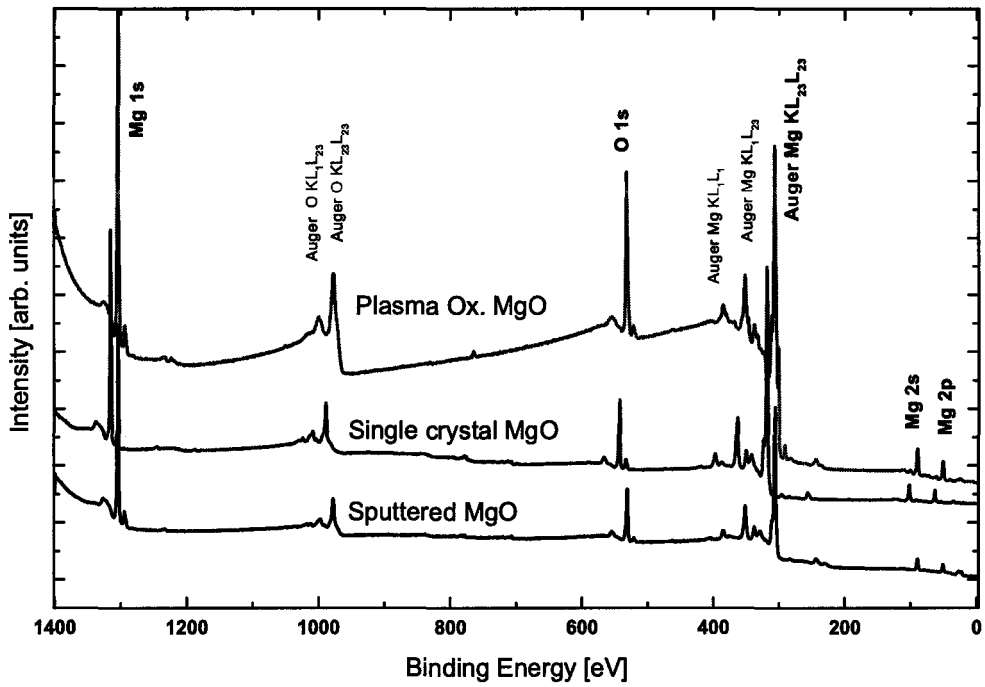

Figure 4.18: XPS overview spectrum of MgO (001) single crystal, plasma oxidized and sputter deposited MgO.

The first apparent feature we see is the large shift in the peak positions for the single crystal. This is due to charging of the sample during the X-ray bombardment which ejects the photo-electrons that cannot be replenished due to the insulating character of the thick MgO. For relative thin films the shift is not so large due to the conducting under-layers. Such the case for our plasma-oxidized Mg and the sputter deposited MgO layer. We can correct the charging by offsetting the spectrum to the correct value found from values in literature. This, however, does not compensate for other side effects of charging like peak broadening originating from a modified escape depth and scattering cross section.

We also closely examined the spectrum obtained on our sputter deposited MgO layer for impurities. We have only found some intensity at the binding energy for argon (Ar 2p, 243eV) and carbon (C 1s, 285eV and Auger, 1221eV). The intensity is, however, too low to pin a quantitative number to these peaks.

If we offset the spectrum to the position of the Mg 2p peak, this results in a shift of 12.9 eV for our single crystal measurement and a shift of 0.4 eV for the sputter deposited and plasma oxidized layer. The modified Auger parameter is independent of this correction. In table 4.1 we have make an overview of all the peak positions as found from our data and as documented in literature (first two rows, the Mg 2s peak in the MgO case was not

tabulated in literature).

- For our metallic Mg film we see that the found values agress within 0.5eV as compared to the tabulated values.
- The single crystal MgO shows a change of the peak position of the 1s when compared to the literature value. This is an indication of the effect of charging in the single crystal which is large as compared to the other two oxides.
- The as-deposited sputtered MgO sample shows very good agreement with the tabulated values for MgO in literature. The slightly lower value of the modified Auger parameter is surprisingly close to the value of the single crystal; this indicates that even in the as-deposited case the Mg chemical environment in sputtered MgO is close to that of single-crystalline MgO.

	Mg 1s	Mg 2s	Mg 2p	O 1s	Auger $KL_{23}L_{23}$	α'
Tab.-Mg	1303.0	90.0	49.4	-	1185.5	1235.4
Tab.-MgO	1304.0	-	50.4	531.0	1180.4	1230.4, 1231.6$^{\#}$
Met.-Mg	1302.8	88.2	49.3	-	1186.1	1235.4
Oxi-Mg*	1304.2	89.1	50.4*	529.7	1180.4	1230.7
Single-MgO*	1303.2	89.1	50.4*	530.5	1180.9	1231.3
Sput.-MgO*	1303.9	89.2	50.4*	530.6	1180.4	1231.2

Table 4.1: Peak position and modified Auger parameter α' as found from tables [34] and found from our measurements. ($^{\#}$ for single crystal MgO, * corrected for charging to the 2p peak (see text)).

If we compare the Auger spectrum of the four different samples as shown in figure 4.19, we see that the peak at the metallic Mg position has completely disappeared for the single crystal and sputter deposited films. This indicates that there is no metallic Mg present in the first few layers of the film. Also, the Auger peaks of the single crystal and sputtered MgO are at the same position after correcting the spectrum to the 2p core position of Mg.

This leads us to the conclusion of this section:

- Due to charging effects of the insulation MgO we find a small shift (~0.4eV) to higher binding energy for thin MgO layers and a large shift (~12.9eV) for the thick single crystal MgO.
- The modified Auger parameter for the single crystalline substrate and the as-deposited MgO show good agreement with values found from literature, indicating that our sputter deposited layers are close to the single crystal chemical environment.

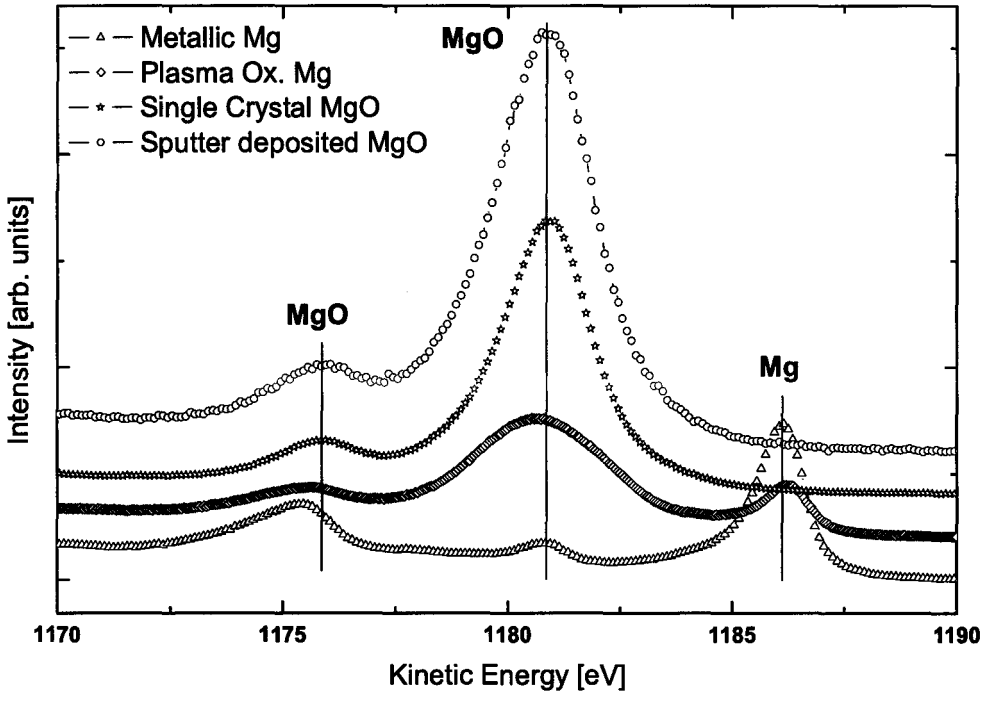

Figure 4.19: XPS Mg-$KL_{23}L_{23}$ Auger spectrum of the four samples, for the oxides a correction to the 2p peak has taken place (see text). The graphs have been displaced in vertical direction for comparison.

- From the Auger lines for the sputter deposited and single crystal substrate we find no remaining metallic Mg.
- From a close examination of the overview spectrum of our sputter deposited MgO we find some impurities in the layer, there is some intensity at the binding energy for argon (Ar 2p, 243eV) and carbon (C 1s, 285eV and Auger, 1221eV). But this is too low for a quantitative analysis.

4.3.3 Stoichiometry

In order to calculate the stoichiometry, we will have to relate the integrated intensities of the Mg peaks to the O-1s peak. In this process we have to compensate for the escape depth of the electrons, and the sensitivity factor of our detector to the individual peaks, both are empirically determined and tabulated in [34].

Another way of determining the stoichiometry is to relate the ratio of the integrated intensity of the Mg peaks to the oxygen peaks in the assumed stoichiometric single crystal MgO [41] to the ratio found in our sputter deposited layer. This maybe not completely accurate as after annealing of the single crystal substrate it is speculated to be oxygen deficient. The result of these calculations is shown in table 4.2 where the ratio [Mg]/[O] atoms is listed.

[Mg]/[O]	Mg 1s	Mg 2s	Mg 2p
Sputtered MgO Calculated	0.80	0.51	0.54
Sputtered MgO/Single Crystal	0.43	0.27	0.76

Table 4.2: Stoichiometry of the sputtered MgO layers determined by correcting for escape depth and sensitivity (calculated), and by relating to the assumed stoichiometric single crystal MgO.

The first observation is a large discrepancy between the stoichiometry determined from the 1s peak to the 2s and 2p peak. A direct reason for this might be the charging effect of the insulating MgO when it is irradiated by the X-rays. The electrons with the higher binding energy might be more sensitive to the charging. This changes the escape depth and the scattering cross section making the discussed methods inconclusive. This is, as expected, even more clear if we relate the integrated intensity peak ratios of the single crystalline substrate to the peaks of the sputter deposited MgO as seen in the second row of table 4.2.

So the only speculation we can make from these results is that we have an oxygen rich MgO layer. Possible reasons for this is that sputtering from a MgO target results in a different sputter rate for the species, or due to the hygroscopic nature of MgO. The exact origin is not clear at the moment.

Further proof of the over-oxidation of the Mg can be found by comparing the O-1s peak in our sputter deposited MgO with the plasma oxidized and single crystal MgO substrate. This is shown in figure 4.20. In this figure we see the O-1s core level lines, where to the right of the figure we see a fit to these curves with two gaussian peak shapes. From the main figure we see that the O-1s peak is made out of two peaks (532.4 eV and 530.5eV). In literature the peak at higher binding energy is shown to belong to MgO_2 [41]. This MgO_2 peak is increasing in intensity if we go from the single crystal to the sputtered film and has maximum intensity in the plasma oxidized case. To make this increase more clear we turn to the fits made to these peaks. When the peak position of both gaussian peaks in all three measurements is fixed. We can then clearly see the increase of the peak at higher binding energy.

Now let us compare these results with literature [41]. In figure 4.21, we see three spectra of MgO layers, all three of them by exposing a Mg layer to O_2 with different exposures. The intensity increases with higher O_2 exposure showing the increasing non-stoichiometric MgO with excess of oxygen. The peak position are comparable with the ones we found for MgO and MgO_2.

Therefore we conclude that for our sputter deposited layer we indeed have more oxygen than magnesium atoms. For the plasma oxidized case the ratio is even worse. Concluding this section we have found the following:

- It is very hard to pin absolute numbers to the stoichiometry; due to charging effects

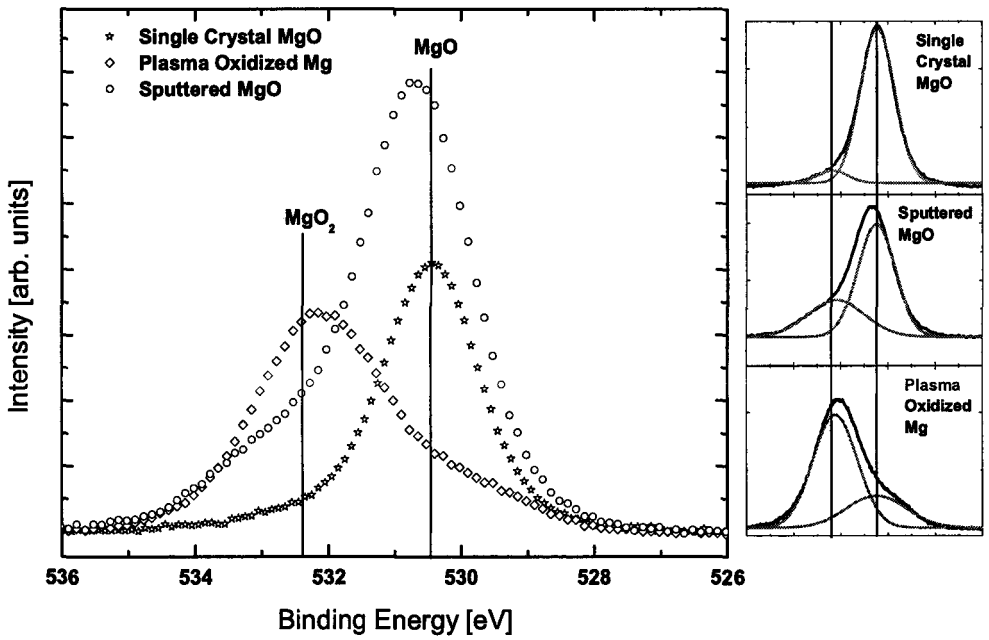

Figure 4.20: XPS charging corrected and background subtracted oxygen 1s core level spectrum for the MgO layers under study, the insets show the fitting with two Gaussians.

the integrated intensity is influenced in such a way that we cannot compensate for this. A solution might be to use very thin MgO films or to use a flood gun, that compensates the charging effect by spraying low energetic electrons on the sample during the measurements.

- We can, however, say that the sputter deposited layers are non-stoichiometric with an excess of oxygen. This is confirmed by the O-1s peak where we see an increase of the intensity to the higher binding energy which in literature is related to MgO_2.

4.3.4 Partial H_2O and impurity pressure

Recently, Itoh *et al.* [42] have shown that 1% chemical disorder in MgO results in reduction of predicted TMR from 1600% to 800%. This demonstrates that chemical and impurity induced disorder in the barrier has a large impact on the spin filter effect, and provides an indication to the hereto experimental failure in achieving the predicted >1500% TMR. We have mentioned before that impurities in the barrier might be a possible underlying cause for low TMR in our MTJ's. One perceivable source of impurities can be associated with the hygroscopic nature of MgO, i.e., its affinity to bond with H_2O. Therefore, during the sputtering process, the partial H_2O pressure in the sputter chamber might be critical and preferably needs to be monitored. We have used various ways to reduce the partial H_2O pressure during sputtering of the tunnel junctions. For instance, pumping with a Ti sublimation pump which is known to effectively lower H_2O partial pressure. Another method adopted was to subject the sample plates to short anneal before introducing them

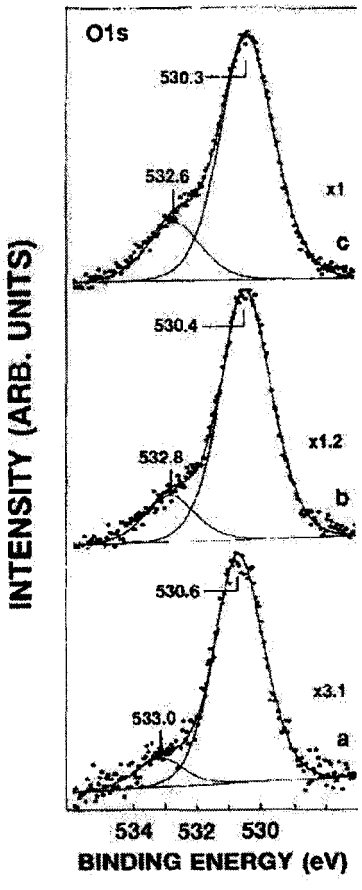

Figure 4.21: O-1s XPS spectra. Seven monolayers of Mg was dosed onto a Mo surface, followed by O_2 exposures of (a) 3L (b) 10L (c) 30L, from [41].

into the sputter chamber. This was intended to lower the local pressure near the sample surface caused by the degassing of the sample plate. The impact of these measures was monitored with a residual gas analyzer (RGA) installed directly in the chamber. Indeed, we were able to reduce the base partial H_2O pressure by an order of magnitude from the 10^{-10} to 10^{-11} mbar range. This in-turn improved the base pressure of the complete sputter chamber from 10^{-8} to 10^{-9} mbar.

Moreover, considering our XPS measurements indicate that we might have MgO_2, instead of MgO barriers, we suspected that partial oxygen pressure in our system could also play a crucial role. In addition to the use of the Ti sublimation pump and annealing the sample holder, we pre-sputtered Ta and Al onto the chamber walls before the crucial deposition of the MTJs. Ta and Al are known to reduce O_2 partial pressure by forming the respective oxides. Using such techniques we were able to reduce the partial pressure of oxygen in the system from $5 \cdot 10^{-10}$ to $8 \cdot 10^{-11}$. However, disappointingly, such measures to reduce H_2O and O_2 partial pressure have not yielded in any improvements in TMR or the yield of our MTJ's to this date.

Having said that, another direct source of impurities is the inert argon sputter gas we use. The purity of the gas directly out of the gas bottle is specified to be 99.9999% (6N) pure. This means that when the sputter pressure is low 10^{-2}mbar, the partial pressure of the impurities is around 10^{-8}mbar. To get a feeling of the number of impurities in the MgO layer due to this impurity partial pressure, we will try to make a rough estimate using elementary vacuum theory. Let us assume an optimistic sticking factor of only 0.1 for the impurities (1 out of 10 incoming impurities stick within MgO). Also, let us assume the number of atoms needed to form one monolayer of impurities is the same as that for one monolayer of MgO. This number of impurity atoms per monolayer can be calculated from the lattice parameter (4.2Å) of crystalline fcc MgO (i.e. 2 times the atoms needed for a lattice of (4.2Å)). Comparing this number to the growth rate of our optimized MgO films (0.07Å/s), we find only ~0.7% of impurities. However, the purity of the gas which enters the sputter system is expected to be lower from that specified for the gas bottles. The primary reason for this is the long argon delivery lines between the sputter system and the gas bottles. Therefore, keeping in mind that the impurity density increases linearly with the partial impurity pressure, and assuming a realistic gas purity level (5N) for the inserted argon gas, we estimate 7% impurities at 10^{-7}mbar partial impurity pressure.

Another source of impurities might be the sputter target we are using, although we have not found high levels of impurities with XPS. The target we are using is a is a hot-pressed target with a density of 75% and purity of 99.95% (excl. Ca), the targets used by other research groups are sintered targets of at least 99.99% (incl Ca.) purity and 95% density (private communication).

However, to make a thorough analysis, all the mentioned issues regarding impurities are currently been addressed. The steps presently being taken are a systematic leak check of the argon lines and installation of a gas filter (9N) in the line. Further, we have recently procured a new sputter gun with enhanced magnetron design. Such a sputter gun should enable sputtering at lower gas pressures, thereby allowing less impurities in the chamber. Moreover, we expect a considerable increase in the growth rate of MgO films, permitting lower deposition times and thus cleaner layers. Also, we have ordered a higher purity (4N) and higher density (95%) MgO target to attempt reduction of impurities from the target itself. We believe that together with the techniques to reduce H_2O and O_2 partial pressures, the new target, sputter gun and argon gas line filter will help us to reach significantly lower impurity levels to produce high quality MgO barriers.

Chapter 5

TMR in MgO based MTJ's and SPT measurements

Here we show the magnetic and the electrical transport characterization of our MTJ's. First we discuss the engineering of the magnetic switching of MTJ's. We then turn to the electrical characterization where we start with the current-voltage relation in our MTJ's. After that we show our best results in the resistance versus magnetic field measurements from which we determine the TMR value of the MTJ's. Next, a study of the resistance versus temperature is given which will discuss some of the electrical transport mechanisms through the barrier. Finally, we show our results on the SPT measurements.

5.1 Magnetic characterization

A condition for MTJ's to show well defined TMR loops is that the ferromagnetic (FM) electrodes show well defined switching of the magnetization. To determine these switching fields (coercivity) we use MOKE (see section 2.3.2). In this section we discuss the magnetic behavior of two types of MTJ's, viz. the so called hard-soft and exchange biased MTJ used for engineering the required magnetic behavior.

5.1.1 Hard-Soft MTJ's

The hard/soft MTJ consists of a FM/I(insulator)/FM stack and makes fast processing of MTJ's possible due to the relatively simple layered structure. However, compared to the exchange biased MTJ's a small range of anti-parallel alignment of the CoFeB magnetic electrodes is obtained.

In figure 5.1, the hysteresis loops for the stack Ta(50Å)/CoFeB(50Å)/MgO(~35Å)/-CoFeB(300Å)/Al(50Å) annealed at 375 °C in a magnetic field are shown. The hysteresis loops are obtained by aiming the (MOKE) laser spot at a specific location as indicated by the arrows in center of figure 5.1. The layers in dark gray in the layer stack and junction drawing (middle of figure) correspond to the bottom layer, the light gray indicated layers

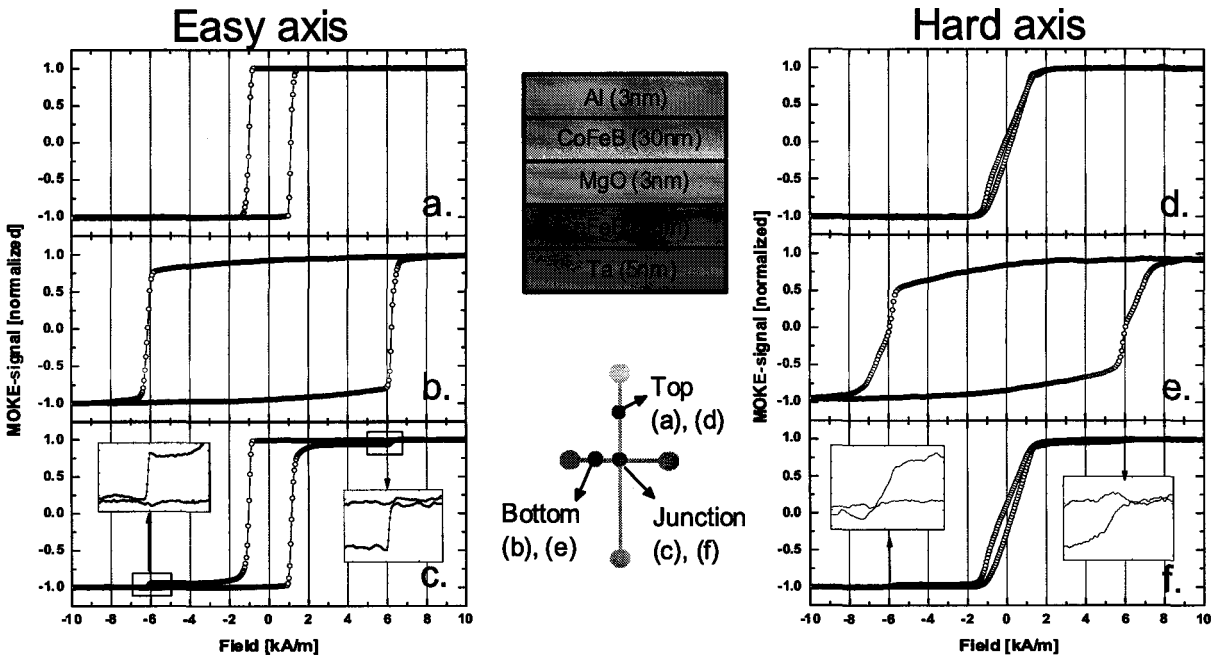

Figure 5.1: Hysteresis loops for a hard-soft MTJ measured after an anneal at 375°C as measured along the easy axis in (a) the soft layer, (b) the hard layer, (c) on the junction; (d), (e), (f) shows the hard, soft and junction layers respectively, measured along the hard axis.

correspond to the top layer. The crossing of the two electrodes in the drawing defines the junction area, i.e. in this area the electrons can tunnel through the MgO to the other electrode.

During the anneal treatment of the MTJ's we apply a magnetic field to induce a large magnetic anisotropy in the films. This anisotropy is used to obtain sharp switching behavior of the electrodes. This can be seen by the sharp switching along the easy axis, i.e. the direction of the applied field during the anneal, (shown in 5.1(a),(b) and (c)) and the rounded loops measured along the hard axis in 5.1(d), 5.1(e) and 5.1(f).

In 5.1(a), (b) and (c), the hysteresis loops of the soft, hard and junction itself are shown, respectively. The difference in coercivity is due to the thickness of the FM layer; a thin layer has a high coercivity (hard layer) and a thick layer has a low coercivity (soft-layer). The hysteresis loop in 5.1(c) shows the magnetization of both layers measured on the junction area, but due to the relative thick top layer the intensity of the bottom layer is low. This explains the small signal seen at 6 kA/m from the hard (bottom) layer. This evidently shows that the two FM layers are oriented anti-parallel in the region 2 - 6 kA/m, for positive as well as negative magnetic fields as can be seen in the insets.

5.1.2 Exchange biased MTJ's

The exchange biased MTJ consist of a more complex layer stack where an anti-ferromagnetic (AFM) layer is used to pin the magnetization of one of the FM electrodes. This leads to magnetically more robust MTJ's in the sense that they have a large range where the electrodes are aligned anti-parallel.

The hysteresis loops can be seen in figure 5.2; here we plot the loops in the same way as in figure 5.1 (note the different scale on the x-axis). For the AFM, we use IrMn to pin the bottom CoFeB layer. The Cu underneath IrMn acts as a seed layer to induce correct growth of the IrMn. The magnitude of the exchange bias field (H_b) is -30 kA/m.

Again we see the effect of the magnetic field during the anneal; when we align the magnetic field along the easy axis we find sharp switching. When we apply the field along the hard axis the switching is gradual.

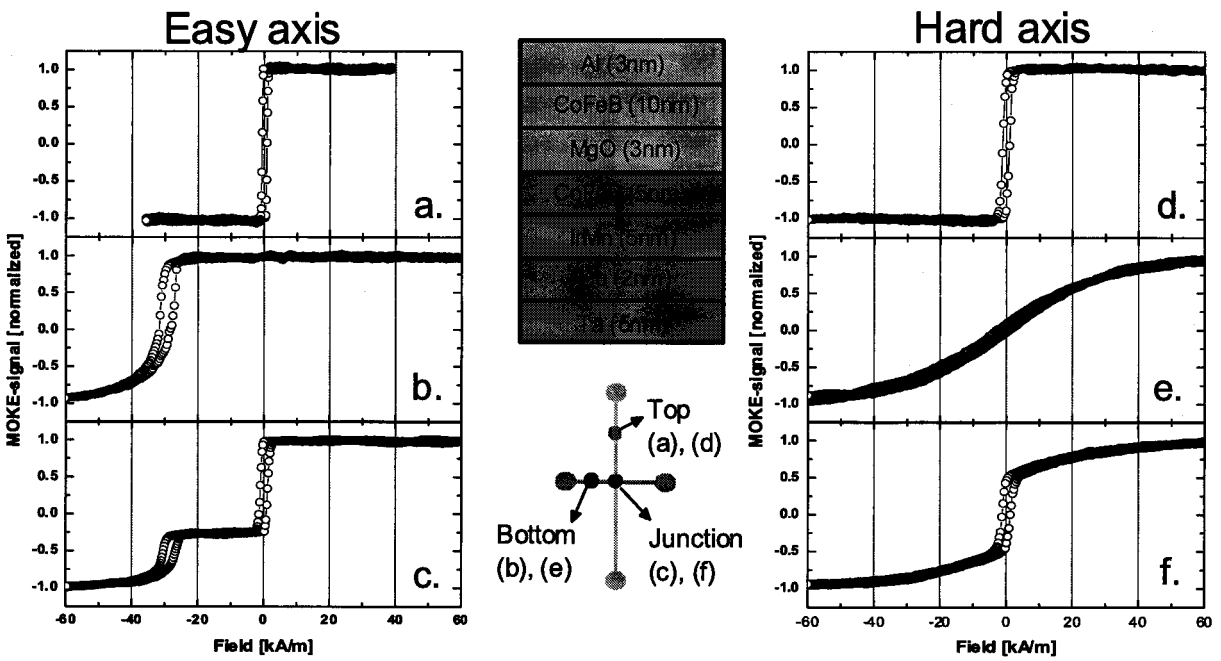

Figure 5.2: Hysteresis loops for an exchange biased MTJ measured after an anneal at 375 °C along the easy axis in (a) the exchange biased layer, (b) free layer, (c) on the junction; (d), (e), (f) shows the exchange biased, free and junction layer, respectively, measured along the hard axis.

5.2 IV characteristics

As discussed in section 2.1.2 one of the characteristics of electron tunneling is the non-lineair behavior of the current as a function of the bias voltage. So the first indication of tunneling behavior in our MTJ's is to look for these characteristics. By fitting these IV's with the

Simmons model, we are able to get a measure of the barrier height and the thickness of our barriers. Please remember that these models assume parabolic free electronic bands so we can only compare the values found here with the values from other research groups and to other batches. The barrier height of MgO found from optical measurements and from electronic band calculations is ~3.8eV [7].

We only measure our junctions from -200mV to +200mV due to the validity of the models in this region [12] and the fact that some of the junctions break down (short out) when we apply larger voltages. In figure 5.3 an IV of a high ohmic tunnel junction is shown, i.e. a thick MgO layer to clearly show the non-linear IV behavior of the tunnel junction in this voltage region. Because this is a symmetric junction (same electrodes) we use fitting to the Simmons model, and the fitting parameters are the barrier height and the barrier thickness. For this particular junctions we find a barrier thickness of 4.8nm and a barrier height of 0.85eV and this junction shows a TMR of 10%.

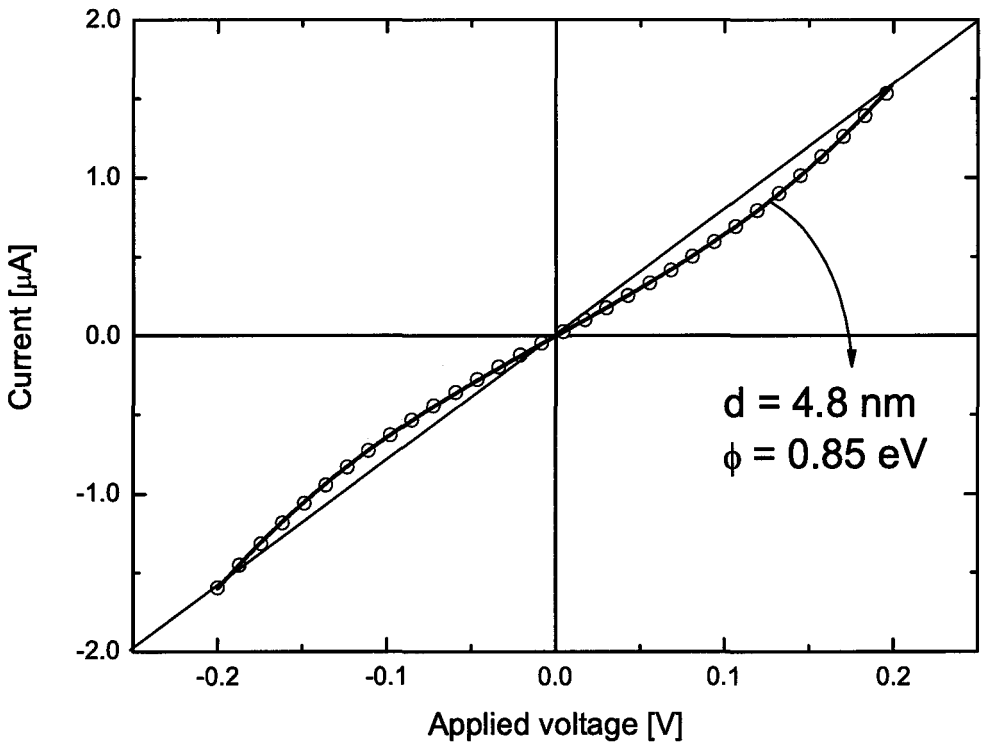

Figure 5.3: A room temperature IV of a MTJ stack consisting of: Ta(50Å)/CoFeB(150Å)-/MgO(45Å)/CoFeB(50Å)/Al(30Å), annealed at 375°C, together with a fit to the Simmons model.

For our junctions showing a TMR higher than 20%, we however find a large spread in the barrier height of 1.4 - 1.9eV which is in the same range as values found in literature by Parkin *et al.* [6] who finds 1.1 - 1.7eV. Our best junctions with the highest TMR ratio (90% at room temperature, see next section), shows a higher barrier height of 1.9eV. This is a general trend, and can be seen in figure 5.4. In this figure, we plot the TMR of our

best junctions as a function of the barrier height. The higher the TMR ratio the higher the barrier height. Further investigation is needed because we only have 3 MTJ's showing a TMR higher as 50%.

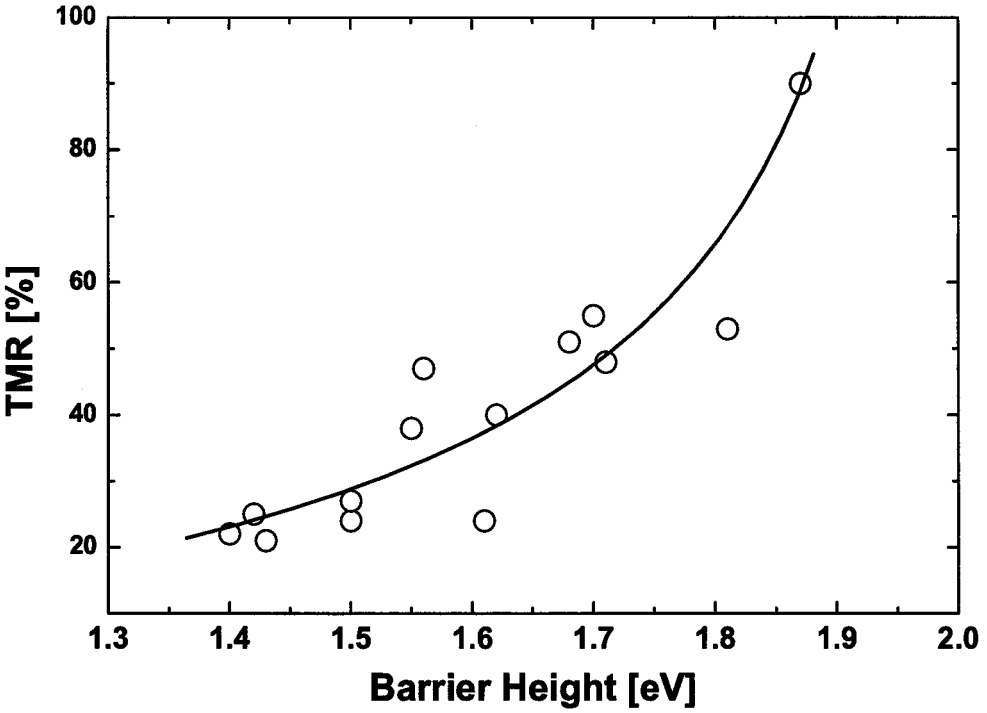

Figure 5.4: TMR versus barrier height ϕ at room temperature for MTJ's with the stack: Ta(50Å)/CoFeB(150Å)/MgO(~35Å)/CoFeB(50Å)/Al(30Å), annealed at 375°C. The line is a guide to the eye.

Recently, this reduction of the barrier height compared to optical experiments is substantiated by a theoretical interpretation by Mathon *et al.* [23]. They state that a intermixing at the barrier electrode interface lowers the Fermi level from halfway in the band gap (3.8 eV) to ~2eV. The low barrier height we find might might thus also indicate that we have significant more intermixing at the barrier-electrode interface leading to the relatively low TMR (10%).

However, most of our junctions show non-linear IV's and a high barrier height but no TMR. This indicates that we have an insulating barrier but the spin-information is completely lost on tunneling through the barrier. The cause is expected to be due to oxidation of the electrode-interface region, intermixing, or spin scattering at the interface or on (magnetic) impurities in the barrier. In conclusion we have found:

- Almost all of our junctions show non-linear IV behavior, but only few show TMR. There is a relation with the found barrier height; junctions showing high TMR have typically a barrier height around 1.7 - 1.9eV where the barrier height saturates at 1.9eV.

- Recently a theoretical interpretation [23], reported for the apparent lower barrier height. They show that due to the intermixing of the atoms in the barrier-electrode region, the barrier height is lowered to values around 2eV.

5.3 TMR behavior

Here, we show the behavior of the TMR as function of field and temperature. From the temperature dependence we are able to speculate on the amount of impurities in our barriers that lead to hopping conductance channels in our junctions.

Resistance vs Field

In figure 5.5, we see a measurement of a junction that showed the highest TMR value. In this figure, the resistance (left axis) and TMR (right axis) versus applied magnetic field is shown for our best junction at room temperature. This junction shows a huge TMR effect of 90% at room temperature which is a record within our group and clearly shows the filtering effect of the crystalline MgO barrier in comparison with AlO_x. The different stable anti-parallel alignments, the so-called shoulders indicated by the arrows are probably caused by different coercive fields of grains/regions at the magnetic electrodes close to the barrier interface.

Figure 5.6 shows the impact on cooling the junction, we see the resistance as a function of externally applied magnetic field for three different temperatures. Firstly note that the TMR increases to 150% at 4.2K. The resistance in the anti-parallel alignment shows a relatively larger increase than the resistance in the parallel alignment. This is the cause for the higher TMR effect.

The origin of the increase of TMR with decreasing temperature can be found in various possible contributions to the total conductance, such as direct tunneling, magnon and phonon assisted tunneling, hopping conductance via localized states in the barrier. Each of the processes have their own specific temperature dependence.

The TMR ratio between the measurement at 4.2K and 300K is 1.7. This is comparable (1.5 - 2.0) to what is found by other research groups [37], [6]. For epitaxially grown barriers the ratio is shown to be lower (1.2 - 1.5) in Fe-MgO-Fe and Co-MgO-Co as compared to sputter deposited junctions. This is directly related to the extra conduction channels that are temperature dependent in sputter deposited junctions and the non-sharp interface. The world-record TMR for sputter deposited MTJ's with MgO barrier and CoFeB electrodes was presented at the conference ICM 2006. Here Hayakawa *et al.* demonstrate a TMR ratio of 405% at room temperature and 800% at 4K, showing a ratio of 2. As is commonly known, we also see in figure 5.6 that the coercivity of the magnetic layers increase with decreasing temperature, and results in a larger region of anti-parallel alignment.

In figure 5.7, we show the TMR (right axis) and resistance area product (left axis; resistance times the area of the junction) as function of temperature. Figure 5.7(a) represents measurements on sputter deposited junction grown by parkin *et al.* [6] and figure

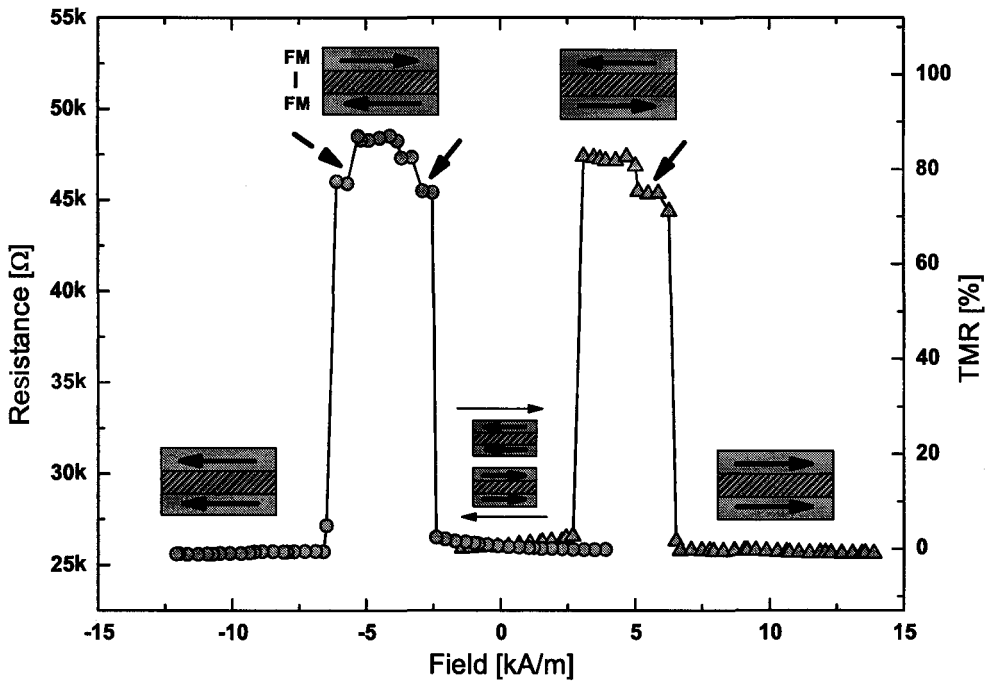

Figure 5.5: The resistance (left axis) and TMR (right axis) versus applied magnetic field, the insets show the orientation of the ferromagnetic (FM) layers separated by the insulator (I). The stack consist of Ta(50Å)/CoFeB(50Å)/MgO(~35Å) /CoFeB(150Å)/Ta(50Å), annealed at 375°C. The solid circles (triangles) indicate a field sweep from positive (negative) field to negative (positive) field.

5.7(b) represents our junction. The resistance area product is used to compare junctions grown in different laboratories. Our junction area is 300*300μm^2 where as that of Parkin *et al.* is 80*80μm^2. The higher RA product of our junctions is due to a relatively thicker MgO layer. On comparing the two graphs we see that for our junction the temperature dependence is higher, this is shown for the parallel case (RA$_P$). In the data from Parkin *et al.* we find for RA$_P$ between low (RA$_{P,LT}$) and high temperature (RA$_{P,HT}$) a ratio of 17% where for our junction we find 28%. We will look into this temperature dependence more closely in the next section.

To conclude this section we have shown that we are able to produce high TMR junctions. In this particular case the behavior is in agreements with what is found in literature. To get an indication why this high TMR effect is not reproducible in all our junctions we will in the next section look into the temperature dependent behavior of the resistance of the junction.

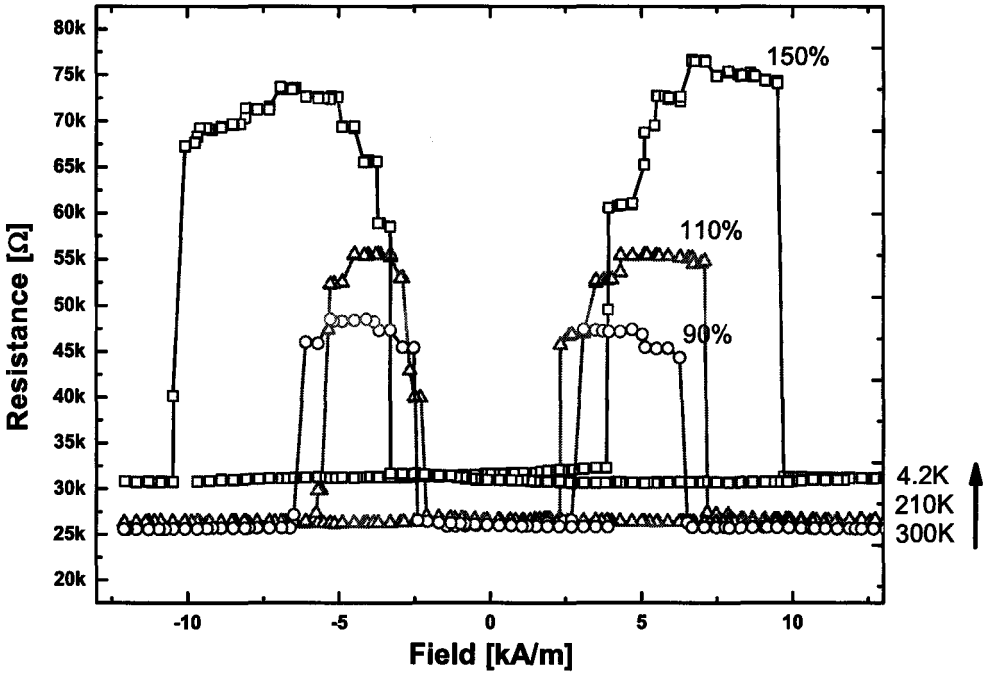

Figure 5.6: The resistance versus applied magnetic field for different temperatures.

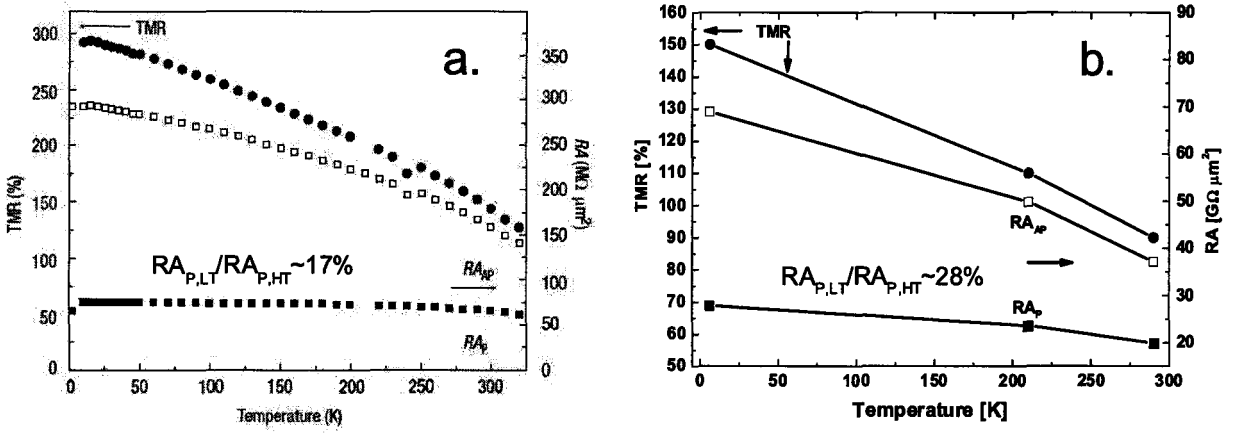

Figure 5.7: The TMR and resistance area product (RA) as a function of temperature. (a) as found by Parkin *et al.* [6] with the stack TaN(100Å)/IrMn(250Å)-/$Co_{84}Fe_{16}$(8Å)/$Co_{70}Fe_{30}$(30Å)/MgO(30Å)/$Co_{84}Fe_{16}$(150Å)/TaN(150Å). (b) For our best junctions with stack: Ta(50Å)/CoFeB(50Å)/MgO(~35Å)/CoFeB(150Å)/Al(30Å) grown at optimal power (80W), gas flow rate (2 sccm), and substrate holder bias (+30V).

Resistance vs Temperature

To elaborate on the various temperature dependent conduction mechanisms, we show in figure 5.8 the normalized parallel conductance as a function of temperature for a junction showing 91% TMR at 4.2K and 53% at room temperature (again ratio of 1.7). This junction shows a slightly higher (34%) temperature dependence as compared to the 28% and 17% in our best junction and that of Parkin *et al.*, respectively. We have fitted the

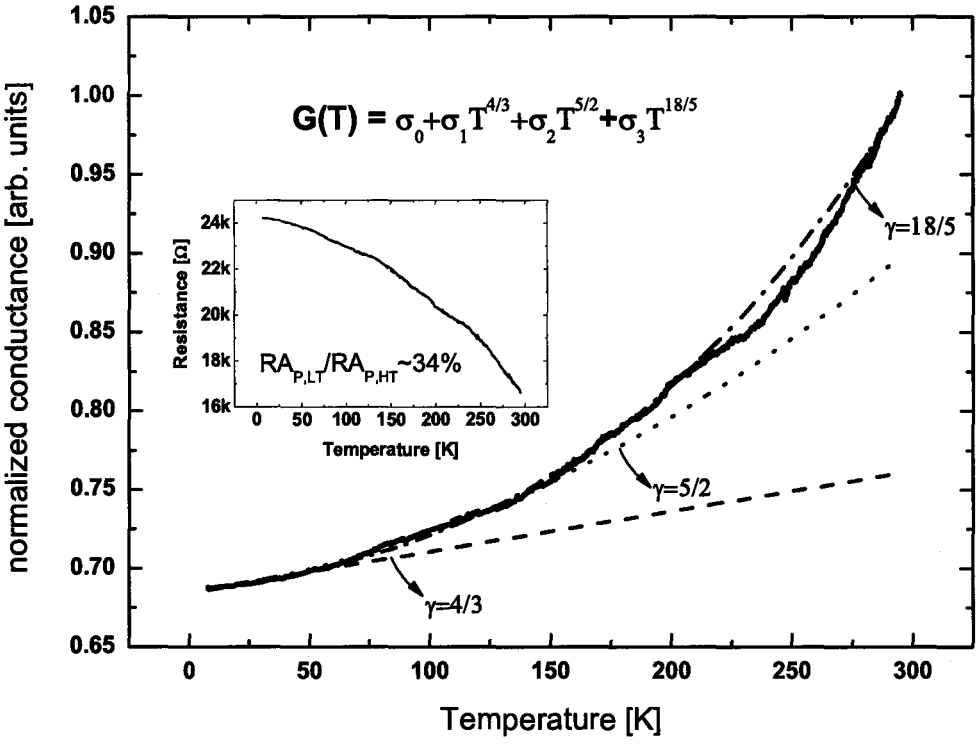

Figure 5.8: Normalized conductance as a function of temperature for a MgO tunnel junction.

conductance curve with increasing hopping contribution (N) as described in section 2.1.2 and shown in the figure 5.8. At low temperature < 70K we find a good fit with only N=2 ($\gamma = N - 2/(N+1) = 4/3$) in equation 2.14. For increasing temperature, we have to add more terms N=4 (γ=N-2/(N+1)=18/5) to obtain a reasonable fit. Including even higher terms does not improve the fit. The fact that we need higher order terms than what is reported in literature for MgO junctions [14], indicates that there might be more hops possible in our junction which is directly related to the amount of impurities in the barrier [17]. This is supported by the discussion in section 4.3.4, where have seen that the partial impurity pressure during the sputtering of the MgO is crucial.

TMR vs Bias voltage

For our best junction, we were able to obtain IV measurements at different temperatures in parallel and anti-parallel alignment before it broke down. This is shown in figure 5.9, where in the upper panels, we see the IV's for parallel and anti-parallel alignment of the electrode magnetization. The missing points are taken out deliberately related to measurement artifacts (occurring at the same current in every measurement due to range switching). In the lower panels we have plotted the TMR. The asymmetry around zero bias might be related to a so-called zero bias anomaly and the error bar in the calculated TMR is highest in this low bias region, therefore we will concentrate on the bias range higher than 0.075V for positive and negative bias of the TMR curve.

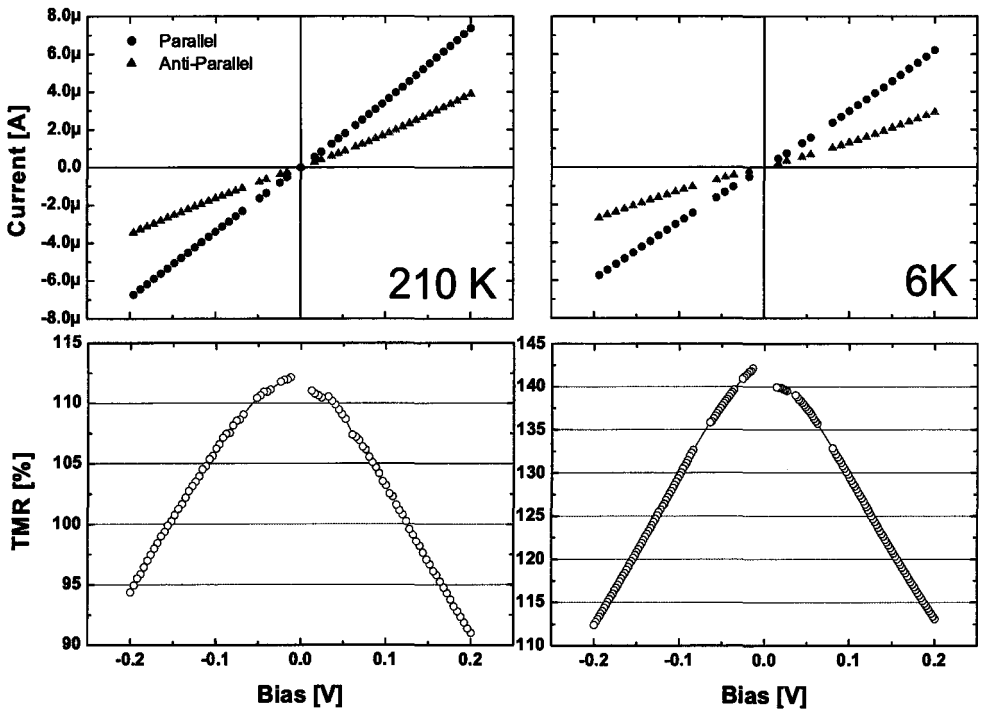

Figure 5.9: IV's in parallel and anti-parallel alignment at 210K and 6K and the calculated TMR as a function of the applied bias voltage.

As already seen before, we have a higher TMR value for low temperature. Another feature that can be seen in the 210K measurement is an asymmetry in the high voltage regime of the TMR value, i.e., we find a TMR value of 95% at -0.2V and 91% at +0.2V. This is not seen in the low temperature measurement. The origin of this effect must be found in the direction of the tunneling current and is also observed with epitaxially grown junctions. For negative bias we are tunneling from the bottom to the top electrode, vice versa for the positive bias.

The interpretation is not clear as yet, and we might speculate that the DOS at the interface with the barrier is different for the top-barrier and bottom-barrier interface. Therefore,

we are working on optimizing the measurement technique to compare our data with literature. This includes the possibility to do measurements with lock-in technique's to directly measure the first (dI/dV) and second derivative (dI^2/d^2V), i.e., performing inelastic tunneling spectroscopy. We will continue with this study when we have reproducible results, in that way we can systematically study the changes. For instance by adding dusting layers at the interface or in the barrier as done by LeClair *et al.* [43]. This will help us with the interpretation of the hopping conductance and interface dependent tunneling.

5.4 Spin Polarized Tunneling measurements

Here, we discuss the results obtained with superconducting tunneling spectroscopy. As explained in the experimental section on the STS technique we replace one of the magnetic electrodes of a MTJ with a superconducting metal. For this we use aluminum with approximately 2 atomic percent of copper; this gives a superconducting gap of typically 0.3mV. From measurements done in the past by Kant *et al.* [25] on Al/MgO/Co, a thickness of 20Å is used for the bottom superconducting Al layer. We decided to grow Al on the bottom to get the superconduction properties without optimizing. The location of the superconducting layer, i.e., on top of the barrier, or below the barrier, is important because the sputtering of MgO might induce oxidation of the Al layer at the interface. This is supported by the results found from the XPS measurements in section 4.3 where we find that our MgO is non-stoichiometric and oxygen rich.

A experimental limitation is that the junctions resistance should be in the order of 1-60 kΩ to be accurately measured. Due to the big variation of the resistance with our MgO junctions the sample preparation is crucial. To overcome the discussed problems we have made the following changes to our junctions: first we have introduced a thin metallic dusting layer of Mg (2 Å) between the MgO and the Al, to prevent the Al from oxidizing at the interface. This might also help a smoother growth of the MgO layer on top of the Al.

In figure 5.10, we show our best SPT measurement up to date on a MgO tunnel junction. The following stack is used: Al(20Å)/Mg(2Å)/MgO(~35Å)/CoFeB(300Å)/Al(20Å) annealed at 390°C in UHV for 30 minutes. The 0T curve shows the superconducting gap of the Al, the 2T curve shows the conductance curve after aligning the junction with the field. The zeeman splitting of the spin-up and spin-down channel is clearly seen.

In figure 5.11(a), we see the same 2T measurement as in figure 5.10 with a Maki fit [28]. We directly see that the fit to the Maki theory is very bad, this is related to the zero bias anomaly commonly observed in tunnel junctions, see [44] for a review. This can be seen in the 5.5T curve where have increased the magnetic field above the critical field of the Al superconductor to force it in its normal state.

In figure 5.11(b) we have subtracted the zero bias anomaly (5.5T) from the 2T data and after normalizing we see that the fit has improved. In the lower left corner we see the fitting parameters where we have fixed the applied field to 2T. A rather low polarization of 19.1% can be seen. This low polarization might be due to many reasons, such as an imperfect

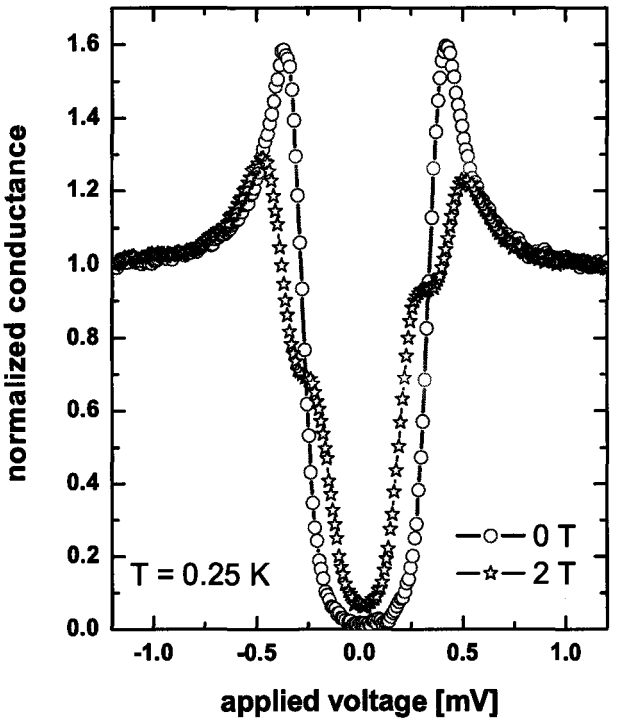

Figure 5.10: Experimental STS conductance curve at 0T and 2T for a MgO tunnel junction.

barrier, oxidation of the barrier-electrode interface, incorrect or low quality texture, and the dusting Mg layer between the superconductor and the barrier.

This measurement was done at the beginning of this thesis work, due to non-optimal results (only one working junction) we decided to focus on fabricating MTJ's. The idea behind this is; when we have optimized the fabrication of MTJ's the step to SPT junctions is small. As mentioned before the TSP of our best MTJ showing 150% TMR at low temperature would result in 65% SPT. However, the average TMR of $\sim$ 50% at low temperature would result in a SPT of $\sim$45%. We will therefore continue with STS measurement on FM/MgO junctions when we have optimal results with MTJ's.

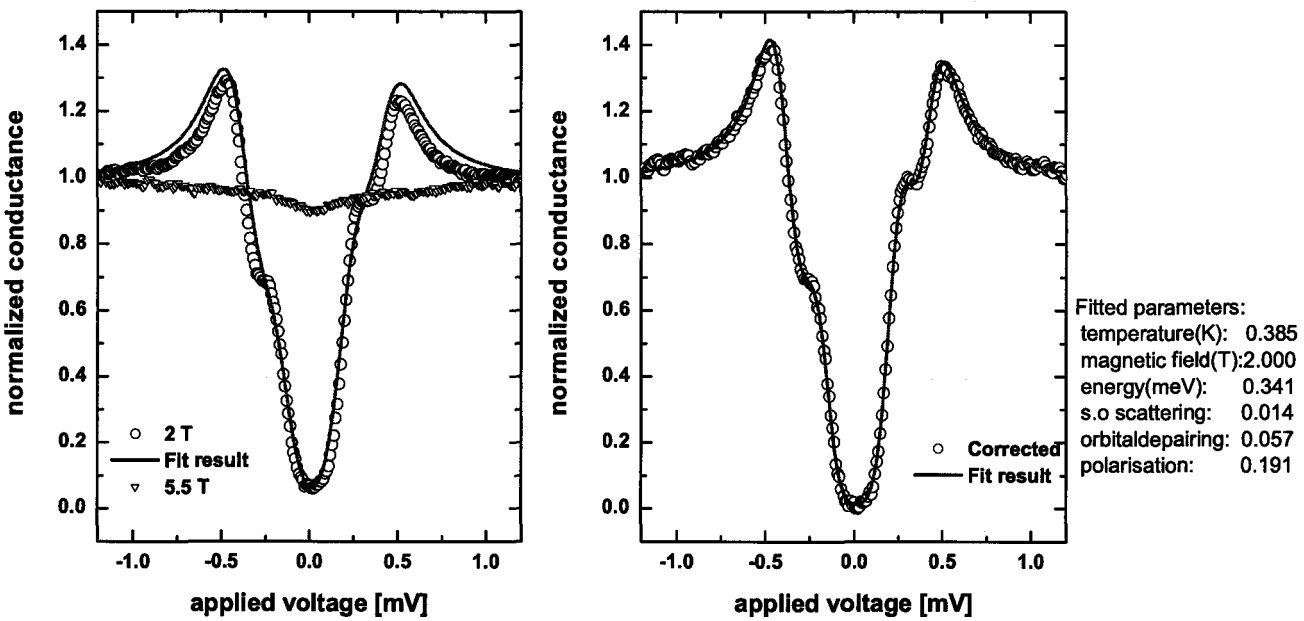

(a) 2T, 5.5 T measurements and fit to the maki theory

(b) Corrected 2T curve and corresponding Maki fit

Figure 5.11: Experimental conductance curves of a MgO tunnel junction showing the effect of the zero bias anomaly on the fitting to the Maki theory.

Chapter 6

Conclusions and Outlook

The goal of this master thesis work as was given in section 1.2 was:

"Fabricate MgO barriers such that the realization of huge TMR effects can be demonstrated in MTJ's. Subsequently measure the TSP using different FM electrodes with MgO barriers."

We started discussing about the theory of tunneling through crystalline barriers in section 2.2. From this discussion, we deduced the most critical points for the fabrication MgO based MTJ's; this was summarized in chapter 3. We also introduced our motivation for our choice for RF sputtering from a MgO target. With these points in mind, we presented a research strategy:

1. Sputter deposition and crystallization of MgO (section 4.1)
2. Sputter optimization of MgO in MTJ's (section 4.2)
3. Chemical analysis of MgO (section 4.3)
4. (a) Magnetic, (b) electrical characterization and (c) SPT measurement of the MgO based MTJ's (chapter 5)

In this chapter we summarize the investigations and conclusions of the individual topics that were presented.

1. Sputter deposition and crystallization of MgO

We started with investigating the structural properties of MgO with X-ray diffraction in section 4.1. This investigation includes (1) the optimization of the growth rate, (2) the effect of the seed layer and (3) the effect of annealing on the crystalline nature of the MgO.

1. The first topic discussed is the target-sample distance during growth of MgO. This investigation was aimed to modify sputter parameters that are known to have a direct

influence on the growth rate, texture and roughness. We found that the optimal target-sample distance is 95mm.

2. Then the growth of MgO on CoFeB is investigated and the impact of annealing. We conclude that in the as-deposited case the MgO grows smoother on CoFeB and the smoothness is increased after the anneal.

3. Finally, we investigated the effect of the anneal temperature on the MgO crystal structure when grown on Al. This is done to facilitate the fabrication of SPT junctions. We show that there is a optimal anneal temperature of 425-475°C for the thick MgO layer under investigation. Which is shown no to be far from what other research groups have found.

2. Sputter optimization of MgO in MTJ's (section 4.2)

To optimize the growth of MgO barriers in MTJ's, we systematically investigated the effect of (1) the sputter power, (2) argon sputter gas pressure and (3) the application of a bias voltage on the substrate holder. As a measure of the optimization we defined two parameters: yield and average TMR.

1. For optimal power, we found 80W; at this power we found the highest average TMR but a slightly lower yield.

2. The optimal gas pressure was found to be the lowest pressure we could sputter at with our system primarily limited by the specification of our magnetron. This was most clearly seen in the yield.

3. By applying a positive bias voltage between the substrate holder and sputter chamber, we showed that we could increase the yield to 100%. We also showed that the average TMR is generally higher for positive bias.

However, we found that the results are scattered. Motivated by these non-optimal performance of our MTJ's we investigated the chemical nature of our MgO barriers.

3. Chemical analysis of MgO (section 4.3)

With XPS we analyzed differently prepared MgO layers, these consist of sputtered MgO, plasma oxidized Mg, single crystal MgO substrate and a metallic Mg layer. By comparing the metallic Mg and the plasma oxidized Mg, we explicitly showed the Mg Auger spectrum to be highly sensitive to the chemical environment of the Mg atoms. The comparison of our sputter deposited MgO with the metallic Mg layer showed that we the Mg in the sputter deposited layer was completely oxidized. Also, we found the first indication of oxygen rich MgO layers. Finally, we attempted to determine the stoichiometry of the sputter deposited MgO by (1) relating the ratio of integrated peak intensities of the Mg and O core level peaks. In this study we find a scattered stoichiometry when we relate the different core

levels of Mg to the 1s peak of O. Therefore, (2) we compared these ratios to those found from the spectrum of a single crystal MgO substrate. This comparison turned out to be inappropriate, due to the large charging effect in the thick MgO substrate. This charging effects the escape depth and the scattering cross section of the photoelectrons, leading to peak broadening. However, we do find an indication of excess oxygen in the sputtered MgO for both methods. Concrete proof was found by examining the shape of the O-1s core spectrum. We find that his core level is split up in two binding energies. The lower binding energy peak is shown to literature to belong to MgO_2. The intensity of this peak increases as we go from the single crystal to sputtered MgO and reaches a maximum for the plasma oxidized case. Therefore, we can conclude that we have an excess of oxygen in our sputter deposited MgO.

4. (a) Magnetic, (b) electrical characterization and (c) SPT measurement of the MgO based MTJ's (chapter 5)

- (a) For controlling the magnetic switching behavior of our electrodes in MTJ's, we used two types of stacks. In the case of hard/soft MTJ's we used ferromagnetic films of different thickness to get a anti-parallel alignment. For exchange biased based MTJ's we used a anti ferromagnetic layer to pin the magnetization of one of the electrodes, thereby obtaining a large region of anti-parallel alignment.

- (b) The electrical characterization of one of our best MTJ's resulted in 90% TMR at room temperature. However, the non-optimal performance of many MTJ's motivated us to look at the electrical properties of our MgO barrier. The behavior of the TMR versus barrier height, indicates that we have a intermixing of the electrode and barrier at the interfaces. Also, a fit using a model which describes hopping conductance applied to R vs T confirms a large amount of impurities in the barrier.

- (c) Finally, a SPT measurement is shown of a CoFeB/MgO tunnel junction. From this measurement we find a SPT of ~19%. From this low value we would find a TMR of 8% at low temperature when we use Julliere's formula equation 2.7. From the average TMR of 20-30% at room temperature found in most of our MTJ's the low temperature TSP would be 35-40%. The highest TMR value found of 150% at low temperature would result in a TSP of 65%.

Origin of excess oxygen and impurities

As we have seen in the chemical analysis we find an excess of oxygen in our MgO layers. The origin of this might be found in an excess of O_2 and H_2O in the sputter chamber during growth of MgO of in the used MgO target.

The sensitivity of MgO to H_2O, i.e. hygroscopic nature as shown by Savio *et al.* [45] makes the partial pressure of H_2O and naturally O_2 during the sputtering of MgO very critical. The source might be the inert argon sputtering gas or the background pressure of

the sputter chamber itself, of in the used MgO target.

From the temperature dependent resistance measurement (see section 5.3) we find an indication for a high amount of impurities in our barrier. This is known to result in a spin-independent conductance channel and might cause spin scattering in the barrier, thereby decreasing the polarization of the tunneling current.

Next we will discuss the solutions that are currently been realized to address the problems we face.

Currently addressed issues

MgO target purity

To decrease the amount of impurities we have procured a new MgO target with 4N purity and a density of 95%. We expect that the amount of impurities reduce the amount of impurities in the MgO barrier.

Sputter magnetron

The problem of the impurities and the non-stoichiometric MgO can be addressed by using a different sputter magnetron. The lowest pressure our current magnetron is able to sputter is $3 \cdot 10^{-3}$ mbar. We have procured a magnetron that is rated to sputter at a pressure one order lower. This directly reduces the amount of impurities in two ways: Firstly, a lower sputter gas pressure results in lower partial impurity pressure thus leading to less impurities in the barrier. Secondly, an enhanced magnetron design will result in a higher growth rate leading to shorter deposition times again leading to less impurities.

Argon supply lines and gas filter

Another cause of the impurities and excess oxygen might be the long Ar distribution line. A minor leak in this line will quickly increase the partial pressure of the impurities and O_2 and H_2O. We are currently planning the leak check of the argon supply gas line. Also, the installation of a gas filter rated to increase the argon gas purity to (9N) will be realized.

Different seed layer for the CoFeB

To improve the correct crystallization of the CoFeB layer, as is shown in literature we intend introducing a Ru layer in direct contact with the bottom CoFeB layer. Thus we can induce a better bcc (001) texture in the CoFeB layer. We are currently experimenting with the Ru layer, up to date this has shown no improvements.

Outlook

The exciting world of research has got a hold on me and therefore I have decided to continue with a PhD that is directly related to the master-thesis work presented here. I will continue where this thesis ends. The first steps that are already taken are discussed in the previous section. If, after optimizing the growth we prove to be successful with producing high quality MgO barriers, we will continue with the understanding of the tunneling process in these barriers. Proposed topics are:

- Expand the resistance-temperature dependent measurements of the MTJ's and try to relate this to the conducting hopping channels by impurities in our junction. This will be conducted with the new target and magnetron. We can then systematically investigate the effect of different levels of impurities in the barrier on the hopping conductance and TMR.
- Investigate the origin of highly textured sputter deposited MgO on amorphous CoFeB layers.
- Investigate the effect of the oxidation of the electrodes at the interface with the barrier with glancing incidence XPS.
- Measure the TSP of FM/MgO with STS technique.
- In collaboration with the PhD work of Paresh Paluskar investigate other barrier materials which have comparable band structures as MgO.
- Investigate the valence band electronic structure with UPS, a first example of our MgO layer is shown below.

Valence band electronic structure with UPS

We have performed a UPS measurement on our sputter deposited MgO layer, again due to the charging effect the interpretation is difficult. We therefore only compare our measurement to a measurement from literature by Schintke *et al.* [46] which shows a comparable valence band structure for a 10 monolayer single crystal MgO film. This is seen in figure 6.1. We see that the global structure of the valence band is the same, and the valence band is approximately at the same energy but shows a more gradual slope.

As can be noted throughout the whole thesis many aspects are not yet fully understood and we hope to get a better understanding when we can reproduce high TMR results. The very broad spectrum of physics involved makes the realization of huge TMR effects with crystalline MgO barriers a very challenging topic.

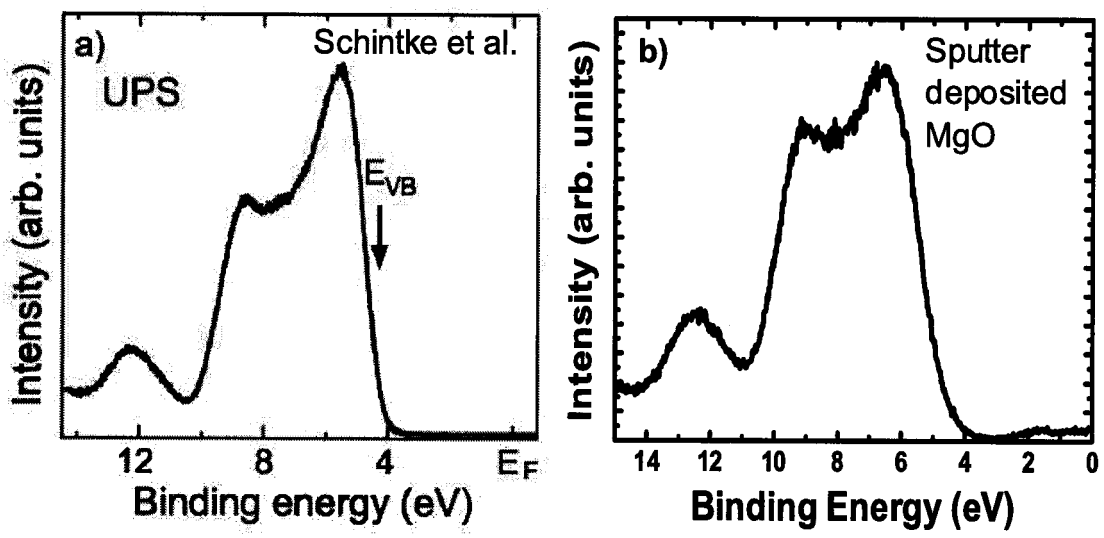

Figure 6.1: (a). UPS spectrum of a 10 monolayer single crystal film as found by Schintke *et al.* (b). UPS spectrum of our sputter deposited layer.

Bibliography

[1] G. A. Prinz. Magnetoelectronics. *Science*, 282:1660, 1998.

[2] M.N. BainBich, J.M. Bronto, A. Fert, F. Nguyen van Dau, F. Petroff, P. Eitenne, G. Creuzet, A. Friederich, and J. Chazelas. Giant magnetoresistance of (001)Fe/(001)Cr magnetic superlattices. *Phys. Rev. Lett.*, 61(21), 1988.

[3] D. Wang, C. Nordman, J.M. Daughton, Z. Qian, and J. Fink. 70with CoFeB as free and reference layers. *IEEE Trans. Mag.*, 40(2269), 2004.

[4] W.H. Butler, X.G. Zhang, and T.C. Schulthess. Spin-dependent tunneling conductance of Fe-MgO-Fe sandwiches. *Phys. Rev. B*, 63(54416), 2001.

[5] J. Mathon and A. Umerski. Theory of tunneling magnetoresistance of an epitaxial Fe-MgO-Fe [001] junction. *Phys. Rev. B*, 63(220403), 2001.

[6] S.S.P. Parkin, C. Kaiser, A. Panchula, P.M. Rice, B. Hugnes, M. Samant, and S.H. Yang. Giant tunnelling magnetoresistance at room temperature with MgO (100) tunnel barriers. *Nat. Mat.*, 3(862), 2004.

[7] S. Yuasa, T. Nagahama, A. Fukushima, Y. Suzuki, and K. Ando. Giant room-temperature magnetoresistance in single-crystal Fe-MgO-Fe magnetic tunnel junctions. *Nat. Mat.*, 3(868), 2004.

[8] H.J.M. Swagten. Spin-dependent tunneling in magnetic junctions. *Elsevier Science*, 2005.

[9] P.M. Tedrow and R. Maservey. Direct observation of spin-state mixing in superconductors. *Phys. Rev. Lett.*, 27(919), 1971.

[10] M. Julliere. Tunneling between ferromagnetic films. *Phys. Lett. A*, 54(225), 1975.

[11] J.G. Simmons. Generalized formula for the electric tunnel effect between similar electrodes separated by a thin insulating film. *J. Appl. Phys.*, 34(1793), 1963.

[12] W.F. Brinkman, R.C. Dynes, and J.M. Rowell. Tunnelling conductance of asymmetrical barriers. *J. Appl. Phys.*, 41(1915), 1970.

[13] C.H. Shang, J. Nowak, R. Jansen, and J.S. Moodera. Temperature dependence of magnetoresistance and surface magnetization in ferromagnetic tunnel junctions. *Phys. Rev. B*, 58(6):R2917, 1998.

[14] X. Kou, J. Schmalhorst, A. Thomas, and G. Reiss. Temperature dependence of the resistance of magnetic tunnel junctions with MgO barrier. *Appl. Phys. Lett*, 88(212115), 2006.

[15] S. Yuasa, A. Fukushima, H. Kubota, Y. Suzuki, and K. Ando. Giant tunneling magnetoresistance up to 410% at room temperature in fully epitaxial Co/MgO/Co magnetic tunnel junctions with bcc co(001) electrodes. *Appl. Phys. Lett.*, 89(042505), 2006.

[16] B. Oliver and J. Nowak. Temperature and bias dependence of dynamic conductance - low resistive magnetic tunnel junctions. *Jour. Appl. Phys.*, 95(546), 2004.

[17] Y. Xu, D. Ephron, and M.R. Beasley. Directed inelastic hopping of electrons through metal-insulator-metal tunnel junctions. *Phys. Rev. B*, 52(2843), 1995.

[18] Ph. Mavropoulos, N. Papanikolaou, and P. H. Dederichs. Complex band structure and tunneling through Ferromagnet-Insulator-Ferromagnet junctions. *Phys. Rev. Lett.*, 85(001088), 2000.

[19] D.A. Papaconstantopoulos. *Handbook of the band structure of elemental solids.* Plenum publishing corporation, 1986.

[20] N. Daude, C. Jouanin, and C. Gout. Electronic band structure of magnesium and calcium oxides. *Phys. Rev. B*, 15(4), 1977.

[21] L.P. Bouckaert, R. Smoluchowski, and E. Wigner. Theory of brillouin zones and symmetry properties of wave functions in crystals. *Phys. Rev.*, 50(58), 1936.

[22] X.-G. Butler, W.H. amd Zhang, S. Vutukuri, M. Chshiev, and T.C. Schulthess. Theory of tunneling magnetoresistance for epitaxial systems. *IEEE Transactions on Magnetics*, 41(10), 2005.

[23] J. Mathon and A. Umerski. Theory of tunneling magnetoresistance in a disordered Fe-MgO-Fe (001) junction. *Phys. Rev. B*, 74(140404(R)), 2006.

[24] R. Meservey and P.M. Tedrow. Spin-Polarised electron tunneling. *Phys. Rep.*, 238(173), 1994.

[25] C.H. Kant. *Probing Spin Polarisation.* PhD thesis, TU/e, 2004.

[26] C. Kaiser. *Novel materials for magnetic tunnel junctions.* PhD thesis, Technischen Hochschule Aachen, 2004.

[27] H.J.M. Swagten. *Magnetism and Magnetic Materials.* Dictaat TU/e, 2005.

[28] K. Maki. Pauli paramagnetism and superconducting state. ii. *Prog. of Theo. Phys.*, 32(1), 1964.

[29] D.C. Worledge and T.H. Geballe. Maki analysis of spin polarized tunneling in an oxide ferromagnet. *Phys. Rev. B*, 62(447), 1999.

[30] M. Tinkham. *Introduction to superconductivity.* McGraw-Hill, New York, 1996.

[31] S.D. Badger. Smoke. *J. Magn. Magn. Mater.*, 100(440), 1991.

[32] Cullity. B.D. *Elements of X-ray diffraction.* Addison-Wesley, London 1978, 2nd edition edition, 1978.

[33] K. Flipse. Spectroscopy of surfaces. TU/e applied physics master course.

[34] D. Briggs and M.P. Seah. *Practical surface analysis*, volume Vol 1: Auger and X-ray photoelectron spectroscopy. Wiley, Chichester, 2nd edition, 1990.

[35] T. Dimopoulos, G. Gieres, and J. Wecker. Large tunnel magnetoresistance with plasma oxidized MgO barrier. *Jour. Appl. Phys.*, 98(073705), 2005.

[36] J. Hayakawa, S. Ikeda, F. Matsukura, H. Takahashi, and H. Ohno. Dependence of giant tunnel magnetoresistance of sputtered CoFeB/MgO/CoFeB magnetic tunnel junctions on MgO barrier thickness and annealing temperature. *Jap. Jour. Appl. Phys.*, 44(L587), 2005.

[37] Y.M. Lee, J. Hayakawa, S. Ikeda, F. Matsukura, and H. Ohno. Giant tunnel magnetoresistance and high annealing stability in CoFeB/MgO/CoFeB magnetic tunnel junctions with synthetic pinnen layer. *Applied Physics Letters*, 89(042506), 2006.

[38] J.C.S. Kools. Exchange-Biased spin valves for magnetic storage. *IEEE Trans. Mag.*, 32(4):3165, 1996.

[39] W. Shen, D. Mazumdar, X. Zou, X. Liu, B.D. Schrag, and G. Xiao. Effect of film roughness in MgO-based magnetic tunnel junctions. *Appl. Phys. Lett.*, 88(182508), 2006.

[40] J. Wollschlager, J. Viernow, C. Tegenkamp, D. Erdos, K.M. Schroder, and H. Pfnur. Stoichiometry and morphology of MgO films grown reactively on Ag (100). *Appl. Surf. Sci*, 142(129), 1999.

[41] J.S. Corneille, J.W. He, and D.W. Goodman. XPS chracterisation of ultra-thin MgO films on a Mo(100) surface. *Surf. Sci.*, 306(269), 1994.

[42] H. Itoh, J. Ozeki, and J. Inoue. Effects of disorder on tunnel magnetoresistance in Fe-MgO-Fe junctions. *Jour. Mag. Magn. Mat.*, 303(e205-e207), 2006.

[43] P. LeClair. *Fundamental aspects of spin polarized tunneling.* PhD thesis, TU/e, 2002.

[44] E.L. Wolf. *Principles of electron tunneling spectroscopy.* Oxford University Press, 1989.

[45] L. Savio, E. Celasco, L. Vattuone, and M. Rocca. Enhanced hydrolysis at monolayer MgO films. *Jour. Chem. Phys*, 119(12053), 2003.

[46] S. Schintke, S. Messerli, M. Pivetta, F. Patthey, L. Libioulle, M. Stengel, A. de Vita, and W. D. Schneider. Insulator at the ultrathin limit: MgO on Ag(001). *Phys. Rev. Lett.*, 87(276801), 2001.